Chapter 9
Laser-Induced Alignment of Molecules in Helium Nanodroplets

Jens H. Nielsen, Dominik Pentlehner, Lars Christiansen, Benjamin Shepperson, Anders A. Søndergaard, Adam S. Chatterley, James D. Pickering, Constant A. Schouder, Alberto Viñas Muñoz, Lorenz Kranabetter, and Henrik Stapelfeldt

Abstract Moderately intense, nonresonant laser pulses can be used to accurately control how gas phase molecules are oriented in space. This topic, driven by intense experimental and theoretical efforts, has been ever growing and developed for more than 20 years, and laser-induced alignment methods are used routinely in a number of applications in physics and chemistry. Starting in 2013, we have demonstrated that laser-induced alignment also applies to molecules dissolved in helium nanodroplets. Here we present an overview of this new work discussing alignment in both the nonadiabatic (short-pulse) and adiabatic (long-pulse) limit. We show how femtosecond or picosecond pulses can set molecules into coherent rotation that lasts for a long time and reflects the rotational structure of the helium-solvated molecules, provided the pulses are weak or, conversely, results in desolvation of the molecules when the pulses are strong. For long pulses we show that the 0.4 K temperature of the droplets, shared

J. H. Nielsen · A. A. Søndergaard
Department of Physics and Astronomy, University of Aarhus,
Ny Munkegade 120, 8000 Aarhus C, Denmark

D. Pentlehner · L. Christiansen · B. Shepperson · A. S. Chatterley · J. D. Pickering · C. A. Schouder · A. V. Muñoz · L. Kranabetter · H. Stapelfeldt (✉)
Department of Chemistry, Aarhus University, Langelandsgade 140, 8000 Aarhus C, Denmark
e-mail: henriks@chem.au.dk

D. Pentlehner
e-mail: Dominik.Pentlehner@th-rosenheim.de

A. S. Chatterley
e-mail: aschatterley@chem.au.dk

J. D. Pickering
e-mail: j.pickering@leicester.ac.uk

C. A. Schouder
e-mail: constantschouder@chem.au.dk

A. V. Muñoz
e-mail: avinas@chem.au.dk

L. Kranabetter
e-mail: kranabetter@chem.au.dk

A. Slenczka and J. P. Toennies (eds.), *Molecules in Superfluid Helium Nanodroplets*,
Topics in Applied Physics 145, https://doi.org/10.1007/978-3-030-94896-2_9

with the molecules or molecular complexes, leads to exceptionally high degrees of alignment. Upon rapid truncation of the laser pulse, the strong alignment can be made effectively field-free, lasting for about 10 ps thanks to slowing of molecular rotation by the helium environment. Finally, we discuss how the combination of strongly aligned molecular dimers and laser-induced Coulomb explosion imaging enables determination of the structure of the dimers. As a background and reference point, the first third of the article introduces some of the central concepts of laser-induced alignment for isolated molecules, illustrated by numerical and experimental examples.

9.1 Introduction

Firstly, it is necessary to define *what* we mean by alignment of molecules, the central topic of this article. Alignment refers to molecular axes being confined with respect to axes fixed in the laboratory system. The simplest case is 1-dimensional (1D) alignment, where a single molecular axis is being confined. This is illustrated on Fig. 9.1 (b) for the linear carbonyl sulfide (OCS) molecules aligned along a space fixed (vertical) axis, in contrast to the case of randomly oriented molecules depicted in Fig. 9.1 (a). The concept of 1D alignment can also apply to asymmetric top molecules, shown in Fig. 9.1 (d). As explained below, when a laser pulse is employed to induce alignment, the aligned axis is the most polarizable axis, which coincides with the C-I axis of the 3,5-difluoro-iodobenzene molecules, chosen as the illustrative example here. The molecules are, however, free to rotate around the aligned axis. A more complete control of the spatial orientation of the molecule requires that this free rotation is arrested. This case, illustrated in Fig. 9.1 (e), is referred to as 3-dimensional (3D) alignment where the three principal polarizability axes are fixed with respect to a space-fixed, Cartesian coordinate system, often denoted as the (X,Y,Z)-coordinate system. Finally, if the molecules are polar, it is often also relevant to control the direction of the permanent dipole moment, a case termed orientation. Figure 9.1 (f) illustrates the situation where the 3,5-difluoro-iodobenzene are both 3D aligned and oriented, which is jointly called 3D orientation. The concept of orientation applies equally to linear (or symmetric top) molecules. In the case of the OCS molecules this would be the situation where the S-end of the molecules all point in the same direction.

Secondly, we must ask *why* it is interesting and relevant to align molecules. One major reason is that samples of aligned and/or oriented molecules make it possible to study or exploit the ubiquitous orientational dependence of molecules' interaction with other molecules, atoms or polarized light. In fact, the orientational dependence of bimolecular reactions was a primary motivating factor for why researchers started to develop techniques to orient and align molecules over 60 years ago [1]. Molecules can also interact with pulses of light and over the past 10–20 years the study and exploitation of how interactions between laser pulses, in particular short and intense laser pulses, and molecules depend on the orientation of the molecule

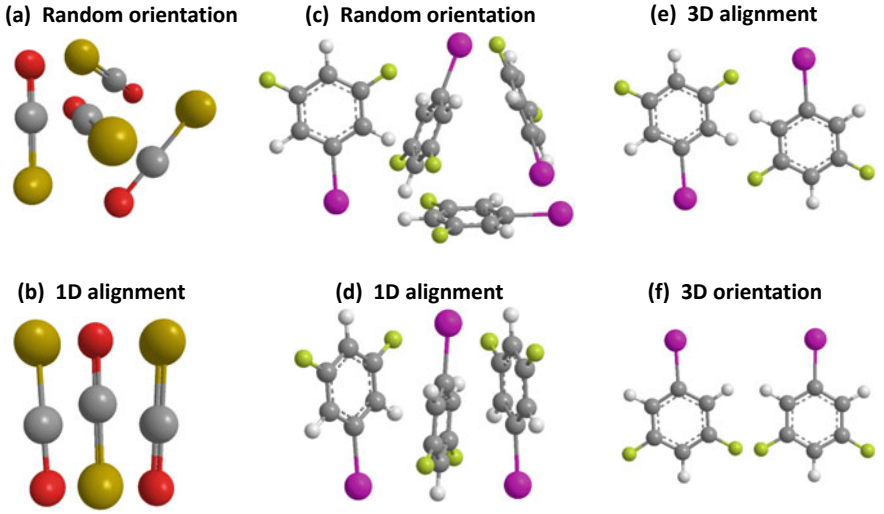

Fig. 9.1 Illustration of 1D alignment, 3D alignment and 3D orientation using the carbonyl sulfide and 3,5-difluoro-iodobenzene molecules as examples

with respect to the polarization state of the laser pulses has been a topic of intense investigation [2]. A second, major advantage of aligned molecules is the fact that they make it possible to perform molecular frame (MF) measurements, which can significantly increase the information content from experimental observables because the blurring they normally suffer from averaging over randomly oriented molecules is strongly reduced. An illustrative example is MF photoelectron angular distributions from aligned molecules where high-information structures appear that are completely absent in experiments on randomly oriented molecules [3, 4].

Finally, the question is *how* to align molecules. The main techniques developed early on were rotational state-selection of molecules by means of hexapolar electric fields [1, 5], 'brute-force' orientation by a strong static electric field [6–9], collisional alignment in a cold molecular beam [10–12], and photoselection whereby polarized light creates alignment in a vibrationally or electronically excited state [13, 14].

The method discussed here employs nonresonant, moderately intense laser pulses to induce alignment. The fundamental interaction responsible for alignment is the polarizability interaction between the molecule and the electric field of the laser pulse. The laser pulse induces an electric dipole moment in the molecule, which in turn interacts with the electric field of the laser pulse. Almost all molecules have an anisotropic polarizability tensor and, consequently, for these molecules the polarizability interaction depends on their spatial orientation with respect to the polarization of the electric field of the laser pulse. The laser pulse forces the molecules to rotate towards an orientation where the polarizability interaction is optimized and this is what leads to alignment of the molecules. In the simplest case of a linearly polarized laser pulse, the potential energy of the polarizability interaction has a minimum when

the most polarizable axis is parallel to the polarization axis. This means that a linearly polarized laser pulse has the potential to induce 1D alignment of molecules. Most of this article concerns 1D alignment of molecules induced by linearly polarized laser pulses. It is, however, also possible to induce 3D alignment using instead an elliptically polarized laser pulse. In this case, the polarizability interaction is optimized when the most polarizable molecular axis is parallel to the major polarization axis and, simultaneously, the second most polarizable molecular axis is parallel to the minor polarization axis. Note that nonresonant means that the laser pulse causes no linear absorption, i.e. the photon energy is not resonant with any transitions in the molecules studied. Moderately intense means that the laser pulse is strong enough that the polarizability interaction induces pronounced alignment, yet weak enough that it does not cause electronic excitation or ionization due to multiphoton absorption.

Laser-induced alignment emerged in the last half of the 1990s [15–21] and beginning of the 2000s [22–30] at the interface between stereochemistry, spectroscopy, strong laser field physics, and wave packet dynamics. Since then the field has undergone a continuous expansion in scope and applications, however with essentially all studies concentrating on gas phase molecules. In 2013 we showed that it is possible to extend laser-induced alignment to molecules embedded inside liquid helium nanodroplets. The purpose of the current article is to provide an overview of laser-induced alignment of molecules embedded in helium nanodroplets, based on work in the period from 2013 to now. The first part of the paper, Sect. 9.2 introduces some of the basic concepts of laser-induced alignment developed for gas phase molecules, exemplified by a few experimental results and calculations. This provides some background and useful reference points for the discussion of molecules in He droplets given in Sect. 9.3. Many more details about laser-induced alignment of gas phase molecules can be found in the existing review articles on the subject [31–35].

9.2 Alignment of Isolated Molecules

9.2.1 Laser-Induced Alignment: Basics

We start by discussing the rotational dynamics of a linear molecule (in a Σ state) induced by a linearly polarized, nonresonant, laser pulse. Theoretically, these dynamics are described by the time-dependent rotational Schrödinger equation with $U(\theta)$ denoting the polarizability interaction:

$$i\hbar\frac{\partial\Psi_{rot}(t)}{\partial t} = \left(B\hat{J}^2 + U(\theta)\right)\Psi_{rot}(t) \tag{9.1}$$

$$= \left(B\hat{J}^2 - \frac{E_0(t)^2}{4}\left(\left(\alpha_\parallel - \alpha_\perp\right)\cos^2(\theta) + \alpha_\perp\right)\right)\Psi_{rot}(t) \tag{9.2}$$

E_0(t): the amplitude (envelope) of the electric field of the laser pulse, $\hat{J}^2$: the squared rotational angular momentum operator, Ψ_{rot}: the rotational wave function, B: the rotational constant, $\alpha_\parallel$ and $\alpha_\perp$: the polarizability parallel and perpendicular to the most polarizable axis, i.e. the molecular axis of a linear molecule, θ: the (polar) angle between the molecular axis and the polarization axis of the laser pulse. We assume that before the laser pulse is turned on, the molecule is populated in a single rotational eigenstate, $|J_k M_k\rangle$, of the field-free Hamiltonian ($B\hat{J}^2$) i.e. $\Psi_{rot}(-\infty) = |J_k M_k\rangle$. Here J_k is the initial quantum number of the rotational angular momentum, M_k its projection on a space-fixed axis parallel to the laser polarization and $|J_k M_k\rangle$ is the rotational eigenfunction given by a spherical harmonic, $Y_{J_k}^{M_k}$. The solution to Eq. 9.2 can be expressed as:

$$\Psi_{rot}^{(k)}(t) = \sum_J d_{JM_k}(t)|JM_k\rangle \tag{9.3}$$

where $d_{JM_k}(t)$ are the expansion coefficients and the index k on $\Psi_{rot}^{(k)}$ indicates the initial state. In other words, the laser pulse creates a superposition of different angular momentum states, $|JM_k\rangle$, but leaves the projection on the laser polarization unchanged. Such a superposition, which is termed a rotational wave packet, can lead to angular confinement, i.e. alignment of the molecule along the polarization axis, provided the phase relationship between the different components $|JM_k\rangle$ in Eq. 9.4 is favorable.

The rotational dynamics depend on the turn-on and turn-off time of the laser pulse. The two most common regimes of alignment are termed adiabatic and nonadiabatic. Here the alignment pulse duration, τ_{align}, and thus both the turn-on and turn-off time, is either much shorter or much longer than the intrinsic rotational period, τ_{rot}, of the molecules, respectively.[1] Here τ_{rot} is defined as $1/2B$ with B given in units of Hz.

In the adiabatic regime, the initial rotational eigenstate $|J_k M_k\rangle$ evolves adiabatically into the corresponding eigenstate of the complete Hamiltonian (given in Eq. 9.2). Such a state, expressed by Eq. 9.3, is called a pendular state [15, 37] and can lead to strong alignment. Upon turn-off, the pendular state evolves back to the initial rotational quantum state. In the adiabatic regime a sample of molecules is, therefore, only aligned during the laser pulse. By contrast, in the nonadiabatic regime, the laser pulse leaves the molecule in a coherent superposition of field-free rotational eigenstates. This superposition can be expressed as:

$$\Psi_{rot}^{(k)}(t) = \sum_J d_{JM_k} \exp\left(\frac{-iBJ(J+1)t}{\hbar}\right)|JM_k\rangle \tag{9.4}$$

where d_{JM_k} in general are complex numbers. An important consequence of Eq. 9.4 is that in the nonadiabatic regime, alignment can occur a long time after the pulse and, in general, the alignment will continue to evolve after the laser pulse is turned off.

[1] Nonadiabatic alignment dynamics can also be induced by turning on the laser pulse slowly and then, typically at the peak, turning it off rapidly [29, 36].

To characterize the degree of alignment, the following measure is normally used:

$$\langle \cos^2\theta \rangle_k = \langle \Psi_{rot}^{(k)} | \cos^2\theta | \Psi_{rot}^{(k)} \rangle \tag{9.5}$$

In practice, measurements involve a sample of molecules initially populated in different rotational states, typically assumed to follow a Boltzmann distribution. To account for this, $\langle \cos^2\theta \rangle_k$ must be averaged over all initial states to give $\langle \cos^2\theta \rangle$:

$$\langle \cos^2\theta \rangle = \sum_k f(k) \langle \cos^2\theta \rangle_k \tag{9.6}$$

where $f(k)$ is the normalized population of state k.

9.2.2 Nonadiabatic and Adiabatic Alignment: OCS Example

In this and the next section, we illustrate numerically the mechanism and alignment dynamics in the adiabatic and nonadiabatic regimes. We use the OCS molecule as an example and solve Eq. 9.2 for a laser pulse with a duration (τ_{align}) that is either much smaller or larger than τ_{rot}. For OCS, $B = 6.0858\,\text{GHz}$, so $\tau_{\text{rot}} = 82.2\,\text{ps}$. For the short-pulse or nonadiabatic regime, we use $\tau_{\text{align}} = 300\,\text{fs}$ and for the long-pulse or adiabatic regime, we use $\tau_{\text{align}} = 600\,\text{ps}$.

Figure 9.2 shows calculated values of $\langle \cos^2\theta \rangle$ for OCS molecules as a function of time, t, after the peak of the linearly polarized, 300 fs laser pulse with a peak intensity of $6.5 \times 10^{12}\,\text{W/cm}^2$. The rotational temperature of the molecules is set to 1 K to match what can be achieved experimentally in cold molecular beams [38]. The calculations take into account that experimentally the molecules are exposed to a distribution of alignment pulse intensities due to the finite beam waist of the probe laser beam used to measure the time dependent degree of alignment.[2] In practice, this is implemented by averaging the calculations over an intensity distribution determined by the actual beam waists of the laser beams. Here we used $\omega_0 = 35$ and 25 μm that are typical values for the alignment and probe beam, respectively.

Before the arrival of the pulse, $\langle \cos^2\theta \rangle = 1/3$, the value for a sample of randomly aligned molecules. During and shortly after the pulse, $\langle \cos^2\theta \rangle$ rises and reaches a first maximum, 0.67, at $t = 0.95$ ps. At this time, some of the angular momentum states in the rotational wave packet (Eq. 9.4) are in phase, which produces alignment. The J-dependence of the complex exponential functions in Eq. 9.4 causes the angular momentum states to fall out of phase at later times, a behavior referred to as wave packet dispersion. On the alignment trace in Fig. 9.2, this manifests as a rapid drop of $\langle \cos^2\theta \rangle$ for $t > 0.95$ ps. Due to the regular rotational energy structure

[2] The probe pulse, sent a time t after the alignment pulse, induces Coulomb explosion of the molecules to probe their spatial orientation. Details are given in Sect. 9.2.3.

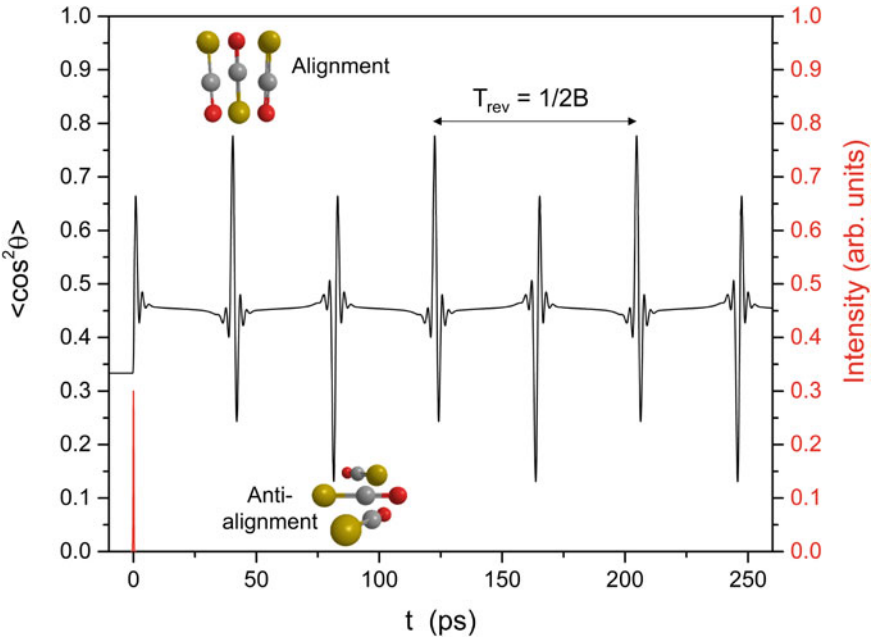

Fig. 9.2 Nonadiabatic alignment dynamics (black curve) calculated for a sample of OCS molecules with a rotational temperature of 1 K. The intensity profile of the alignment pulse is shown by the red curve. $\tau_{\text{align}} = 300$ fs and $I_{\text{align}} = 6.5 \times 10^{12}$ W/cm^2

of linear molecules, modelled as rigid rotors, i.e. $E_{rot}(J) = BJ(J+1)$, the angular momentum states do come back into phase again at longer times.

In particular, at times separated by integer multiples of $1/2B$, each of the complex exponential functions in Eq. 9.4 accumulates a phase of $2\pi N$, where N is an integer. This means that the wave packets given by Eq. 9.4 are periodic with a period of $1/2B$. The same will hold for any expectation value of an operator, like $\langle\cos^2\theta\rangle$, i.e. $\langle\cos^2\theta\rangle$ is also $1/2B$-periodic. Therefore, the initial alignment maximum is repeated every $1/2B$, and this is called the revival period, T_{rev}. The $1/2B$ periodicity, which is 82.2 ps for OCS, manifests itself in the alignment trace in Fig. 9.2, where the transients centered at 82.4 ps, 164.6 ps and 246.7 ps are the 1st, 2nd and 3rd full revivals. Here $\langle\cos^2\theta\rangle$ first dips to a low value corresponding to anti-alignment, where the molecules are confined to the plane perpendicular to the polarization axis, and then rises steeply to a high value where the molecules are aligned along the polarization axis. The prominent transients between the full revivals are termed half revivals. Here, the complex exponential functions are shifted by π compared to their values at the full revivals. This reverses the order of alignment and anti-alignment such that the molecules first align and then anti-align. Note that the peak value of $\langle\cos^2\theta\rangle$ at the half revival, 0.80, exceeds that at the full revivals, 0.67. Higher-order fractional revivals, such as quarter revivals, appear if the OCS molecules are populated initially

in a single rotational state rather than in a Boltzmann distribution of states. They also appear for molecules where the population of odd and even J-states are influenced by nuclear spin statistics, for instance for N_2 [30], CO_2 [39] and I_2 [23]. The appearance of quarter revivals is illustrated by the experimental results on I_2 molecules in Fig. 9.9.

In a classical picture, the alignment pulse exerts a torque on the molecule and thereby sets it into rotation towards the laser polarization. In the limit where the rotation of the molecule during the laser pulse is negligible, the angular velocity, ω, gained by the molecule-laser interaction is given by [40]:

$$\omega = \frac{1}{2}\frac{\Delta\alpha F_{\text{align}} \sin(2\theta_0)}{I\varepsilon_0 c}, \tag{9.7}$$

where $\Delta\alpha = \alpha_{\parallel} - \alpha_{\perp}$ is the polarizability anisotropy, I is the moment of inertia, F_{align} the fluence of the laser pulse, and θ_0 the initial angle between the molecule and the polarization of the laser pulse. Molecules at different initial angles acquire different angular velocities and therefore do not line up with the polarization vector at exactly the same time. In particular molecules with θ_0 close to 90° arrive later than those with θ_0 close to 0°. This explains why the degree of alignment at the prompt maximum is not necessarily particularly high. In this classical model, often termed the delta-kick model, the molecules will continue to rotate, which explains why the degree of alignment decreases after the prompt peak, but they will never reach the same degree of alignment at later times due to the continuum of classically available angular frequencies. Thus, the presence of revivals is a phenomenon that must be described by the quantum model.

The 300 fs alignment pulse converts each molecule from residing in a single rotational eigenstate into a superposition of eigenstates as expressed by Eq. 9.4. The underlying mechanism is multiple Raman-type transitions between rotational states with $\Delta J = 0, \pm 2$ [32, 41], whereas the vibrational and electronic states are unchanged. Information about which rotational states are populated after the alignment pulse is obtained by Fourier transformation of $\langle \cos^2\theta \rangle(t)$. The resulting power spectrum, displayed in Fig. 9.3 (a), shows a series of regularly spaced peaks. The spectral peaks reflect the frequencies of the nonzero matrix elements $\langle JM|\cos^2\theta|J'M\rangle$, i.e. the coherence (coupling) between state $|JM\rangle$ and $|J'M\rangle$. The matrix element is only nonzero if $J - J' = \pm 2, 0$ and thus the frequencies are given by:

$$\nu_{(\text{J–J+2})} = B(4J + 6), \tag{9.8}$$

assuming a rigid rotor model of the molecules.

All the peaks in Fig. 9.3 (a) have been assigned and labelled ($J - J + 2$). It is seen that states up to $J = 20$ are populated. For comparison, the distribution of J-states prior to the pulse, given by a Boltzmann distribution with a temperature of 1 K, is displayed in Fig. 9.3 (b). Here, essentially all molecules reside in states with $J \leq 4$, showing that the polarizability interaction shifts the molecules to much higher-lying rotational states. Figure 9.3 (a) shows that the weight of $\nu_{(\text{J–J+2})}$ is centered around 300 GHz. This defines the oscillation period of $\langle \cos^2\theta \rangle$ during the revivals. In fact, the

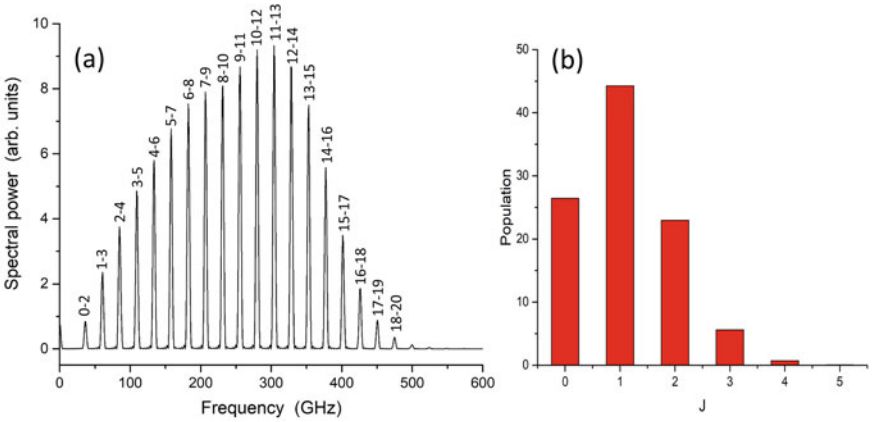

Fig. 9.3 **a** Power spectrum of $\langle \cos^2 \theta \rangle (t)$ shown in Fig. 9.2. **b** Boltzmann distribution of rotational states calculated for OCS molecules at a temperature of 1 K

time difference between the minimum and the maximum of $\langle \cos^2 \theta \rangle$ at both the half and the full revivals is ~1.6 ps—giving an oscillation period of 3.2 ps corresponding to 310 GHz.

Next, we discuss the alignment dynamics in the adiabatic limit. Figure 9.4 (a) shows the time-dependence of $\langle \cos^2 \theta \rangle$ for OCS molecules when a linearly polarized, 600 ps long laser pulse with a peak intensity of 1×10^{12} W/cm^2 is used to induce alignment. The center of the pulse defines $t = 0$. Again, the rotational temperature of the molecules is set to 1 K and the calculations are averaged over the intensities in the probed focal volume of the alignment pulse. The degree of alignment now closely follows the intensity profile of the laser pulse. It is seen that $\langle \cos^2 \theta \rangle$ rises concurrently with the laser pulse, reaches the maximum value of 0.84 at the peak of the pulse, and returns to the isotropic value of 0.33 when the pulse turns off. This is the characteristic adiabatic behavior of laser-induced alignment and it clearly differs from that of nonadiabatic alignment.

The picture of the adiabatic alignment dynamics is that the laser pulse is turned on sufficiently slowly that each rotational eigenstate of the field-free molecule is transferred into the corresponding eigenstate in the presence of the laser field [15, 19]. These states are called pendular states since they correspond to a molecule librating in the angular potential well created by $U(\theta)$, see Eq. 9.4, a motion similar to the oscillation of a pendulum. If the laser pulse is also turned off sufficiently slowly, the pendular states return to the field-free states. In other words, in the true adiabatic limit, the distribution of rotational states after the pulse is the same as before the pulse as if the molecules never knew that they were aligned for a period of time. This situation stands in stark contrast to that of nonadiabatic alignment where the molecules are left in coherent superpositions of field-free eigenstates after the pulse, which leads to a distinct post-pulse time dependence of $\langle \cos^2 \theta \rangle$ as discussed above.

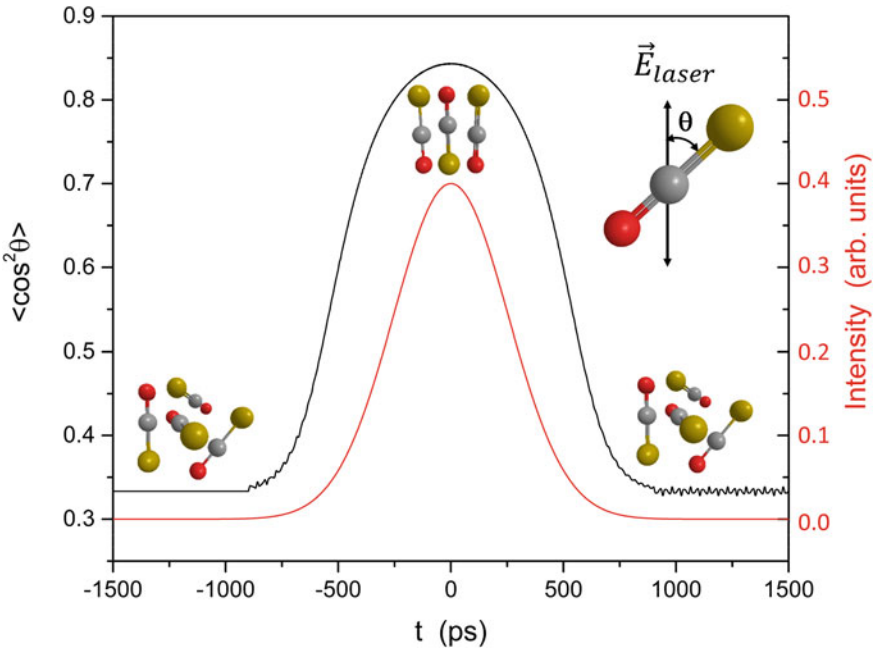

Fig. 9.4 Adiabatic alignment dynamics (black curve) calculated for a sample of OCS molecules with a rotational temperature of 1 K. The intensity profile of the alignment pulse is shown by the red curve. $\tau_{\text{align}} = 600$ ps and $I_{\text{align}} = 1.0 \times 10^{12}$ W/cm^2. The inset illustrates the polar angle θ between the inter-atomic axis of a molecule and the laser polarization, represented by the double-headed arrow

In the adiabatic limit, the degree of alignment for a given molecule is only determined by the intensity of the laser pulse and the rotational temperature [36]. The intensity dependence is illustrated experimentally in Sect. 9.2.4. Here we note that if the intensity of the alignment pulse is increased too much, it will start ionizing and/or dissociating the molecules. Consequently, the intensity must be kept sufficiently low to avoid these unwanted processes. In practice, the limit is in the range $10^{12} - 10^{13}$ W/cm^2 depending on the molecule and the pulse duration.

One significant advantage of adiabatic alignment is that for the many different molecules that can routinely be brought down to rotational temperatures of a few K in cold, supersonic beams, high degrees of alignment can be achieved, lasting for as long as the pulse is turned on. In the present example, $\langle \cos^2 \theta \rangle > 0.8$ for 250 ps. Thus, adiabatic alignment appears useful for applications such as following reaction dynamics in the molecular frame, where observation times of several tens of picoseconds can be required. The advantage of the long-lasting character of adiabatic alignment was demonstrated in real-time measurements of torsional motion of axially chiral molecules [42–44]. The feasibility of this approach requires that the alignment pulse does not perturb the reaction of the molecule or any other process studied. In Sect. 9.3.6 we discuss how rapid truncation of the laser pulse at its peak can convert

the high degree of adiabatic alignment into field-free alignment, lasting tens of ps, for molecules embedded in He nanodroplets. Another advantage of adiabatic alignment is that it is straightforward to extend 1D alignment of an asymmetric top molecule to 3D alignment, see Sect. 9.3.6.

In the nonadiabatic limit, the short duration of the time windows in which strong alignment exists is typically not long enough to enable chemical reaction dynamics to be followed.[3] For instance, in the OCS example with a 300 fs alignment pulse, the strongest alignment, achieved during the half revival, amounts to $\langle \cos^2 \theta \rangle$ staying above 0.8 for only 0.2 ps. The alignment in this time interval occurs, however, long after the alignment pulse is turned off, i.e. under completely field-free conditions. This has proven very useful in many studies of e.g. high-order harmonic generation by intense fs laser pulses [2, 46–50]. For such applications, a high degree of alignment lasting for a few hundred fs is more than enough time to do an experiment.

9.2.3 Experimental Setup

We now turn to discussing the practicalities of actually performing alignment experiments on either isolated molecules or molecules in helium droplets. A schematic diagram of a typical experimental setup, depicting the key components, is shown in Fig. 9.5. There are four main parts. (1) A continuous beam of He droplets doped with molecules, propagating along the Z-axis. (2) A pulsed molecular beam of isolated molecules propagating along the X-axis. (3) Pulsed laser beams propagating along the Y-axis. (4) A velocity map imaging (VMI) spectrometer with a flight-axis parallel to the X-axis.[4]

The helium nanodroplets are produced by continuously expanding high purity (99.9999%) helium gas through a cryogenically cooled 5-μm-diameter aperture into vacuum. The stagnation pressure is typically between 20 and 40 bar while the stagnation temperature is varied between 10 and 18 K. This makes it possible to vary the mean size of the droplets between ∼2000 and 12000 helium atoms [52]. The He droplets pass through a skimmer and enter a pickup cell containing a gas of molecules (or atoms). In most of the experiments described here, the partial pressure of the gas is adjusted to optimize for single molecule doping of each droplet but the partial pressure can also be increased to enable pickup of two molecules by each droplet and subsequent formation of a dimer,[5] see Sects. 9.3.5 and 9.3.7. Hereafter the doped droplets pass through another skimmer (not shown on Fig. 9.5) and enter the 'target chamber' where they interact with the laser pulses. This takes place in the middle

[3] One exception is found here [45].

[4] Note that the (X,Y,Z) coordinate systems used to label the experimental setup is rotated for some of the results in this article.

[5] Although not used in the studies presented here, we note that the He droplet instrument is equipped with two in-line pickup cells. This makes it possible to form e.g. a dimer composed of two molecules or larger heterogeneous complexes [53, 54].

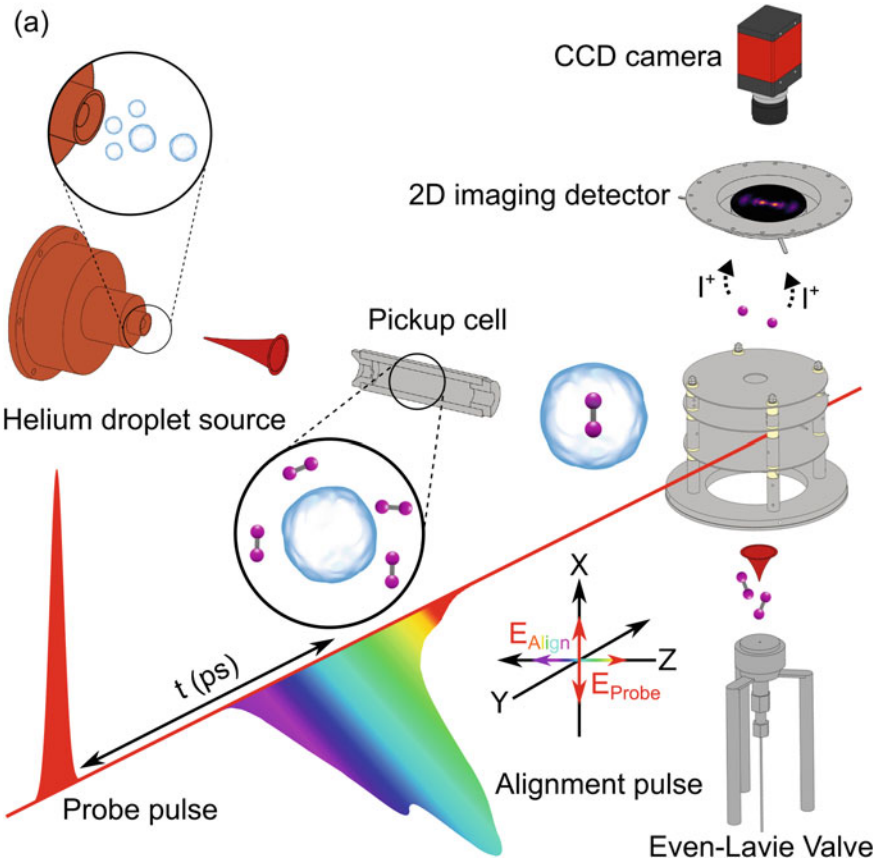

Fig. 9.5 Schematic diagram of the experimental setup. Depicted are the helium droplet source, the pickup cell, the 2D imaging detector, the CCD camera, and the Even-Lavie valve used in the studies on isolated molecules. The direction of the sketched pulse forms indicates the polarisation direction of the laser pulses used to align (along the z-axis) and probe (along the x-axis) the molecules. Adapted from [51] with permission from American Physical Society (APS). Copyright (2018) by APS

of a velocity-map imaging (VMI) spectrometer. For the alignment experiments, two collinear laser beams, crossing the He droplet beam at 90°, are used.

Both laser beams originate from an amplified Ti-Sapphire femtosecond laser system and thus their central wavelength is 800 nm. The pulses in the first laser beam are used to induce alignment of the molecules. Essentially all molecules studied have negligible absorption at 800 nm, which means that the alignment pulses fulfill the requirement of being nonresonant. For the nonadiabatic alignment measurements, the duration of the alignment pulses is in the range from 300 fs to 15 ps. Such durations are obtained by sending a part of the compressed output from the amplified laser system through a pulse stretcher composed of two transmission gratings in a

double-pass geometry [55]. For the adiabatic alignment measurements, a part of the uncompressed output of the laser system is used. The pulses in this beam have a duration of 160 ps.[6]

The pulses in the second laser beam are taken directly from the compressed output of the amplified laser system and their duration is ∼40 fs. These probe pulses are used to measure the spatial orientation of the molecules in the following way. The intensity of these pulses, typically a few times 10^{14} W/cm^2, is high enough to cause rapid multiple ionization of the irradiated molecules. Most of the resulting multiply charged molecular cations break apart into positively charged fragment ions due to internal electrostatic repulsion. This process is termed Coulomb explosion [57]. In many cases, the fragment ions recoil along a molecular axis and thus detection of the emission direction of the fragment ions provides direct information about the spatial orientation of the molecules at the instant that the probe pulse arrives. In the case of 1D alignment, detection of the angular distribution of a single ion species, like I^+ ions from an I_2 molecule, is sufficient to fully characterize the degree of alignment. For the case of 3D alignment, two ion species are typically needed to characterize how the molecules are aligned. We note there are other ways to measure alignment of molecules including the optical Kerr effect [26, 39], photodissociation [19], four-wave mixing [58] and photoionization yields [59].

The ion detection is implemented by a VMI spectrometer [60, 61]. This means that ions created when the probe pulse interacts with the molecules are projected by a weak electrostatic field onto a 2D microchannel plate (MCP) backed by a phosphor screen. The ion images are recorded by a CCD or a CMOS camera that monitors the phosphor screen and captures the fluorescence created by electrons from the MCP impinging on the phosphor screen. On-line software analysis determines and saves the coordinates of each individual particle hit. The MCP is gated in time by a high voltage switch so that only ions with a certain mass-to-charge ratio are detected at one time.

To achieve the intensities of the alignment pulse and the probe pulse needed for the experiments, both laser beams are focused by a lens with a 30 cm focal length. At the crossing point with the beam of He droplets, the Gaussian beam waist, ω_0 of the alignment (probe) beam is typically 35 μm (25 μm). The laser beams are carefully spatially overlapped, so that the smaller beam waist of the probe beam ensures that only molecules that have been exposed to the alignment beam are being ionized and then detected.

The experimental setup is also equipped with a molecular beam of isolated molecules (or dimers). It is formed by expanding a few mbar of a molecular gas in about 60–80 bar of He gas into vacuum through a pulsed Even-Lavie valve [62]. The molecular beam is skimmed and sent to the target chamber where it intersects the focused laser beams at the same spatial position as the droplet beam. The advantage of this setup is that it becomes possible to conduct experiments under the exact same laser conditions for isolated molecules and for molecules embedded in He nanodroplets. More details on the experimental setup can be found in [63].

[6] If needed, an external grating stretcher can increase the duration [56].

9.2.4 *Experimental Observations of Adiabatic Alignment*

In this section, we present experimental results on alignment of gas phase molecules, using I_2 as an example. We start in the (quasi-) long-pulse limit. As mentioned in Sect. 9.2.3, 2D ion images constitute the basic experimental observables. From such images, we can extract information about the spatial orientation of the molecules. For I_2 molecules, I^+ ions are detected. Figure 9.6 (a1) shows an I^+ images recorded with the probe pulse only, polarized perpendicular to the detector plane. These ions are produced when the probe pulse ionizes the I_2 molecules, and the resulting singly or multiply charged molecular ions fragment into an I^+-I, I^+-I^+ or I^+-I^{2+} pair [64]. The key observation for our purpose is that the image is circularly symmetric. This is to be expected since the I^+ angular distribution must be symmetric around the polarization axis because the (multiple) ionization rate of the I_2 molecules, and thus the emission direction of I^+ fragment ions, depends only on the polar angle between the probe pulse polarization and the I_2 internuclear axis. The circularly symmetric

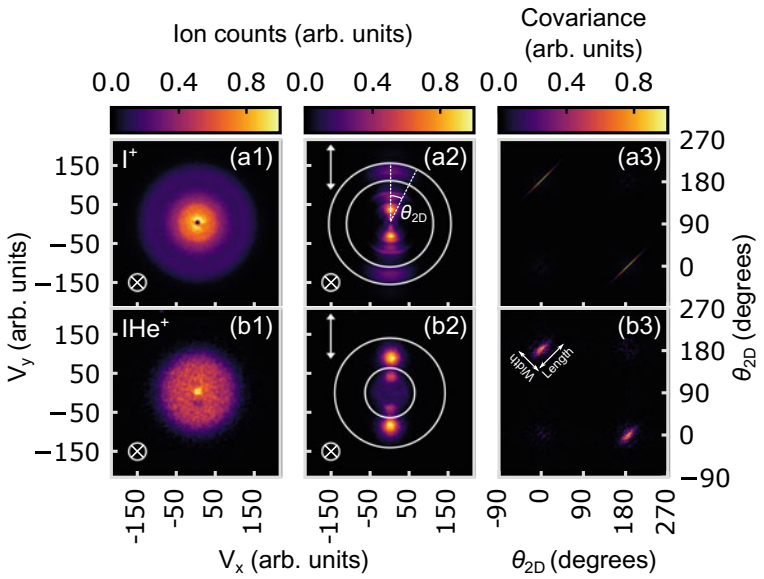

Fig. 9.6 (a1)–(a2) [(b1)–(b2]: I^+ [IHe^+] ion images from Coulomb exploding isolated [He-solvated] I_2 molecules with the probe pulse only (1) and with the alignment pulse included (2). The images represent the detection of the ion velocities, v_x, v_y in the detector plane. (a3) [(b3)]: Angular covariance map of the image in (a2) [(b2)]. The polarization directions of the alignment pulse (vertical: ↕) and probe pulse (perpendicular to the detector plane: ⊗) are shown on the ion images. White circles indicate the radial ranges used for calculating $\langle \cos^2 \theta_{2D} \rangle$ and the angular covariance maps. For the images in the middle column the probe pulse was sent at $t = 0$ and $I_{align} = 0.83$ TW/cm^2. Adapted from [63] with the permission of American Institute of Physics (AIP) Publishing. Copyright 2017 by AIP

image allows us to conclude that the molecules are randomly oriented in the detector plane and thus serves as a reference for the next measurements where alignment in the detector plane is induced.

Figure 9.6 (a2) shows the I^+ images when an alignment pulse is included. The pulse is 160 ps long and is linearly polarized along the Y-axis. The probe pulse is synchronized to the peak of the alignment pulse. Now the I^+ ions are tightly confined along the direction of the alignment pulse polarization. In line with many previous works, we interpret this as evidence of 1D alignment by the alignment pulse. To quantify the degree of alignment, we determine $\langle \cos^2 \theta_{2D} \rangle$ from the average of all I^+ ions detected between the two white circles. Here θ_{2D} is the angle between the polarization axis of the alignment pulse and the projection of the recoil vector of an I^+ ion on the detector plane [see Fig. 9.6 (a2)]. The reason that we determine $\langle \cos^2 \theta_{2D} \rangle$ and not $\langle \cos^2 \theta \rangle$, is that the detector only records the components of the velocity vector in the detector plane. However, it can be shown that $\langle \cos^2 \theta_{2D} \rangle$ contains the same information as $\langle \cos^2 \theta \rangle$ [65].

The ions between the two circles are chosen because they originate from double ionization of the I_2 molecules and subsequent Coulomb explosion into a pair of I^+ ions: $I_2^{2+} \rightarrow I^+ + I^+$. In such a Coulomb fragmentation process, each of the I^+ ions should recoil back-to-back, precisely along the I_2 internuclear axis, meaning that their emission direction is a direct measure of the alignment of the I_2-bond-axis at the instant the probe pulse triggers the Coulomb explosion. This makes these I^+ ions ideal observables for measuring the degree of alignment. To prove that the ions between the white circles are indeed produced by Coulomb explosion, we determined the angular covariance map of the I^+ ions, see Fig. 9.6 (a3). An angular covariance map allows identification of possible correlations in the emission direction of the ions, details are given in Refs. [43, 66–68]. Here two narrow diagonal lines centered at (0°, 180°) and (180°, 0°) stand out and show that the emission direction of anI^+ ion is strongly correlated with another I^+ ion departing in the opposite direction. This identifies the ions as originating from the I^+-I^+ channel. As discussed in Ref. [69] the length of the signal in the covariance map (as defined in panel (b3)) is a measure of the distribution of the molecular axes, i.e. the degree of alignment, whereas the width is a measure of the degree of axial recoil. The observation of a width of $\sim 1°$ shows that the axial recoil approximation is indeed fulfilled, i.e., that the two I^+ ions fly apart back-to-back along the interatomic axis of their parent molecule.

To explore the alignment dynamics, $\langle \cos^2 \theta_{2D} \rangle$ was measured as a function of time, t measured from the peak of the alignment pulse. We remark that before the pulse, $\langle \cos^2 \theta_{2D} \rangle = 0.50$. This is the value of $\langle \cos^2 \theta_{2D} \rangle$ characterizing randomly oriented molecules that corresponds to 1/3 for $\langle \cos^2 \theta \rangle$. The blue curve in Fig. 9.7 shows that $\langle \cos^2 \theta_{2D} \rangle$ follows the intensity profile of the laser pulse during the rising part and reaches the maximum at the peak of the pulse. We note that this adiabatic behavior occurs despite the fact that the rise time, ∼100 ps is significantly shorter than $\tau_{\text{rot}} = 446$ ps[70, 71]. Upon turn-off of the alignment pulse, $\langle \cos^2 \theta_{2D} \rangle$ does not return all the way to 0.50, indicating that the molecules are left in a superposition of eigenstates rather than in single eigenstates. This is corroborated by measurements out to 750 ps, showing characteristic revival structures in $\langle \cos^2 \theta_{2D} \rangle$ although with a

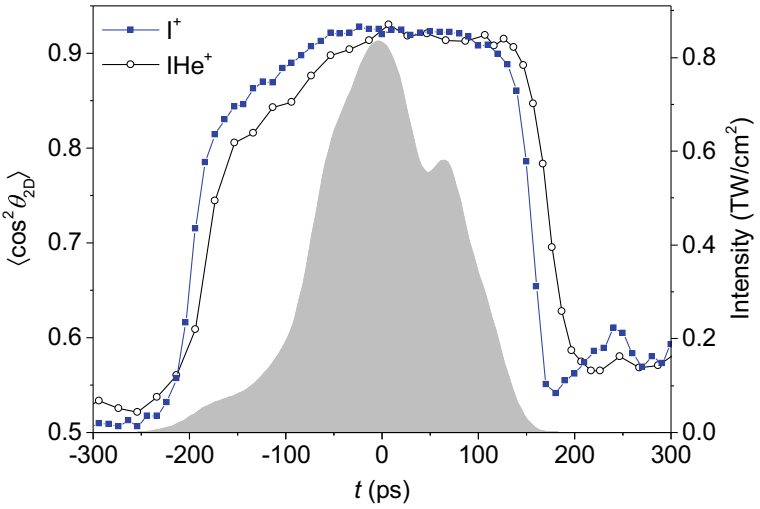

Fig. 9.7 $\langle \cos^2 \theta_{2D} \rangle(t)$ for both isolated I_2 molecules (filled blue squares) and I_2 molecules in He droplets (open black circles). The grey shape shows the intensity profile of the alignment pulse (right vertical axis). Reproduced from [63] with the permission of American Institute of Physics (AIP) Publishing. Copyright 2017 by AIP

smaller amplitude than that at $t = 0$ ps. These nonadiabatic effects are not considered here, but details can be found in Ref. [51]. Here, we focus instead on the maximum degree of alignment obtained at the peak of the alignment pulse.

The blue filled squares in Fig. 9.8 shows $\langle \cos^2 \theta_{2D} \rangle$, obtained at $t = 0$ ps, as a function of the intensity of the alignment pulse, I_{align}. The curve rises gradually from 0.50 at $I_{align} = 0\,W/cm^2$, then levels out and ends at ~ 0.92 for $I_{align} = 8.3 \times 10^{11}\,W/cm^2$. The I_2 molecules should be able to withstand an intensity of several TW/cm^2, so it should be possible to increase the degree of alignment even further by simply increasing I_{align}. In Sect. 9.3.5 we show that an alternative and potentially more useful way to increase $\langle \cos^2 \theta_{2D} \rangle$ is to use I_2 molecules in He droplets (the data represented by the black lines in Fig. 9.8) because their rotational temperature is lower than that of the gas phase molecules.

9.2.5 Experimental Observations of Nonadiabatic Alignment

Next, we turn to alignment in the short-pulse limit induced by 450 fs long, linearly polarized laser pulses. Images of I^+ ion images were recorded for a large number of delays, t, between the centers of the alignment and the probe pulses. For each image, $\langle \cos^2 \theta_{2D} \rangle$, is determined from the ions produced through the I^+-I^+ Coulomb explosion channel, as described above. The black traces in Fig. 9.9 show $\langle \cos^2 \theta_{2D} \rangle$ as a function of t for nine different fluences of the alignment pulse, F_{align}. We note

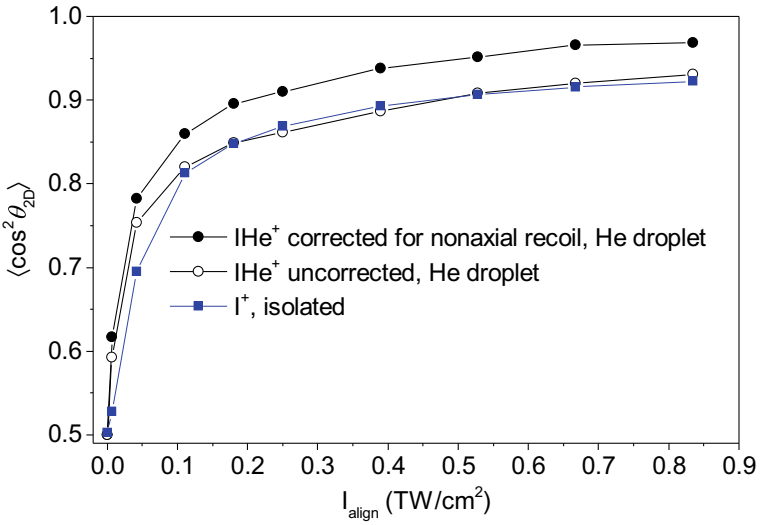

Fig. 9.8 $\langle\cos^2\theta_{2D}\rangle$ at the peak of the alignment pulse as a function of I_{align} for isolated I_2 molecules (filled blue squares) and for I_2 molecules in He droplet without (open black circles) and after (filled black circles) correcting for nonaxial recoil (see text). Reproduced from [63] with the permission of American Institute of Physics (AIP) Publishing. Copyright 2017 by AIP

that the intensity of the alignment pulse, I_{align}, is given by $F_{\text{align}}/\tau_{\text{align}}$, so for e.g. $F_{\text{align}} = 0.25\,J/cm^2$, $I_{\text{align}} = 5.5 \times 10^{11}$ W/cm^2.[7]

The overall structure of the nine alignment traces is similar to that calculated for OCS and shown in Fig. 9.2: a prompt peak shortly after the pulse, a half revival, centered at ∼225 ps, and a full revival centered at ∼448 ps. In addition, there are transients at ∼109 ps and ∼333 ps, which are assigned as the quarter and three-quarter revival, respectively. These quarter revivals appear because of the unequal population of rotational states with odd and even J, caused by the nuclear spin statistical weight of the odd/even J states = 21/15.

The effect of increasing F_{align} is twofold. First, the prompt peak and the revivals narrow, and their oscillatory structure becomes faster. The zoomed-in region, displayed in the right column of Fig. 9.9 illustrates this effect for the prompt peak. Second, the amplitude of the prompt peak and of the revivals increase as F_{align} is increased up to 3.7 J/cm^2. Notably, the global maximum (minimum) of $\langle\cos^2\theta_{2D}\rangle$, attained at the half (full) revival increases (decreases) from 0.61 (0.42) at $F_{\text{align}} = 0.25$ J/cm^2 to 0.88 (0.28) at $F_{\text{align}} = 3.7$ J/cm^2. In other words, both the peak alignment and peak anti-alignment sharpen when F_{align} is increased. Increasing F_{align} beyond 3.7 J/cm^2, leads to a gradual weakening of both the global alignment and anti-alignment maxima in the alignment traces.

[7] The measurements with F_{align} = 6.4, 7.4 and 8.7 J/cm^2 were recorded with an alignment pulse duration of 1300fs to avoid ionization.

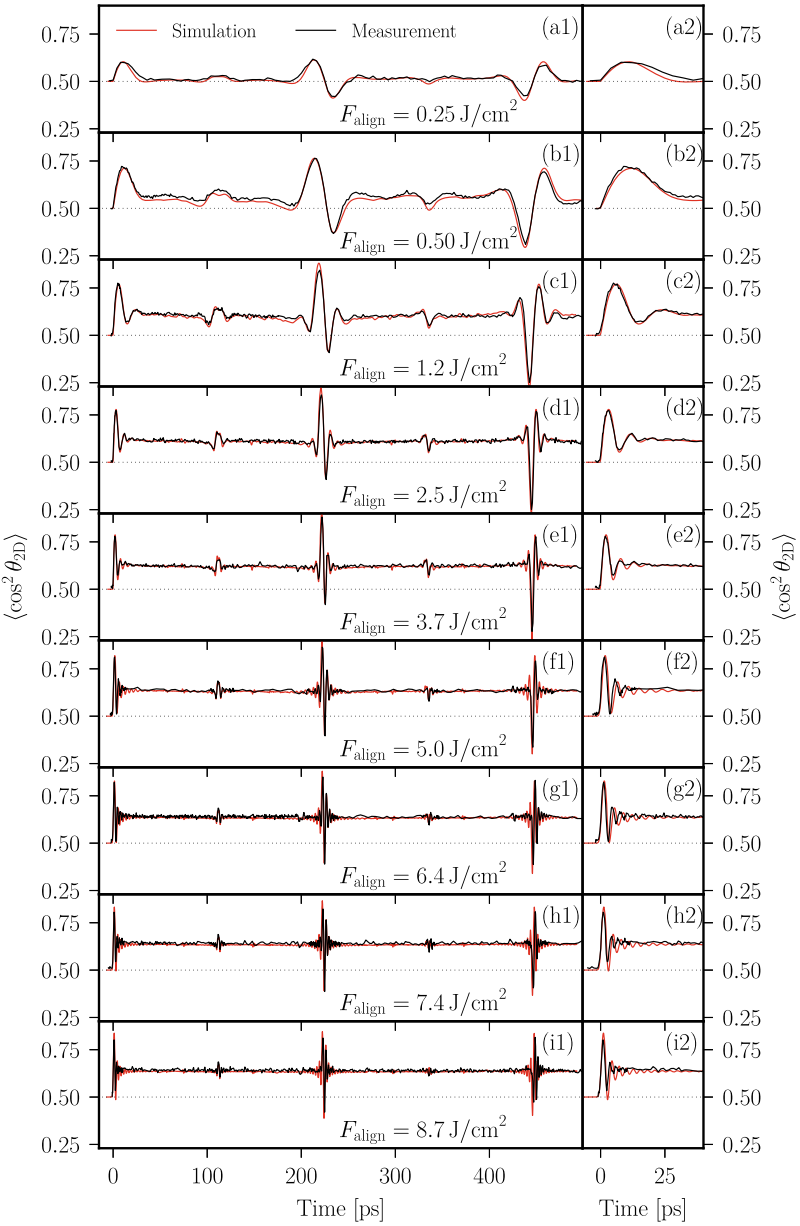

Fig. 9.9 Time-dependence of $\langle\cos^2\theta_{2D}\rangle$ for isolated I_2 molecules at 9 different fluences of a 450 fs alignment laser pulse. The rightmost panels show a zoom of the first 30 ps

Both effects are caused by the fact that as the intensity of the alignment pulse increases, the I_2 molecules are excited to increasingly higher rotational states, which can be seen directly in the spectra of $\langle \cos^2 \theta_{2D} \rangle$, discussed below. This increased width of the wave packet in angular momentum space, enables a tighter angular confinement of the molecular axes but only if the different angular momentum states in the rotational wave packets have a well-defined phase relationship [72]. This is analogous to how broadening a laser pulse in frequency space allows it to become narrower in the time-domain, provided that the frequency components in the pulse are phase-locked. We interpret the weakening of the alignment and the anti-alignment at $F_{\text{align}} > 3.7\,\text{J/cm}^2$ as due to a non-optimal phasing of the angular momentum states in the wave packet. The reason is that the frequencies of the highest angular momentum components in the wave packet are so high that they start evolving during the pulse leading to a phase shift compared to the lower angular momentum components. Expressed classically, the delta-kick model is no longer valid at the highest fluences. Using two alignment pulses, or more generally a shaped alignment pulse, the phase relationship of the components in broad rotational wave packets can be optimized, to increase the degree of alignment further [73, 74]. We note that at the highest fluences the rapid oscillatory structure of the half and full revivals is also influenced by the centrifugal distortion, i.e. deviation from the rigid rotor structure [75]. This dispersive effect is much more pronounced for molecules in He droplets and will be discussed in Sect. 9.3.3.

As mentioned in the discussion of the simulated OCS nonadiabatic alignment dynamics, the spectral content of the wave packets is revealed by Fourier transformation of $\langle \cos^2 \theta_{2D} \rangle(t)$. Figure 9.10 shows the spectrum for each alignment trace. At the lowest fluences, $F_{\text{align}} = 0.25\,\text{J/cm}^2$ and $F_{\text{align}} = 0.50\,\text{J/cm}^2$, only about 8 peaks are observed, see inset on Fig. 9.10 (b). The assignment of the spectral peaks shows that no rotational states higher than $J = 9$ are significantly populated. For comparison, we have plotted the Boltzmann distribution of rotational states for I_2 at a temperature of 1 K, the estimated rotational temperature of the molecular beam (see also Sect. 9.3.5). As shown by the inset in Fig. 9.10 (a), the states populated are in the range $J = 0$–10, i.e. almost the same as those derived from the spectrum in Fig. 9.10 (b). We conclude that at $F_{\text{align}} = 0.25\,\text{J/cm}^2$ and $F_{\text{align}} = 0.50\,\text{J/cm}^2$, the probability of a Raman transition between J states is so low that the redistribution of rotational states is very modest.

This is no longer the case when F_{align} is increased. Figure 9.10 shows how the spectrum broadens and shifts to higher frequencies as F_{align} increases. At the highest fluence, $F_{\text{align}} = 8.7\,\text{J/cm}^2$, the spectral width is greater than 200 GHz and there are spectral components beyond 450 GHz. One of the highest-frequency peaks that can be identified is centered at ~454 GHz, which corresponds to the frequency beat between $J = 100$ and $J = 102$. These high-lying J states have been populated by a sequence of $\Delta J = \pm 2$ Raman transitions starting from the initially populated low-lying rotational states. We note that in many of the spectra from $F_{\text{align}} = 1.2\,\text{J/cm}^2$ to $8.7\,\text{J/cm}^2$ there is an alternation in the amplitude of the peaks, with those corresponding to odd J states being stronger than those corresponding to even J states.

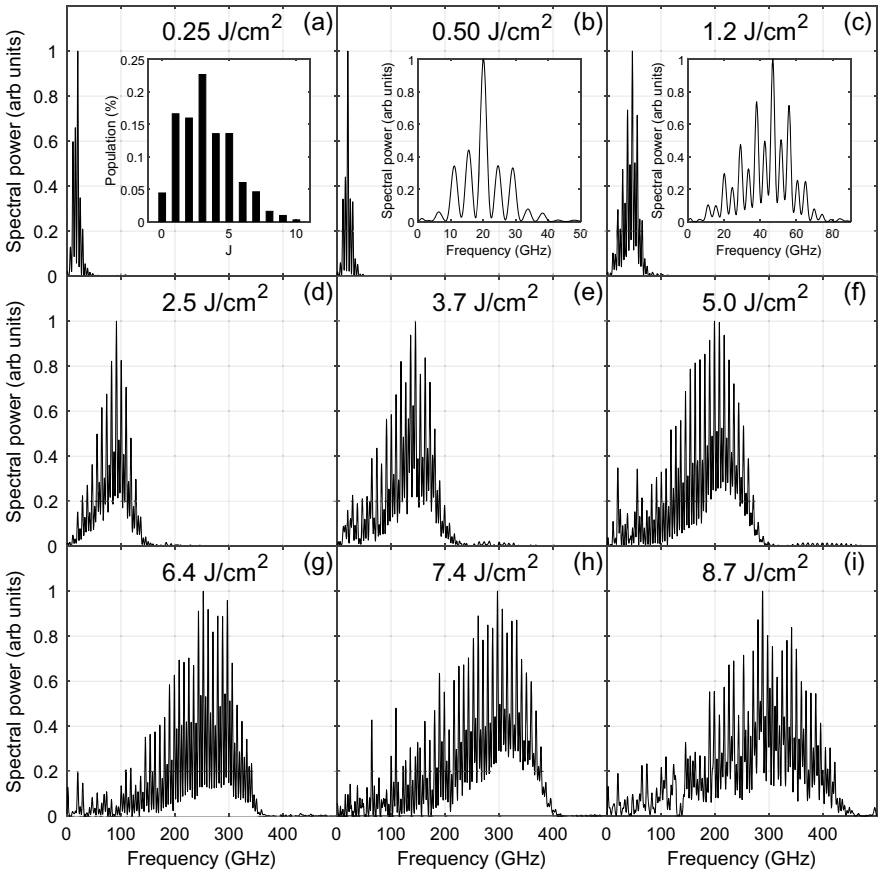

Fig. 9.10 Power spectra of each of the $\langle \cos^2 \theta \rangle(t)$ traces shown in Fig. 9.9. In (**b**) and (**c**), the inset shows a zoom on the spectral peaks. The inset in (**a**) is a Boltzmann distribution of rotational states calculated for I_2 molecules at a temperature of 1 K

This is a consequence of the nuclear spin statistics. The nuclear spin of ^{127}I is 5/2, which gives a statistical weight of 21 to odd and 15 to even J states.

To analyze the experimental data we make comparisons to the predictions of both the quantum model and the classical delta-kick model. In the quantum model, the time-dependent Schrödinger equation, Eq. 9.2 is solved numerically for the I_2 molecules to give the experimental observable, $\langle \cos^2 \theta_{2D} \rangle$. The calculations were averaged over the focal volume determined by the measured beam waists of the alignment (ω_0 = 30 μm) and probe beams (ω_0 = 25 μm) and with the rotational temperature as a free parameter. As seen in Fig. 9.9 the agreement between the experimental (black curves) and simulated results (red curves), is very good. The minor discrepancies observed may be due to neglect of centrifugal distortion effects (at the highest fluences) in the simulation and the fact that the ionization efficiency

Table 9.1 Comparison of the maximal J quantum number calculated classically, J_{max}^{clas}, (see text) and observed in the experimental spectra, J_{max}^{obs}—for four different fluences of the alignment pulse

F_{align}, J/cm ^{2}	ω, 10^{12} Hz	E_{rot}^{clas}, cm^{-1}	J_{max}^{clas}	J_{max}^{obs}
1.2	0.23	10	16	16
2.5	0.49	45	34	34
5.0	0.98	179	69	65
8.7	1.7	541	120	102

of the probe pulse depends on the molecular alignment. Overall, the good agreement demonstrates that time-dependent rotational dynamics of gas phase linear molecules, induced by fs or ps laser pulses, is well-understood (Table 9.1).

We also applied the delta-kick model to produce a classical prediction of how much rotational excitation the alignment pulse induces. For this, we used Eq. 9.7 with $\theta_0 = 45°$, to calculate the maximal angular velocity, ω, of a molecule after the interaction with the laser pulse, assuming that the molecule did not rotate before the laser pulse (which is reasonable for a rotational temperature of 1 K). Classically, the rotational energy, E_{rot}^{clas}, is given by $E_{rot}^{clas} = \frac{I}{2}\omega^2$, where I is the moment of inertia of an I_2 molecule. If we then equate E_{rot}^{clas}, in units of cm^{-1}, with the quantum expression for the rotational energy, $BJ(J+1)$, (B in units of cm^{-1}) we can determine the maximal J quantum number, J_{max}^{clas}. This can be compared to the observed maximal quantum number, J_{max}^{obs} read off from the spectra in Fig. 9.10. Table 9.1 list the values of ω, E_{rot}^{clas}, J_{max}^{clas} and J_{max}^{obs} for four different fluences of the experiment. At F_{align} =1.2 J/cm^2 and 2.5 J/cm^2 the classical model captures the observations essentially spot-on. At the two higher fluences, the classical calculation slightly overestimates the observed maximal rotational quantum state in the wave packets. This corroborate that the rotational dynamics of the highest-lying angular momentum states excited by the alignment pulse are so fast that the delta-kick model is not perfectly valid, i.e. the molecules rotate slightly during the pulse.

Finally, we illustrate the spectroscopic aspect of nonadiabatic alignment, i.e., how it is possible to determine accurate rotational constants from the time-dependent $\langle\cos^2\theta_{2D}\rangle$ measurements. We do so to introduce a technique applied to molecules in He droplets as discussed in Sect. 9.3.3. We use data for $F_{\text{align}} = 0.5$ J/cm^2 now recorded in the interval -10 ps to 3230 ps. Figure 9.11(a) shows $\langle\cos^2\theta_{2D}\rangle(t)$ and Fig. 9.11 (b) the corresponding spectrum obtained by Fourier transformation. The alignment trace exhibits a sequence of full and fractional revivals. Their decaying amplitude as a function of time is due to coupling between the rotational angular momenta and the nuclear spins through the electric quadrupole interaction, see Ref. [76] for details. Here we focus on the position of the peaks in the spectrum. Note that these peaks are much narrower than those in Fig. 9.10 (b), due to the >5 times higher spectral resolution resulting from the > 5 times longer time measurement. The black squares in Fig. 9.12 show the central frequencies of the peaks in the spectrum and the red line the fit to B(4J+6), see Eq. 9.8. The best fit is obtained

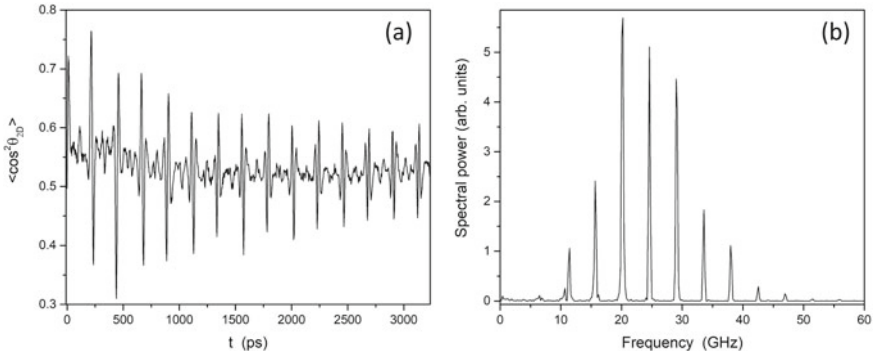

Fig. 9.11 **a** $\langle \cos^2 \theta_{2D} \rangle$ for isolated I_2 molecules with $F_{\text{align}} = 0.50\,\text{J/cm}^2$. **b** Power spectrum of $\langle \cos^2 \theta_{2D} \rangle(t)$ shown in (**a**)

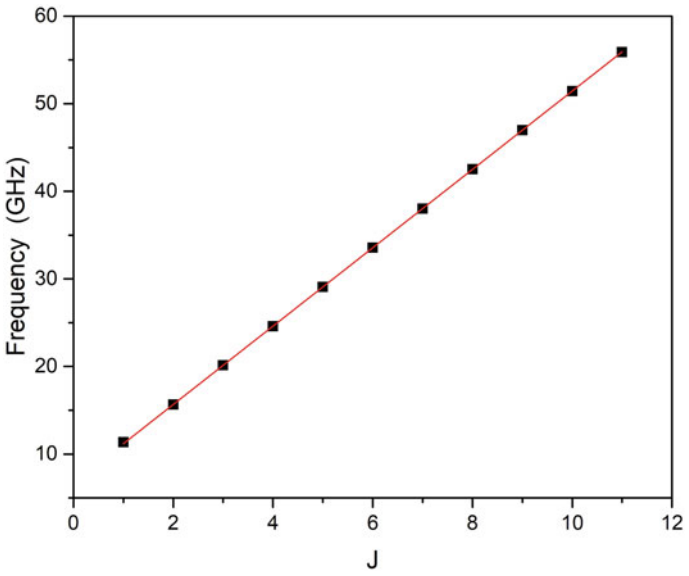

Fig. 9.12 Central frequencies of the $(J–J+2)$ peaks in the power spectra versus J. The red line represent the best fit using Eq. 9.8

for B = 0.03731±0.00002 cm^{-1} = 1.119±0.0001 GHz , which agrees exactly with the value given on https://webbook.nist.gov/chemistry/. Our results demonstrate the possibility for accurate determination of rotational constants, and thus information on molecular structure, from time-resolved rotational dynamics measurements, a discipline broadly termed rotational coherence spectroscopy [77, 78].

9.2.6 *Laser-Induced Alignment: A Versatile and Useful Technique*

The sections above have demonstrated the ability of moderately intense laser pulses to induce high degrees of alignment in both the nonadiabatic and the adiabatic regime. Space limitation of this article prevents us from providing a full account of laser-induced alignment, so again we refer readers to the aforementioned reviews. We do, however, want to mention a few central points here. First of all, laser-induced alignment applies to all molecules that have an anisotropic polarizability tensor, which includes all molecules expect for spherical tops like methane and sulphur-hexafluoride. In practise, laser-induced alignment has been applied to a variety of molecules ranging from the simplest diatomics like N_2 [30] to substituted biphenyls [79]. As shown in the coming sections, using He droplets extends the scope of laser-induced alignment to even larger and more complex systems. In the previous sections, 1D alignment was discussed but we stress that it is also possible to create 3D aligned molecules, in particular by using elliptically polarized pulses in the adiabatic regime [22, 80], but also by using fs/ps pulses [81–83] or combinations of long and short pulses [84, 85]. In Sect. 9.3.6, we discuss 3D alignment of molecules in He droplets. Finally, we would like to point out that in the case of polar molecules, laser pulses in combination with a weak static electric field makes it possible to both create strong alignment and a very high degree of orientation [86–91]. This technique, now referred to as mixed-field orientation, is particularly efficient when the polar molecules are quantum-state selected by an inhomogeneous static electric field prior to the laser-interaction [88, 89, 92]. Mixed-field orientation has been applied to both 1D and 3D orientation [80, 93].

The ability to exert rigorous control over the rotation, alignment and orientation of molecules has proven useful in a number of applications in molecular science and opened new opportunities. Examples include imaging of molecular orbitals by high harmonic generation [46, 94, 95] or by photoelectron angular distributions [3, 96, 97]; alignment-dependent yields of and molecular frame photoelectron distributions from strong-field ionization by intense, polarized fs pulses [98–104]; imaging of static molecular structures by Coulomb explosion, by electron diffraction [105–109] or by x-ray diffraction[110, 111]; time-resolved imaging of molecular structure during intramolecular processes such as torsion [42, 44] and dissociation [45, 112]; high-resolution rotational coherence spectroscopy [113–115]; development of the optical centrifuge and the application of molecular superrotors [116–120]; intramolecular charge migration with sub-fs time resolution using high harmonic generation [50]; and determination of the absolute configuration of chiral molecules [121].

9.3 Alignment of Molecules in Helium Nanodroplets

9.3.1 Alignment of Molecules in a Dissipative Environment?

An interesting and perhaps obvious question to ask is whether laser-induced alignment techniques can be extended to molecules that are no longer isolated. This question was addressed theoretically around 2005 focusing on nonadiabatic alignment of linear molecules subject to binary collisions in a dense gas of atoms or molecules [122, 123]. It was shown that the collisions caused both dephasing and population relaxation of the energy levels in the rotational wave packets. As a consequence, the amplitudes of the revivals in the $\langle \cos^2 \theta \rangle$ traces were reduced when the revival order increased, and the permanent alignment level decayed gradually. The revival period remained, however, identical to that of the isolated molecules since the collisions did not change the energy of the available rotational states. A few years later, the first experiments, exploring systems such as CO_2 molecules in a gas of Ar atoms [124] or a pure gas of N_2 molecules [125], were reported. Subsequently, a number of related studies have been published extending measurements and detailed theoretical analysis to other molecular species and mixtures [126–129].

For molecules in classical solvents, like water or ethanol, the situation is qualitatively different. Firstly, a solute molecule is no longer rotating freely due to the high collision rate with the solvent molecules (or atoms) [130]. When the molecules are immersed in a liquid they typically lose the discrete rotational energy level structure characteristic of the gas phase. Secondly, even if a laser pulse could initiate coherent rotation of a molecule, the high collision rate would rapidly perturb the rotation. Thirdly, an alignment pulse would interact not just with the solute molecule but also with the many solvent molecules (or atoms) surrounding it. It seems likely that these three circumstances obstruct the transfer of molecular alignment, based on laser-induced formation of coherent superposition of rotational states, from gas phase molecules to molecules in a solvent.

9.3.2 Alignment of Molecules in He Droplets: First Experiments

In 2007 we started to think about using molecules embedded in helium nanodroplets as an alternative system for studying laser-induced alignment of molecules in a dissipative environment. At that time, our motivations were manifold. Firstly, infrared spectra of molecules, such as OCS, SF_6, and N_2O, in He droplets exhibit a discrete spectral line structure quite similar to that observed for gas phase molecules. This structure had been interpreted as free rotation of the molecules along with a local solvation shell of He atoms, leading to effective rotational constants smaller than those of the corresponding isolated molecules [52, 53, 131]. The rotational coherence lifetimes, estimated from the linewidths of IR and microwave spectra, were on

the order of nanoseconds, corresponding to multiple rotational periods. Secondly, IR spectra had shown that the rotational temperature of molecules in He droplets was around 0.4−0.5 K [132–134]. Such low temperatures would be advantageous for creating a high degree of alignment [135]. Thirdly, the interaction between an alignment pulse and the solvent (the He atoms) should be negligible due to the low, isotropic polarizability and high ionization potential of He atoms. Fourthly, recent laser-based photodissociation experiments [136, 137] had shown that ion detection by velocity map imaging was possible for molecules in He droplets [138]. This strongly indicated that the detection methods, notably femtosecond laser-induced photodissociation and Coulomb explosion, employed to characterize the degree of alignment for gas phase molecules, could also be applied to molecules in He droplets. Finally, helium droplets had been shown to be able to pick up and solvate essentially any molecular species that could be brought into gas phase [52–54, 139–142]. Therefore it should become possible to study alignment for a variety of molecular systems, including some that would otherwise be difficult to explore in cold molecular beams.

The aforementioned considerations built the expectation that both adiabatic and nonadiabatic alignment of molecules in He droplets would be possible. Regarding nonadiabatic alignment, we expected that the alignment dynamics for a given molecule slower be slower than that observed in the gas phase due to the increase of the moment of inertia from the solvation shell [134, 143]. Thus, it seemed likely that the revival periods would be larger compared to that of isolated molecules, and also that the number of revivals might be limited due to a finite rotational coherence lifetime resulting from coupling between the molecule and the surrounding He solvent. We also expected adiabatic alignment to be feasible, and furthermore, that the degree of alignment would benefit from the low rotational temperature [135].

The construction of an experimental setup in our laboratory for exploring laser-induced alignment of molecules was completed in 2010. The plan was to explore alignment in the nonadiabatic limit using a 450 fs kick pulse to initiate alignment and a delayed, intense 30 fs probe pulse to determine the time-dependent degree of alignment via Coulomb explosion. Initially, a pulsed cryogenic valve was employed to produce He droplets [144], to match the pulsed nature of the laser beams. The droplets were doped with either iodobenzene (IB) or methyliodide (MeI) molecules. As a first test, we used only the probe pulse, linearly polarized in the detector plane. The intensity of the probe pulse was $I_{\text{align}} = 1.8 \times 10^{14}\,\text{W/cm}^2$, which is strong enough to multiply ionize IB or MeI molecules and create I^+ fragments from Coulomb explosion [145, 146]. For isolated molecules the I^+ images are angularly anisotropic with most ions detected along the polarization direction. The reason is that the probability for multiple ionization is highest (lowest) for those molecules that happen to have their most polarizable axis (the C-I axis for both species) parallel (perpendicular) to the polarization vector of the probe pulse at the instant that it arrives. Details on this 'geometrical' alignment or enhanced ionization are given in [147]. Our first objective was to detect such angular confinement for the I^+ ions created by Coulomb exploding either the IB or MeI molecules in the droplets, as this would prove our ability to detect an anisotropic angular distribution of fragment ions, which was exactly what was needed for the planned alignment experiments.

No such angular anisotropy was, however, detected in the I^+ images. Instead, they were circularly symmetric, independent of whether the probe pulse polarization was parallel or perpendicular to the detector. The explanation, we believe, was that each droplet was doped with multiple molecules, which then formed dimers, trimers and even larger clusters. In these oligomers, the C-I axes are not necessarily parallel, and the polarizability tensors could become more isotropic than for the monomers. This would strongly reduce the alignment-dependence of the strong-field ionization. An obvious follow-up question is to ask why the droplets picked up several molecules. We believe that this was because the pulsed nozzle produced very large droplets, with a size of $10^5 - 10^6$ He atoms per droplet [144]. The sheer size of these droplets gives them a very large cross section for picking up molecules or atoms. In principle, the multiple doping can be avoided by lowering the doping pressure so much that each droplet picks up at most one molecule. We tried to enter this regime but at the lowest doping pressure, where the I^+ signal was detectable, the I^+ images remained isotropic. We believe this was a consequence of the low droplet number density, resulting from their large size. The upshot was that for these large droplets, in the single doping regime there are so few doped droplets that they cannot produce detectable ion signals.

As a consequence of the lack of success with the pulsed valve, the experimental setup was instead equipped with a continuous nozzle of the Göttingen design [149, 150], manufactured by Alkwin Slenczka at Regensburg University. Figure 9.13 shows IHe^+ images recorded when He droplets from this new source, doped with either MeI (top row) or IB molecules (bottow row) are irradiated by the probe pulse.[8] When the probe pulse is polarized perpendicular to the detector, Fig. 9.13 (a), (c), the image is circularly symmetric which is to be expected if the molecules are randomly oriented. When the polarization is parallel to the detector plane, Fig. 9.13 (b), (d), the images develop an anisotropy with the ions being confined along the polarization direction. We interpret this as a result of the alignment-dependent strong-field ionization, well-known for isolated molecules, mentioned above. The measurements were repeated for both somewhat higher and somewhat lower doping pressures. No changes were observed in the angular distributions of the IHe^+ ions indicating that the experiment took place under single-doping conditions, where each droplet was doped with at most one molecule.

Next, the nonadiabatic alignment experiment was carried out. The experiment was first conducted on isolated MeI molecules provided by the molecular beam. Similar to the I_2 experiment described in Sect. 9.2.5, the 450 fs alignment pulse was linearly polarized parallel to the detector while the 30 fs probe was polarized perpendicular to the detector. Examples of I^+ images at $t = 0.3$ ps and $t = 33.6$ ps are shown in Fig. 9.14 (a2), (a3). An image obtained with only the probe pulse present is included as a reference, Fig. 9.14 (a1). In the image at $t = 0.3$ ps, the ions are

[8] We prefer to detect IHe^+ ions because I^+ ion images may contain a small contribution from unsolvated molecules drifting from the pickup cell to the target region. Although the experimental setup is designed to make this contribution very small, the detection of IHe^+ ions ensures background-free conditions.

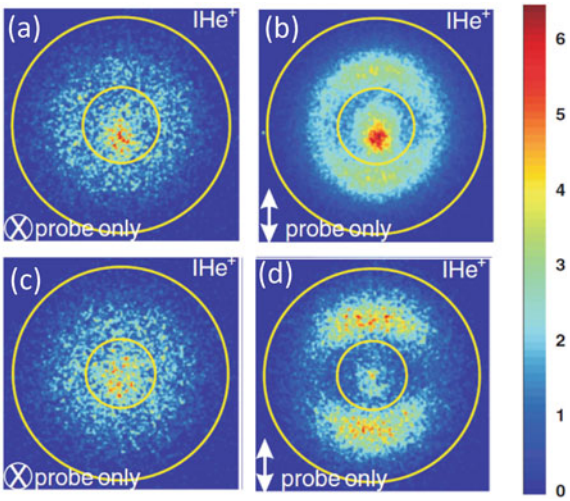

Fig. 9.13 2D velocity images of IHe^+ resulting from irradiation of He droplets doped with either methyl iodide (top row) or iodobenzene (bottow row) molecules by a 30 fs long probe pulse. The polarization direction of the linearly polarized probe pulse is indicated on each panel. $I_{\text{probe}} = 1.8 \times 10^{14}$ W/cm^2. No alignment pulse was included. Adapted from [148] with permission from American Physical Society (APS). Copyright (2013) by APS

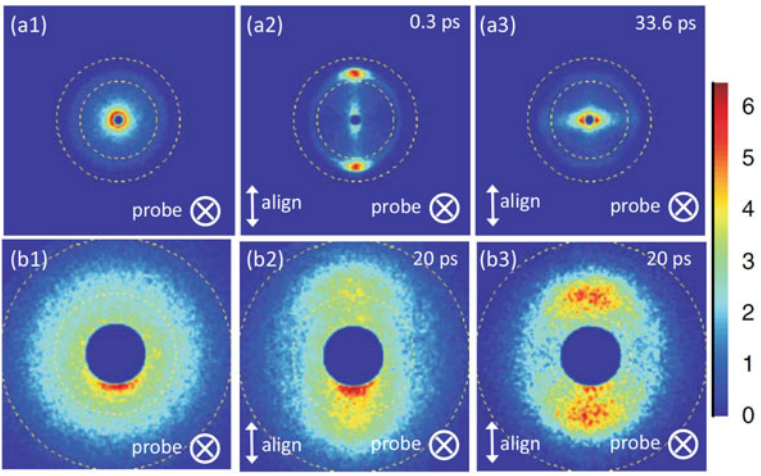

Fig. 9.14 2D velocity images of I^+ ion images resulting from irradiation of CH_3I molecules with the probe pulse [(b3): IHe^+ ions]. Top (bottom) row: Isolated (He-solvated) molecules. (a1) and (b1): Probe pulse only. In the other images, the alignment pulse is included, its polarization direction indicated by the double headed arrows. The probe time is also given on the panels. $I_{\text{align}} = 1.2 \times 10^{13}$ W/cm^2

localized along the polarization of the alignment pulse whereas at t = 33.6 ps the localization is perpendicular to the polarization vector. This demonstrates alignment and anti-alignment, respectively. As for the gas phase I_2 experiment in Sect. 9.2.5, we determined $\langle\cos^2\theta_{2D}\rangle$ from the ion hits in the radial range (in between the two yellow circles) corresponding to the directional Coulomb explosion channel, here I^+-CH_3^+.

The time-dependence of $\langle\cos^2\theta_{2D}\rangle$, shown by the black curve in Fig. 9.15, has a structure similar to that observed for the I_2 gas phase molecules, Fig. 9.9, i.e. narrow, periodically occurring alignment transients identified as the prompt alignment peak (t = 0.3 ps), the half revivals (t = 0.3 ps + $(N - \frac{1}{2})T_{rev}$) and the full revivals (t = 0.3 ps + NT_{rev}), where $T_{rev} = 1/2B$ and $N = 1, 2, 3, \ldots$ [146]. Hereafter, the molecular beam with the isolated MeI molecules was blocked and instead the doped He droplet beam was let into the target chamber. The laser beams were left untouched to ensure that the parameters of the alignment and the probe pulses were well-suited for inducing and observing laser-induced nonadiabatic alignment.

Figure 9.14 (b2) shows an I^+ image, recorded at t = 20 ps. The most important observation is that the ions are confined along the alignment pulse polarization showing that the MeI molecules are aligned at that time. A similar confinement is also present in the IHe^+ image displayed in Fig. 9.14 (b3). Compared to the gas phase results, the radial (velocity) distribution is broader, which could be caused by the fragments ions scattering on, and thus exchanging energy and momentum with, the He atoms on their way out of the droplets. Also, the probe laser may ionize some He atoms in the vicinity of the MeI molecule. The repulsion between such He^+ ions and the I^+ fragment ions will add kinetic energy to the latter. To account for the larger velocity range of the I^+ (or IHe^+) fragment ions, a larger radial range (in between the yellow circles) was employed to determine $\langle\cos^2\theta_{2D}\rangle$. Note that the ion distributions in the three images, Fig. 9.14 (b1)–(b3) are slightly offset from the image center. This shift results from the fact that the He droplet beam propagates parallel to the detector whereas the molecular beam with the isolated molecules propagates perpendicularly to the detector, see Figs. 9.14 (a) and 9.5.

The time-dependence of $\langle\cos^2\theta_{2D}\rangle$ for the MeI molecules in He droplets is represented by the red curve in Fig. 9.15. The curve rises to a maximum of 0.60 at $t \sim$ 20 ps, whereupon it decreases to 0.50, the $\langle\cos^2\theta_{2D}\rangle$ value for randomly oriented molecules, at $t \sim$ 110–120 ps. Hereafter $\langle\cos^2\theta_{2D}\rangle$ remains flat at 0.50 until the end of the recording time, 1000 ps. At the time this experimental result was obtained and published, it seemed at odds with the expectations mentioned above. Most strikingly, there were no revivals observed. Also, the degree of alignment was significantly below that found for isolated molecules with an identical alignment pulse. As we explain in the next section, experiments at much lower intensities and on other molecular species were needed to understand laser-induced rotational dynamics of molecules in He nanodroplets.

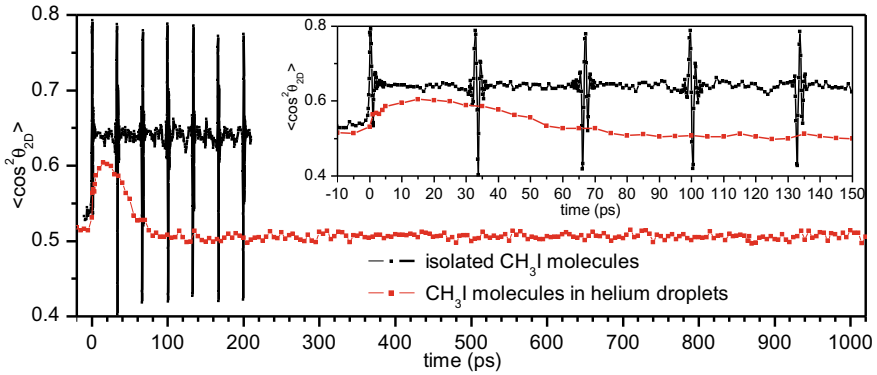

Fig. 9.15 Time dependence of $\langle \cos^2 \theta_{2D} \rangle$ for isolated CH_3I molecules (black squares) and for CH_3I molecules in He droplets (red squares). The alignment and the probe pulse parameters are identical for the two data series. $I_{\text{align}} = 1.2 \times 10^{13}$ W/cm^2. The inset expands on the first 150 ps. Reproduced from [151] with permission from American Physical Society (APS). Copyright (2013) by APS

9.3.3 *Nonadiabatic Alignment in the Weak-Field Limit: Free Rotation (Reconciling the Time and the Frequency Domains)*

In the first part of this section, we describe nonadiabatic alignment experiments on OCS molecules in He droplets. Their rotational energy structure has been characterized by IR and MW spectroscopy, thereby making OCS an ideal case for comparing, and hopefully reconciling, results from time-resolved alignment dynamics with results from frequency-resolved spectroscopy. Infrared and microwave spectroscopy have shown that the energy, E_{rot}, of the five lowest rotational levels are given by:

$$E_{rot} = BJ(J+1) - DJ^2(J+1)^2 \tag{9.9}$$

where J is the rotational angular momentum quantum number and $B = 2.19$ GHz and $D = 11.4$ MHz [152]. The reason that no higher J-states are explored is the combination of the fact that at a temperature of 0.4 K only $J = 0, 1, 2, 3$ are significantly populated and that the selection rules for the transitions driven by the IR or MW radiation is $\Delta J = \pm 1$. The gas phase-like rotational energy-level structure given by Eq. 9.9 builds the expectation that a short, nonresonant laser pulse can make a superposition of these states and thus initiate coherent rotational dynamics in a similar way to what has been done with isolated molecules.

The experimental procedure of our OCS experiment was similar to that described for MeI in Sect. 9.3.2 except that the alignment pulses were 15 ps long and the fragment ions detected were S^+ ions. The black curves in Fig. 9.16 (a1)–(c1) show the time-dependence of $\langle \cos^2 \theta_{2D} \rangle (t)$ recorded at three different values of the fluence.

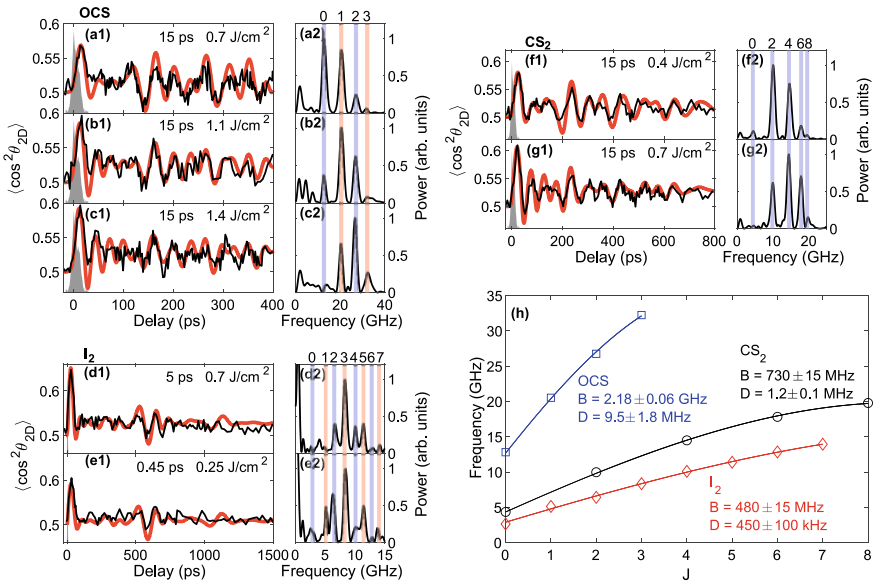

Fig. 9.16 **a**1–**g**1: The time dependence of $\langle \cos^2 \theta_{2D} \rangle$ for OCS, CS_2 and I_2 molecules at different durations and fluences of the alignment pulse, given on each panel. Black (red) curves: experimental (simulated) results. The intensity profile of the alignment pulses are shown by the shaded grey area. **a**2–**g**2: The power spectra of the corresponding $\langle \cos^2 \theta_{2D} \rangle$ traces. The spectral peaks, highlighted by the colored vertical bands, are assigned as $(J–J+2)$ coherences with J given on top of the panels (blue: even, red: odd). **h**: Central frequencies of the $(J–J+2)$ peaks in the power spectra versus J. The full lines represent the best fits using Eq. 9.10. The B and D constants from the fits are given for each molecule. Adapted from [153] with permission from American Physical Society (APS). Copyright (2020) by APS

All three alignment traces reach a maximum shortly after the alignment pulse, which is followed by oscillations with a gradually decreasing amplitude. At first glance, the three curves may appear noisy and rather uninformative but this impression changes when one views the corresponding power spectra obtained by Fourier transformation of $\langle \cos^2 \theta_{2D} \rangle(t)$. The power spectra contain discrete peaks just as for the spectra of the gas phase I_2 molecules presented in Fig. 9.10.

In Sect. 9.2.5, we described how the spectral peaks reflect the frequencies of the nonzero matrix elements $\langle JM| \cos^2 \theta_{2D} |J'M\rangle$—the coherence (coupling) between state $|JM\rangle$ and $|J'M\rangle$, where M is the projection of the angular momentum on the polarization axis of the alignment pulse. From Eq. 9.9 the frequencies corresponding to the dominant $\Delta J = J' - J = 2$ coherences [65], labeled $(J–J+2)$, are given by:

$$\nu_{(J–J+2)} = B(4J + 6) - D(8J^3 + 36J^2 + 60J + 36). \tag{9.10}$$

Using Eq. 9.10 the three peaks in Fig. 9.16 (a2) at 12.8, 20.6 and 27.2 GHz are assigned as pertaining to the (0–2), (1–3) and (2–4) coherences, respectively. The spectra for the two higher fluences, Fig. 9.16 (b2)–(c2) contain the same spectral

peaks as illustrated by the vertical colored bands. At $F_{\text{align}} = 1.4\,\text{J/cm}^2$, an extra peak shows up at 32.3 GHz. This peak is assigned as the (3–5) coherence. It can be seen that the weight of the spectral peaks shift to higher frequencies as the fluence is increased. The same observation was made for the nonadiabatic alignment meaurements on I_2 molecules, see Fig. 9.10. As mentioned, the classical explanation of the shift is that a stronger alignment pulse imparts more angular momentum to the molecule, which will then lead to higher rotational frequencies. Now the central positions of the four peaks in the spectra can be plotted as a function of J and fitted using Eq. 9.10 with B and D as the fitting parameters. The experimental points along with the best fit, obtained for $B = 2.18 \pm 0.06\,\text{GHz}$ and $D = 9.5 \pm 1.8\,\text{MHz}$, are shown in Fig. 9.16 (h). These findings agree well with the values from IR spectroscopy, $B = 2.19\,\text{GHz}$ and $D = 11.4\,\text{MHz}$, where D was the average for the v=0 and v=1 vibrational states in the IR transition [152].

From this we can draw two conclusions. Firstly, the excellent fitting of Eq. 9.10 to the positions of the spectral peaks strongly indicates that laser-induced rotation of OCS molecules in He droplets is well described by a gas phase model, employing the effective B and D constants, when the rotational excitation is modest, here $J \leq 5$. This point is further discussed in the next paragraph. Secondly, the rotational structure of a He-solvated molecule is encoded in $\langle\cos^2\theta_{2D}\rangle(t)$ and the rotational constants can be retrieved by Fourier transformation. This introduces nonadiabatic alignment as a rotational coherence spectroscopy method for molecules embedded in He nanodroplets. Examples for molecules other than OCS will be given below.

To test how well a gas phase model describes the observed alignment dynamics, we calculated $\langle\cos^2\theta_{2D}\rangle(t)$ by solving the time-dependent rotational Schrödinger equation for a linear molecule exposed to the 15 ps alignment pulse, using the experimental pulse shape, and the B and D values from the fit. The calculations were averaged over the initially populated rotational states, given by a Boltzmann distribution with $T = 0.37\,\text{K}$, and over the focal volume determined by the measured beam waists of the alignment ($\omega_0 = 30\,\mu\text{m}$) and probe beams ($\omega_0 = 25\,\mu\text{m}$). Also, the effect of inhomogeneous broadening was implemented by a Gaussian distribution of the B constants with a FWHM, (ΔB) of 90 MHz and a constant B/D ratio. The distribution of B constants can arise from differences in droplet sizes and shapes, the location of the molecule inside a droplet and coupling of the rotation and centre-of-mass motion of the molecule [154]. The value of ΔB was taken as half of the width, W, of the J: $1-0$ transition in a MW spectroscopy experiment on OCS molecules in He droplets [155].

The red curves in Fig. 9.16 (a1)–(c1) show the calculated degree of alignment. The simulated $\langle\cos^2\theta_{2D}\rangle$ values were scaled by a factor of 0.3, symmetrically centered around $\langle\cos^2\theta_{2D}\rangle = 0.5$, to account for the non-axial recoil of the S^+ ions from the Coulomb explosion of the OCS molecules [63]. The calculated $\langle\cos^2\theta_{2D}\rangle(t)$ is very close to the measured trace and captures in detail most of the oscillatory patterns observed. The very good agreement between the calculated and experimental data corroborates the previous conclusion that gas phase modelling with effective B and D constants can accurately describe ps laser-induced rotational dynamics of OCS molecules in He droplets. Nevertheless, the observed dynamics appear very different

from that of isolated molecules. As discussed below, this is due to the much larger D constant for molecules in He droplets compared to isolated molecules (OCS: $D_{He} \approx 6.5 \times 10^3 D_{gas}$) [152, 156] and the presence of inhomogeneous broadening.

For the OCS molecules aligned with the 15 ps pulse, we calculated $\langle \cos^2 \theta_{2D} \rangle(t)$ for three values of the D constant, with or without the effect of inhomogeneous broadening. When $D = 0$ and all molecules have the same B value, i.e. no inhomogeneous broadening, Fig. 9.17 (a1) shows that $\langle \cos^2 \theta_{2D} \rangle(t)$ is identical to that of isolated OCS molecules except that the revival period is increased by a factor 2.8 due to the effective B constant. The calculation for $D = 5.0$ MHz, Fig. 9.17 (b1), shows that the centrifugal term introduces an additional oscillatory structure in $\langle \cos^2 \theta_{2D} \rangle(t)$ and distorts the shape of the revivals. For gas phase molecules, it was already observed and understood that the centrifugal term modulates the shape of rotational revivals [115, 157] but the influence was moderate [9] and the different revivals remained separated from each other. In Fig. 9.17 (b1), the effect of the centrifugal term is so large that, with the exception of the half-revival, there is essentially no longer distinct, separated revivals. This trend is even more pronounced for the calculation with the experimental D value, Fig. 9.17 (c1). The yellow and blue bands provide a rigid rotor reference, Fig. 9.17 (a1), for how the centrifugal term distorts and shifts the rotational revivals.

The panels in the right column of Fig. 9.17 show $\langle \cos^2 \theta_{2D} \rangle(t)$ when inhomogeneous broadening is included by averaging calculated alignment traces over a Gaussian distribution of B constants with a FWHM width of 90 MHz. The main influence is a gradual reduction of the amplitude of the oscillations in the alignment traces while preserving the average value of $\langle \cos^2 \theta_{2D} \rangle$. This dispersion effect produces alignment traces which (for $D = 9.5$ MHz) agree very well with the experimental results for all three fluences studied, see Fig. 9.16 (a1)–(c1).

Experiments were carried out for two other linear molecules, CS_2 and I_2. The alignment traces and the corresponding power spectra are displayed in Fig. 9.16 panels (d)–(g).[10] Again, each spectral peak is assigned to a $(J–J+2)$-coherence, noting that for CS_2 only even J-states are possible due to the nuclear spin statistics. The center of the spectral peaks are plotted versus J and as for OCS, Eq. 9.10 provides excellent fits to the experimental results, illustrated by the red (I_2) and blue (CS_2) points/lines in Fig. 9.16 (h). The B and D values extracted from the best fits are given on the figure. No other experimental values from frequency resolved spectroscopy are available in the literature but a recent path integral Monte Carlo (PIMC) simulation gives $B = 756 \pm 9$ MHz, in good agreement with the experimental value. For the case of CS_2, IR spectroscopy could have been used to determine B and D, just as it has been used for CO_2 [159]. For I_2, however, neither IR nor MW would apply because I_2 neither has a permanent dipole moment, nor a dipole moment that changes during vibration.

[9] Unless extreme rotational states, excited by an optical centrifuge, are populated [158].

[10] The I_2 results shown were obtained for alignment pulse durations of 450 fs and 5 ps. Measurements were also carried out at 15 ps showing spectral peaks at the same positions.

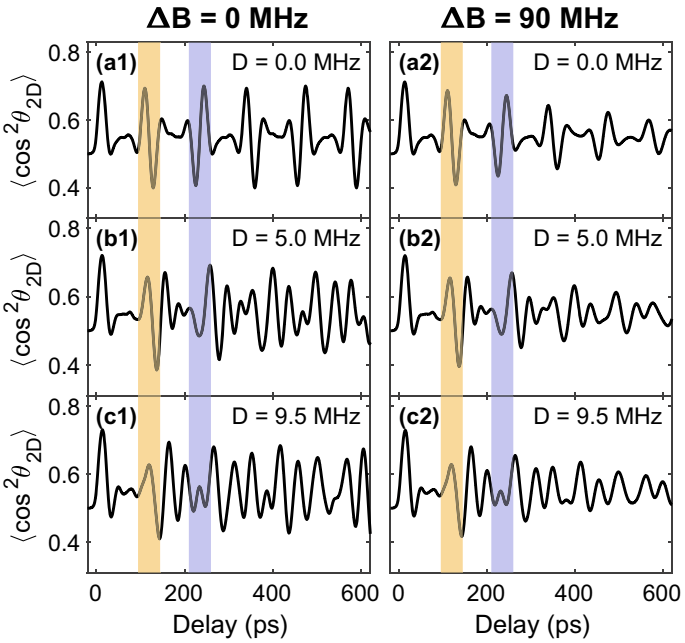

Fig. 9.17 $\langle \cos^2 \theta_{2D} \rangle$ as a function of time calculated for OCS (B=2.17 GHz) for three different values of the D constant, without (left column) or with (right column) inhomogeneous broadening included. T = 0.37 K and F = 0.7 J/cm^2. The yellow and blue bands highlight the position of the half-and full-revival for the D=0 case. Reproduced from [153] with permission from American Physical Society (APS). Copyright (2020) by APS

We also calculated the time-dependent degree of alignment for I_2 and CS_2. As for OCS, it was necessary to scale the simulated data to account for non-axial recoil. The scaling factor was 0.37 for CS_2 and 0.75 for I_2. The calculated results, shown by the red curves in Fig. 9.16 panels (d1)–(g1) agree very well with the experimental findings. Since the two molecules had not been spectroscopically studied in He droplets before, we had to choose a width for the inhomogeneous distribution of the B constant. The best agreement with the measured $\langle \cos^2 \theta_{2D} \rangle(t)$ was obtained for ΔB = 50 MHz for CS_2 and 40 MHz for I_2. As for OCS, we also did calculations where the D constant was varied from 0 to the experimental value - 1.2 MHz for CS_2 and 450 kHz for I_2. The result of these calculations, that are not shown here, identify the valley-peak structure around t = 200 ps for CS_2 as the quarter revival and the oscillatory structure in the 550–700 ps range for I_2 as the half revival.

Based on the excellent agreement between the measured and calculated $\langle \cos^2 \theta_{2D} \rangle(t)$ for the three different molecules, we conclude that for the relatively weak, nonresonant fs or ps pulses used, the mechanism of nonadiabatic alignment is the same for molecules in He droplets as for isolated molecules. This means that first the polarizability interaction between the laser pulse and the He-solvated

molecule creates a rotational wave packet. The interaction strength is essentially the same as for an isolated molecule because for a given laser pulse intensity, it is only determined by the polarizability anisotropy of the molecule.[11] The rotational wave packet will, however, be different because the rotational energy levels are not the same for the He-solvated molecules as for the isolated molecules. In fact, the orders-of-magnitude larger D values for the He-solvated molecules cause a strong dispersion of $\langle\cos^2\theta_{2D}\rangle(t)$ making only the first fractional revivals identifiable. This is in stark contrast to the gas phase case where a large number of revivals are observable. Furthermore, the distribution of B (and D) values also contrasts the gas phase case where B and D are defined by the molecular structure only. The inhomogeneous B-distribution causes a gradual decay of the amplitude of the oscillations in the $\langle\cos^2\theta_{2D}\rangle$ trace.

One question remains, namely why is the rotational structure of the He-solvated molecules gas phase-like for the lowest rotational states? We believe this is a consequence of the superfluidity of the He droplets. According to the power spectra, shown in Fig. 9.16, the maximum J values and thus rotational energies, E_{rot}(Eq. 9.9), are the following: OCS: $J = 5$, $E = 1.9\,\mathrm{cm}^{-1}$; CS_2: $J = 10$, $E = 2.2\,\mathrm{cm}^{-1}$; I_2: $J = 9$, $E = 1.3\,\mathrm{cm}^{-1}$. In all three cases, E_{rot} falls in the regime where the density of states in the He droplets is low and thus the coupling between molecular rotation and the phonons (rotons) of the He droplet should be weak [53]. If stronger alignment pulses are applied, we expect that higher rotational states will be excited. Then the free-rotor description is probably no longer valid since the density of states in the He droplet increases strongly, implying that the coupling of rotation to the phonons (rotons) increases, which in turn will make the lifetime of highly excited rotational states (very) short [160]. We note that it is unlikely that Eq. 9.9 will provide accurate or meaningful descriptions of highly-excited rotational states. In the case of OCS, Eq. 9.9 predicts negative energies for J > 9, which is unphysical.

9.3.4 *Nonadiabatic Alignment in the Strong-Field Limit: Breaking Free*

To illustrate how increasing the alignment intensity influences the alignment dynamics of molecules in He droplets, we use experimental results for the I_2 molecule. The experimental strategy was identical to that described above. An alignment pulse, linearly polarized parallel to the detector and with a duration τ_{align} = 450 fs, initiates the rotational dynamics, whereupon the delayed probe pulse, I_{probe} = $3.7 \times 10^{14}\,\mathrm{W/cm}^2$, Coulomb explodes the molecules and IHe^+ ion images are recorded. The time-dependence of $\langle\cos^2\theta_{2D}\rangle$ obtained from these images, for nine different fluences, is shown in Fig. 9.18. The alignment trace recorded at the lowest fluence, $F_{\mathrm{align}} = 0.25\,\mathrm{J/cm}^2$, is the same as the one displayed in Fig. 9.16 (e1) and it

[11] The He atoms in the shell will also be polarized but the polarizability is isotropic.

shows the characteristic peak shortly after the alignment pulse and the half-revival at around 550–700 ps.

As F_{align} is increased to 0.50 and then to 1.2 J/cm^2 the prompt alignment peak grows in amplitude and appears earlier. This is the same behavior seen for OCS in He droplets, Fig. 9.16 panels (a1)–(c1) and for the isolated I_2 molecules, Fig. 9.9, and is the result of excitation of higher rotational states, and thus faster rotation and higher degree of alignment. The half-revival structure remains F_{align} = 0.50 and 1.2 J/cm^2, although its amplitude decreases somewhat. The spectra, obtained by Fourier transformation (not shown) corroborate that the increase of F_{align} leads to higher frequencies of the rotational wave packet. At F_{align} = 1.2 J/cm^2 , the spectrum shows a clustering of the frequencies in a peak around 18–19 GHz. When F_{align} is further increased to 2.5 and 3.7 J/cm^2, the revival structure disappears from the time traces, as seen in Fig. 9.18 (d1)–(e1). Unlike the gas phase case, the frequencies in the spectrum do not shift to higher frequencies but rather stay below 20 GHz. We are currently analyzing this phenomenon and its relation to the phonon (roton) excitations of the He droplet. Here, we will instead focus on another non-gas phase phenomenon. Up to F_{align} = 2.5 J/cm^2 the rising part of the prompt peak is smooth and increases faster as F_{align} is increased. At F_{align} = 3.7 J/cm^2 the rising part changes qualitatively to become much steeper and even develops a small substructure - see the right column of Fig. 9.18 for a zoom-in on the first 100 ps. This trend continues when F_{align} is further increased and the substructure grows to a prominent sharp peak ending with a maximum already at $t \sim 1.3$ ps for F_{align} = 8.7 J/cm^2, see Fig. 9.18(i).

This initial dynamics are almost as fast as for an isolated molecule, which can be seen on Fig. 9.19 where the $\langle \cos^2 \theta_{2D} \rangle$ trace during the first 20 ps is shown for both He-solvated molecules and isolated molecules. The maximum of the prompt peak appears at close to the same time in the two cases. We believe the reason for these rapid dynamics of the He-solvated molecules is that the I_2 molecules transiently decouples from their He solvation shell. The explanation for the decoupling is that the interaction with the alignment pulse induces a rotational speed of the He-solvated molecules that is so high that the He atoms in the solvation shell detach from the molecule due to the centrifugal force.

To substantiate our explanation, we use the classical delta-kick model, Eq. 9.7, to calculate the angular velocity that a He-dressed I_2 molecule gains from the interactions with the laser pulse using the effective moment of inertia, I_{eff}, of I_2 in the droplets. According to the experimental result in Sect. 9.3.3, I_{eff} is equal to 2.3 times the moment of inertia of a gas phase molecule. In our classical model, a He-dressed molecule is treated as an I_2 molecule rigidly attached to eight He atoms placed in the minima of the I_2–He potential [152, 162]. This means six He atoms in the central ring around the molecule at a distance, r_{He}, of 3.7 Å from the center of the molecule and one He atom at each end, at r_{He} = 5.0 Å, see Fig. 9.20. We note that the value of I_{eff} determined from this structure (Fig. 9.20) gives $I_{\text{eff}} = 1.8 I_{\text{gas}}$. If two He atoms are placed at each end of the molecule, then $I_{\text{eff}} = 2.3 I_{\text{gas}}$.

A simple criterion for estimating if a He atom in the solvation shell can be detached is: $E_{\text{rot}}(\text{He}) > E_{\text{binding}}(\text{He})$, where $E_{\text{rot}}(\text{He}) = \frac{1}{2} m_{\text{He}} r_{\text{He}}^2 \omega^2$ is the rotational energy of a He atom and $E_{\text{binding}}(\text{He}) \approx 16$ cm^{-1} is the ground-state binding energy of the

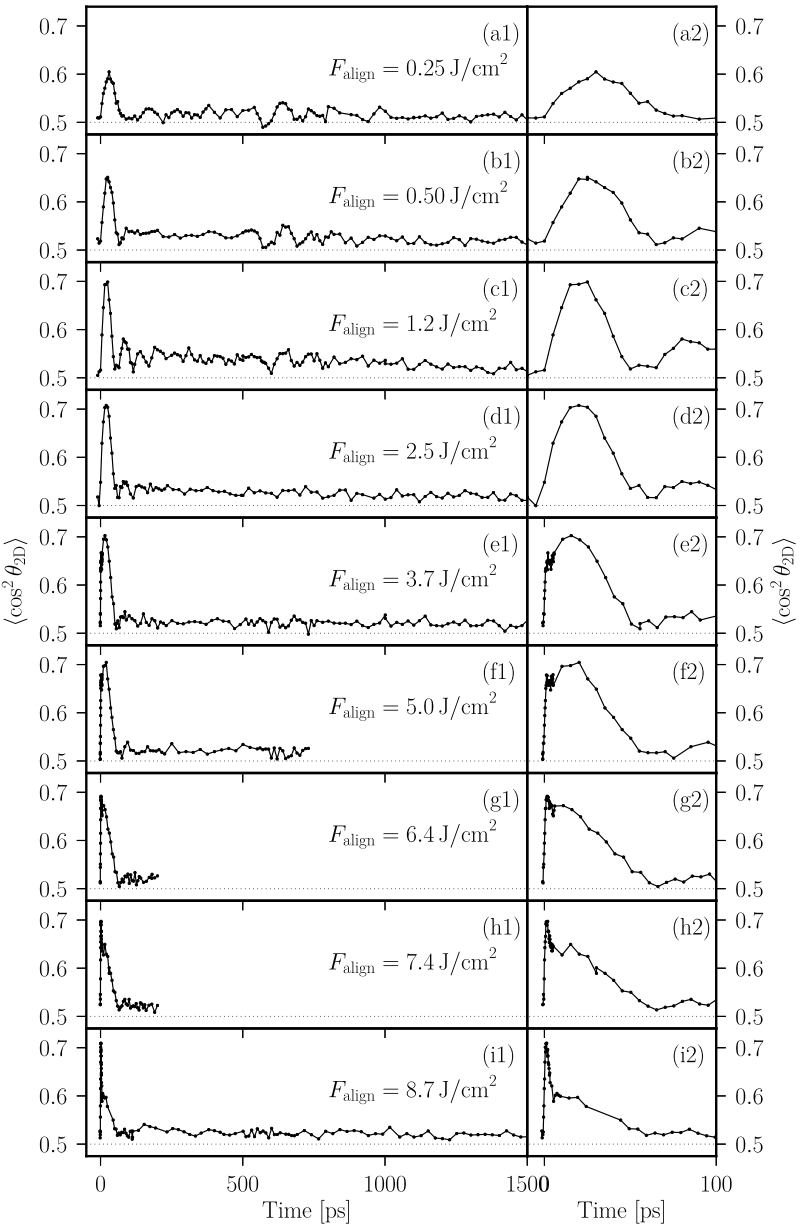

Fig. 9.18 Time-dependence of $\langle\cos^2\theta_{2D}\rangle$ for I_2 molecules in He droplets at 9 different fluences of a 450 fs alignment laser pulse. The rightmost panels show a zoom of the first 100 ps. Adapted from [161] with permission from American Physical Society (APS). Copyright (2017) by APS

HeI_2 complex [162, 163]. Table 9.2 displays E_{rot}(He) calculated for the different fluences. For the value of r_{He} we have taken 5.0 Å. At $F_{kick} \gtrsim 6\,J/cm^2$ the criterion is met implying that one or several He atoms detach from the molecule (lower panels in Fig. 9.20) since the binding energies of the first few He atoms are similar [164]. If one He atom is detached, the angular velocity of the I_2 molecule and its remaining He solvent atoms will increase, which causes detachment of more He atoms and then another increase in ω etc. It is likely that this self-reinforcing process can lead to rapid detachment of all the He atoms in the solvation shell. A schematic representation of the rotational dynamics in the high fluence limit, where the detachment process occurs, and in the low fluence limit where the molecule and its solvated shell rotates as a concerted system, is shown in Fig. 9.20 (Table 9.2).

Similar rapid, short-time alignment dynamics were also observed for OCS and CS_2 molecules in He droplets. Figure 9.21 shows the time-dependent alignment dynamics for OCS and CS_2 molecules, in both cases induced by a 450 fs alignment pulse and probed by Coulomb explosion and recording of the S^+ fragment ions. The red curves in Fig. 9.21 are obtained for He-solvated molecules. The traces for both OCS and CS_2 resemble that of I_2 at $F_{align} = 8.7\,J/cm^2$—a sharp initial spike of $\langle\cos^2\theta_{2D}\rangle$ followed by a decay over ~50–60 ps to the equilibrium value of 0.5. The $\langle\cos^2\theta_{2D}\rangle(t)$ traces for isolated molecules in the supersonic beam are shown as references. The right panels in Fig. 9.21 compare the alignment dynamics of He-solvated molecules to

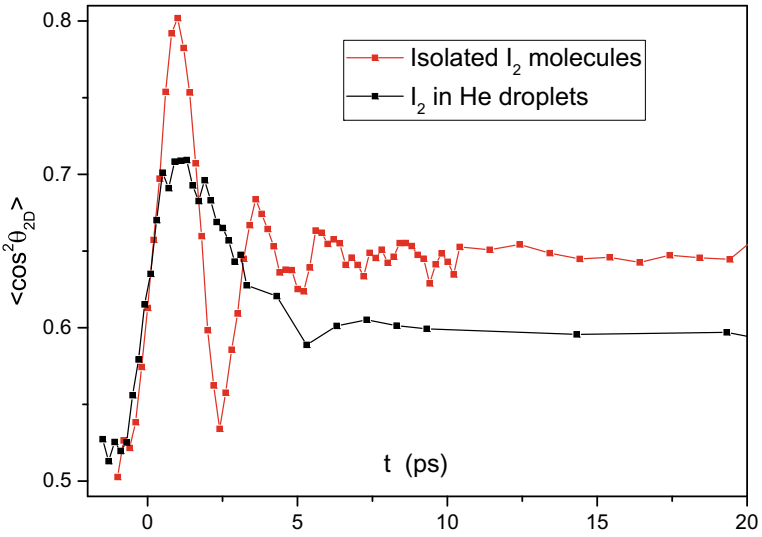

Fig. 9.19 $\langle\cos^2\theta_{2D}\rangle$, at early times for isolated I_2 molecules (red) and I_2 molecules in He droplets (black) recorded for $F_{align} = 8.7\,J/cm^2$. The parameters of the alignment pulse and the probe pulse were identical for the measurements on the isolated molecules and on the molecules in He droplets. Adapted from [161] with permission from American Physical Society (APS). Copyright (2017) by APS

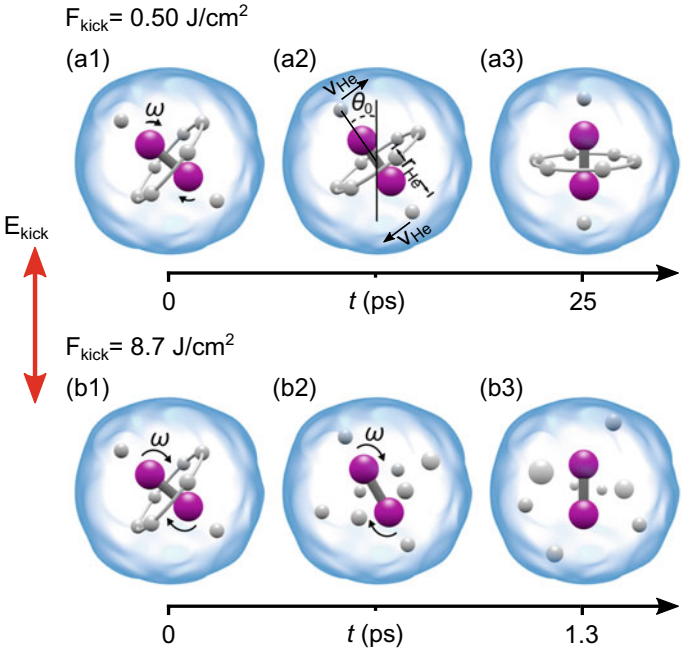

Fig. 9.20 Schematic illustration of laser-induced rotation of I_2 molecules inside He droplets, based on the classical model described in the text, for a weak [(a1)–(a3)] and a strong [(b1)–(b3)] alignment pulse. **a**2 illustrates parameters used in the classical model. θ_0: The starting angle between the molecular axis and the alignment pulse polarization, r_{He}: Distance from the He atom at the ends to the axis of rotation, $v_{He} = \omega\, r_{He}$: The linear speed of the He atoms at the ends of the molecule gained from the laser-molecule interaction. Reproduced from [161] with permission from American Physical Society (APS). Copyright (2017) by APS

Table 9.2 Classical calculation of the maximum angular velocity using Eq. (9.7) with $\theta_0 = 45°$ for the nine different fluences used in the experiment. From ω the linear speed, v_{He}, and the rotational energy, E_{rot}(He), of the He atoms at the ends of the molecules are calculated—see text

F_{align}, J/cm ^{2}	ω, 10^{10} Hz	v_{He}, m/s	E_{rot}(He), cm^{-1}
0.25	2.7	13	0.029
0.50	5.5	26	0.12
1.2	14	65	0.71
2.5	27	130	2.8
3.7	41	195	6.4
5.0	54	260	11
6.4	70	338	19
7.4	81	390	26
8.7	95	454	35

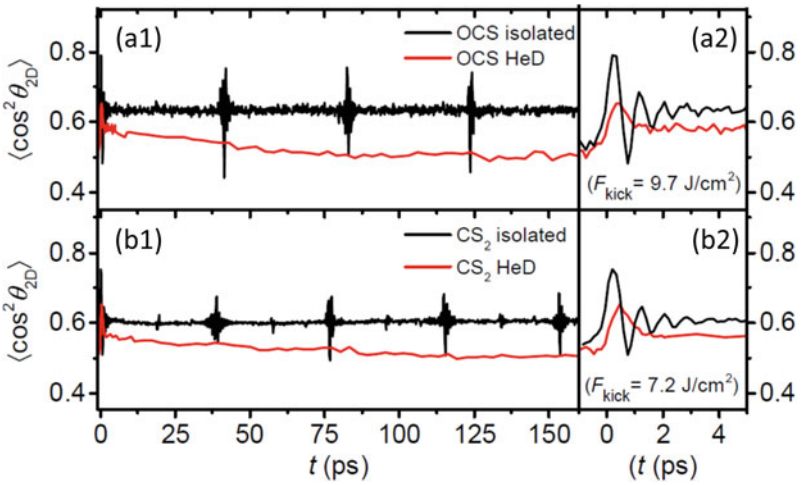

Fig. 9.21 $\langle \cos^2 \theta_{2D} \rangle$(t) for isolated (black curves) and He-solvated molecules (red curves). Upper row: OCS with $F_{\text{align}} = 9.7\,\text{J/cm}^2$. Lower row: CS_2 with $F_{\text{align}} = 7.2\,\text{J/cm}^2$. The parameters of the alignment pulse and the probe pulse were identical for the measurements on the isolated molecules and on the molecules in He droplets. The rightmost panels show a zoom of the first 5 ps

that of isolated molecules during the first 5 ps. It is seen that $\langle \cos^2 \theta_{2D} \rangle$ evolves almost as fast for the molecules in He droplets as for the gas phase molecules. Repeating the classical calculation for OCS and CS_2 with the effective moment of inertia determined in Sect. 9.3.3, shows that the alignment pulse at the fluences used makes the He-solvated molecules rotate so fast that the He atoms will be detached, in an analogous way to the I_2 case just discussed. We note that a quantum model of the laser-induced rotational dynamics of a CS_2 molecule weakly bonded to a single He atom, gives almost the same value for the alignment laser pulse intensity (fluence) needed to dissociate the system [165, 166].

9.3.5 Adiabatic Alignment of Molecules in He Nanodroplets

In this section, we discuss alignment induced by laser pulses with a duration of 160 ps. We first describe experiments conducted on I_2 molecules in He droplets. In Sect. 9.2.4, it was already mentioned that although 160 ps is shorter than the rotational period ($1/2B = 446$ ps) for isolated molecules, the degree of alignment exhibited adiabatic behavior, i.e. $\langle \cos^2 \theta_{2D} \rangle(t)$ followed the temporal intensity profile of the alignment pulse. Encouraged by those results, we used the same 160 ps pulses to explore alignment of He-solvated I_2 molecules although their moment of inertia is 2.3 times higher than for the isolated molecules.

The experiment was conducted in the same way as for the isolated molecules, but using IHe^+ ions as the observables rather than I^+ ions. Images of IHe^+ with the probe pulse only and with the probe pulse synchronized to the peak of the alignment pulse are shown in Fig. 9.6 (b1) and (b2). In the latter case, the ions are strongly localized around the polarization direction of the alignment pulse, showing that the molecules are strongly 1D aligned. The degree of alignment, $\langle\cos^2\theta_{2D}\rangle$, is determined from the ions in the radial range between the two white circles. These ions result from double ionization of the I_2 molecules and subsequent Coulomb explosion into two I^+ ions, each of which then picks up a single He atom. This assignment is based on the angular covariance map, determined from the ions between the two white circles, displayed in Fig. 9.6 (c1). The two covariance signals centered at (0°, 180°) and (180°, 0°) identify the ions as originating from double ionization of the I_2 molecules and fragmentation into a pair of correlated IHe^+ ions. The length of the covariance signals is small, thus showing that the molecules are well-aligned, but the width, $\sim 11°$, is much larger than in the case of the isolated molecules. We believe the increased width is due to distortion of the ion trajectories from collisions with He atoms on the way out of the droplet. The angular distribution of the IHe^+ ions is therefore wider than the distribution of the molecular axes and represents an underestimate of the true degree of alignment. As is discussed below, we can deconvolute the effect of the deviation from axial recoil in the probe process using analysis of the angular covariance maps [69].

The time-dependence of $\langle\cos^2\theta_{2D}\rangle(t)$ is shown by the black line in Fig. 9.7. It is seen that $\langle\cos^2\theta_{2D}\rangle(t)$ follows the shape of the laser pulse (shaded grey area). Compared to the gas phase results (blue line) the $\langle\cos^2\theta_{2D}\rangle$ curve is, however, slightly shifted to later times. Additionally, upon turn-off of the alignment pulse $\langle\cos^2\theta_{2D}\rangle(t)$ does not return to 0.50. As for the gas phase molecules, this means that the He-solvated molecules are left in a coherent superposition of rotational states after the pulse. In fact, measurements at times out to 1500 ps reveal clear revival structures [51]. Like for the isolated molecules we omit any discussion of these nonadiabatic effects and concentrate on the maximum degree of alignment obtained at the peak of the alignment pulse.

The black open circles in Fig. 9.8 shows $\langle\cos^2\theta_{2D}\rangle(t)$, obtained at $t = 0$ ps, as a function of the intensity of the alignment pulse, I_{align}. The intensity dependence of $\langle\cos^2\theta_{2D}\rangle$ for the He-solvated molecules is very similar to that of the gas phase molecules (blue squares). There is a rather steep initial rise from 0.50 at $I_{align} = 0$ and then a more moderate rise from $I_{align} = 2.5 \times 10^{11}$ W/cm^2 ending at $\langle\cos^2\theta_{2D}\rangle = 0.92$ at the highest intensity used. We expect the $\langle\cos^2\theta_{2D}\rangle$ values of the isolated molecules to represent an accurate measurement of the true degree of alignment due to the essentially perfect axial recoil of the I^+ fragments. For the molecules in He droplets the deviation of axial recoil, as mentioned above, implies that the true degree of alignment is underestimated. Using a method based on analysis of the correlations between the IHe^+ fragment ions employing the angular covariance maps shown in Fig. 9.6 (b3), it is possible to correct the $\langle\cos^2\theta_{2D}\rangle$ measured for the effect of nonaxial recoil [69]. The result of this correction method is represented by the black filled circles in Fig. 9.8. Comparing this curve to the blue curve, it is clear that $\langle\cos^2\theta_{2D}\rangle$

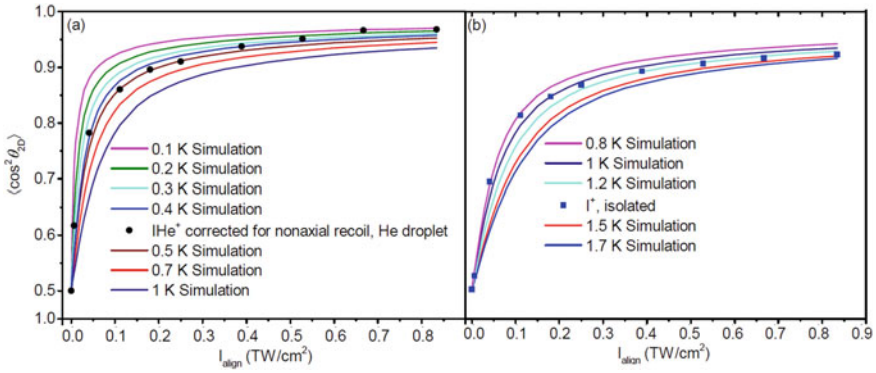

Fig. 9.22 $\langle \cos^2 \theta_{2D} \rangle$ for **a** I_2 molecules in He droplets and **b** isolated I_2 molecules calculated as a function of the alignment pulse intensity for different rotational temperatures. The black filled circles in (**a**) and the filled blue squares, representing the experimental results, are the same as the black filled circles and filled blue squares in Fig. 9.8. Adapted from Ref. [63] with the permission of American Institute of Physics (AIP) Publishing. Copyright 2017 by AIP

is significantly higher for I_2 in He droplets than for isolated I_2 molecules at all intensities. In particular, for the highest intensity, the corrected $\langle \cos^2 \theta_{2D} \rangle$ value is 0.96. For comparison, a sample of perfectly aligned molecules has $\langle \cos^2 \theta_{2D} \rangle = 1$.

To model and thus gain insight into alignment of the He-solvated molecules, we solved the rotational Schödinger equation (compare Eq. 9.2) for the I_2 molecules exposed to the experimental 160 ps alignment pulse. The molecules were treated as isolated molecules but with the effective B and D constants determined from the rotational coherence spectroscopy experiment discussed in Sect. 9.3.3. This treatment is motivated by the success of the model to accurately reproduce the $\langle \cos^2 \theta_{2D} \rangle(t)$ for the nonadiabatic aligment experiments on I_2, OCS and CS_2, as shown in Sect. 9.3.3. Also, the intensity of the laser pulse is sufficiently low and varies slowly enough that the He solvation shell is expected to follow adiabatically, as rationalized by angulon theory arguments [63].[12] The result of the calculations, expressed as $\langle \cos^2 \theta_{2D} \rangle$, at the peak of the pulse, as a function of the alignment intensity at different rotational temperatures of the I_2 molecules are shown in Fig. 9.22 (a).

At all intensities the experimental data points fall within the range confined by the calculated 0.2 K and 0.5 K curves, and on average lie close to the calculated 0.4 K curve. We believe that the agreement between the data points and the 0.4 K curve would be even better if the former could be corrected for the alignment-dependent ionization efficiency of the probe pulse: The probe pulse ionizes, and thus Coulomb explodes, the molecules aligned parallel (perpendicular) to its polarization axis most (least) efficiently. At intermediate degrees of alignment such as for the three data points between 0.1 and 0.3 TW/cm^2, $\langle \cos^2 \theta_{2D} \rangle$ will be underestimated because the best aligned molecules are least efficiently probed. A correction for this probe

[12] Details on angulon theory can be found in [167, 168].

pulse selectivity would increase $\langle\cos^2\theta_{2D}\rangle$ for the three points and bring them closer to the 0.4 K curve. The agreement between the simulated curve for 0.4 K and the experimental results lead us to conclude that in this limit of quasi-adiabatic alignment the He-solvated molecules behave as gas phase molecules at a temperature of 0.4 K. This conclusion is the same as we reached for nonadiabatic alignment, induced by fs or few-ps long alignment pulses.

The reason that the molecules in the He droplets obtain a higher degree of alignment than the molecules in the supersonic beam is that the rotational temperature is lower in the droplets. For the isolated molecules, we also calculated the degree of alignment at the peak of the pulse for different temperatures. The results, together with the experimental data, are displayed in Fig. 9.22 (b). It can be seen that the data points, apart from the points at the highest intensities, fall within the range confined by the calculated 0.8 K and 1.2 K curves. A temperature around 1 K is consistent with previous estimates of the rotational temperature for molecular beams produced by an Even-Lavie valve operated under similar conditions [93].

To complete the argumentation that the degree of alignment for a given molecule that is exposed to a specific laser field strength, E_0, is strongly dependent on temperature, we note that in 2001, Tamar Seideman showed that in the limit where $kT/B \gg 1$:

$$\langle\cos^2\theta\rangle = 1 - \sqrt{\pi kT/\Delta\alpha E_0^2}. \tag{9.11}$$

This expression shows that $\langle\cos^2\theta\rangle$ is determined by T and independent of B. For I_2 in He droplets, kT/B = 8.34 GHz/0.48 GHz = 17.4 and for the isolated I_2, kT/B = 20.9 GHz/1.12 GHz = 18.7, in both cases the ratio is much larger than 1. Using Eq. 9.11 we obtain $\langle\cos^2\theta\rangle = 0.94$ for the He-droplet case (T = 0.4 K) and 0.90 for the gas phase case (T = 1.0 K), with $\Delta\alpha = 7.0$ Å^3 and E_0 = 2.5e7 V/cm, corresponding to the highest intensity of 0.83 TW/cm^2. These values are in good agreement with the experimental $\langle\cos^2\theta_{2D}\rangle$ values of 0.96 and 0.92, noting that for a given distribution of aligned molecules, $\langle\cos^2\theta_{2D}\rangle$ is always slightly larger than $\langle\cos^2\theta\rangle$ [65, 145].

The effectiveness of He droplets as a medium in which strong molecular alignment can be created was also demonstrated for 1,4-diiodobenzene and 1,4-dibromobenzene, with direct comparison between He-solvated molecules and isolated molecules in a supersonic beam [63]. For the He-solvated molecules, $\langle\cos^2\theta_{2D}\rangle$ again exceeded 0.96 at the highest intensity applied, 0.83 TW/cm^2. In the following, though, we would like to present another example, which both illustrates the applicability of adiabatic alignment to a molecular dimer and also how the intensity-dependent degree of alignment again matches calculations with a rotational temperature of 0.4 K. The example is the carbon disulfide dimer. In the gas phase, the dimer has a cross-shaped structure with D_{2d} symmetry, and it is a prolate symmetric top, see Fig. 9.23. For now we assume the dimer has the same structure inside He droplets but in Sect. 9.3.7 we actually show that laser-induced Coulomb explosion imaging can be used to determine the structure of the CS_2 dimers in He droplets.

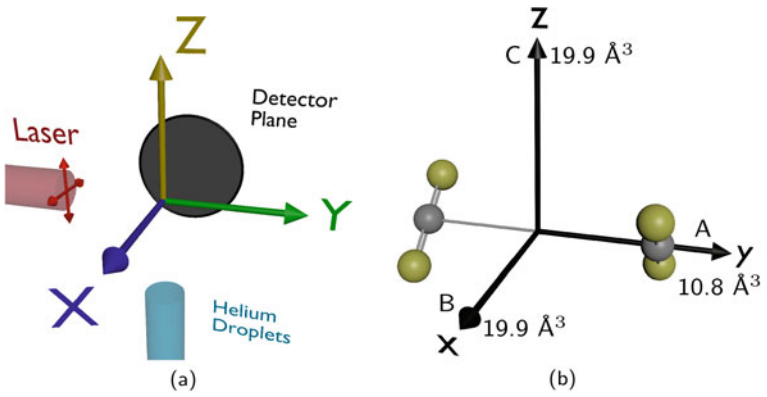

Fig. 9.23 **a** Sketch of the space-fixed (XYZ) coordinate system. **b** Sketch of the molecular (xyz) coordinate system and the CS_2 dimer in its ground state geometry. Polarizability elements of the dimer (in units of $Å^3$) are annotated onto each molecular axis. Adapted from [169] with permission from American Physical Society (APS). Copyright (2019) by APS

Experimentally, the He droplets were sent through a gas of CS_2 molecules with a pressure sufficiently high that there is a non-negligible probability that some of the droplets pick up two CS_2 molecules. Since the attraction between the two CS_2 molecules is much larger than between a CS_2 and a He atom, the two molecules are expected to approach each other and can then form a dimer with the binding energy being dissipated into the He solvent and subsequently removed from the droplet by evaporation of ∼162 He atoms—evaporation of one He atom removes $5\,cm^{-1}$ of energy [52] and the binding energy of $(CS_2)_2$ is $\sim 810\,cm^{-1}$ [170]. The doped droplets are irradiated by a 30 fs, 800 nm, $3 \times 10^{14}\,W/cm^2$, probe pulse. Hereby the CS_2 are singly ionized, leading to formation of CS_2^+ ions, which is the experimental observable considered in this section. Some of the molecules are also multiply ionized, which results in Coulomb explosion and production of S^+ fragment ions. The use of these ions for structure determination of the dimer is discussed in Sect. 9.3.7. To induce alignment, the 160 ps pulses are used with the probe pulse synchronized to its peak.

Figure 9.24 (a1) shows a 2D velocity image of CS_2^+ ions with the probe pulse only, polarized perpendicular to the detector plane. The image is dominated by an intense signal in the central portion corresponding to low kinetic energy of the CS_2^+ ions. We assign this signal to ionization of CS_2 monomers in droplets doped with a single molecule. There is also a significant amount of signal detected at larger radii—outside of the yellow ring—corresponding to larger kinetic energies. We assign these ions as originating from double ionization of $CS_2)_2$ from droplets containing a dimer, and subsequent breakup of the $(CS2)2^{2+}$ dication into two CS_2^+ fragment ions. This assignment was substantiated in the same way as we identified the Coulomb explosion for the I_2 molecule, either in gas phase or in He droplets, via calculation of the angular covariance map [43, 66], from ions in the radial range outside of the annotated yellow

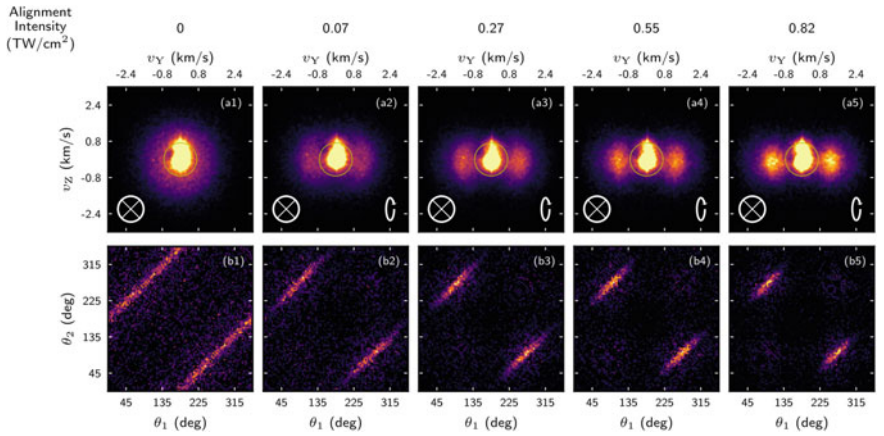

Fig. 9.24 **a**1–**a**5: 2D velocity images of CS_2^+ ion images at different intensities of the alignment pulse, annotated above each column. **b**1–**b**5): corresponding angular covariance maps determined from the ions outside the annotated yellow circles in row (**a**). The polarization state of the probe (alignment) laser is shown in the lower left (right) corner of each ion image. The data were recorded under doping conditions where CS_2 dimers could be formed. Adapted from [169] with permission from American Physical Society (APS). Copyright (2019) by APS

circle. The result is displayed in Fig. 9.24 (b1). Two distinct diagonal lines, centered at $\theta_2 = \theta_1 - 180°$ and $\theta_2 = \theta_1 + 180°$, stand out and show the correlation of a CS_2^+ ion with another CS_2^+ ion departing in the opposite direction [θ_i, i = 1,2 is the angle between an ion hit and the vertical center line].

The emission direction of the CS_2^+ fragment ions from Coulomb explosion of $CS_2)_2$ is determined by the spatial orientation of the C-C intermolecular axis of the parent dimer at the instant of ionization, similar to how the emission direction of I^+ or IHe^+ ions is a measure of the spatial orientation of the I-I axis of their parent I_2 molecule. Thus, the uniform extent of the covariance signal over 360° shows that the C-C axes are randomly oriented, which is to be expected in the absence of an alignment pulse. When the alignment pulse, circularly polarized in the XZ-plane (Fig. 9.23), is included the CS_2^+ ions images develop an asymmetry with the ions becoming confined along the Y-axis. As the intensity of the alignment pulse is increased, the confinement grows stronger as can be seen in the sequence of images on Fig. 9.24. These observations demonstrate that the CS_2 dimers are aligned with the C-C axis confined along the Y-axis. The effect of a circularly polarized alignment field is to confine the least polarizable molecular axis perpendicular to the polarization plane [22], which is the same as the propagation direction of the laser pulse (the Y-axis)—see Fig. 9.23 (a). Consequently, the CS_2 dimer inside the He droplets must have a structure where the least polarizable axis coincides with the C-C axis. This is the case for a cross-shape, as that of the gas phase dimer, but not for a T-shape, or a slipped-parallel shape [171]. Therefore, the ion images in Fig. 9.24 lead us to conclude that the dimer is cross-shaped and aligned with the C-C axis parallel to

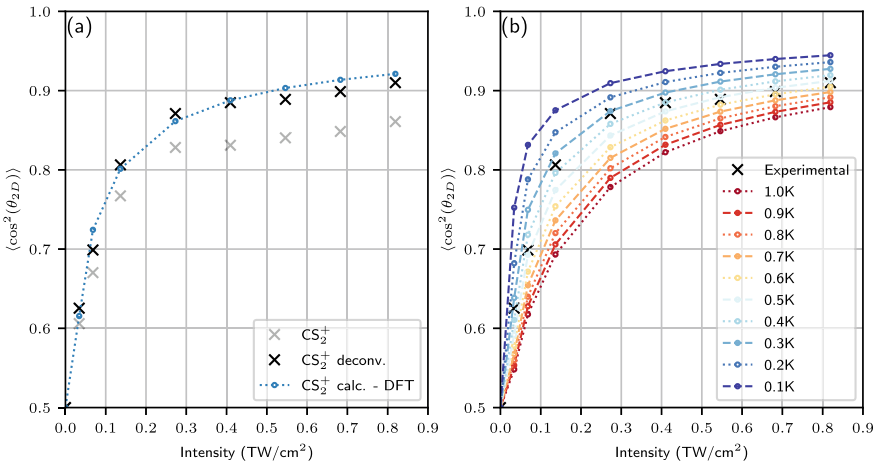

Fig. 9.25 Experimental (crosses) and simulated (circles and dashed line) degree of alignment of the CS_2 dimer as a function of alignment intensity. The alignment was induced adiabatically using a circularly polarized laser pulse. Panel **a** shows a comparison of the experimental degree of alignment with the simulated degree of alignment calculated at 0.4 K. Panel **b** shows a comparison of the experimental degree of alignment with the simulated degree of alignment calculated at a variety of different ensemble temperatures. Adapted from [169] with permission from American Physical Society (APS). Copyright (2019) by APS

the Y-axis. The dihedral angle between the two monomer axes cannot be determined from detecting CS_2^+ ions, but in Sect. 9.3.7 we show that this is possible from images of S^+ ions.

The quantification of the degree of alignment is done similar to that outlined in the previous sections. The grey crosses in Fig. 9.25 shows $\langle\cos^2\theta_{2D}\rangle$ as a function of I_{align} based on the five images in Fig. 9.24 and another four at other intensities. Here θ_{2D} is the angle between an ion hit and the propagation direction of the laser pulse, i.e. the Y axis, see Fig. 9.23. When the CS_2^+ ions travel out of the droplet, they are also subject to collisions with He atoms. To avoid underestimating the true degree of alignment, it is necessary to correct for this deviation from nonaxial recoil of the fragment ions, as discussed previously. The corrected data points are shown by the black crosses in Fig. 9.25 (a). They are well-matched by a calculation of $\langle\cos^2\theta_{2D}\rangle$ at the peak of the alignment pulse for the different intensities used in the experiment. The calculated values of $\langle\cos^2\theta_{2D}\rangle$ were obtained by solving the time-dependent rotational Schrödinger equation for the dimers exposed to the circularly polarized alignment pulse with the experimental parameters of its duration, intensity and spot size and for a 0.4K rotational temperature. Finally, the calculations were repeated for a series of different temperatures. As can be seen on Fig. 9.25 (b), the experimental data agrees well with the simulated data using an ensemble temperature between 0.3 and 0.5K. This agreement implies that the alignment of the CS_2 dimers in the He droplets is well-described by alignment of a 0.4K ensemble of gas phase CS_2 dimers.

This is in line with the expected temperature of the dimers inside the He droplets [52] and consistent with the findings for the I_2 molecules presented in Sect. 9.3.5.

9.3.6 *Long-Lasting Field-Free Alignment of Molecules*

In the previous section, we demonstrated that in the (quasi-) adiabatic limit of laser-induced alignment, molecules embedded in He nanodroplets can be very strongly aligned thanks to the 0.4 K rotational temperature of the molecules. We focused on 1D alignment, induced by a linearly polarized laser pulse but note that 3D alignment, induced by an elliptically polarized laser pulse, also benefits from the 0.4 K temperature and leads to higher degrees of alignment for He-solvated molecules compared to that of isolated molecules in a cold supersonic beam [172]. One disadvantage of adiabatic alignment is that the strongest alignment occurs at the peak of the pulse when the intensity is highest. For some applications of aligned molecules, this can be a serious obstacle, because the alignment field may perturb the molecules severely. An important example is molecules in electronically excited states, where the alignment field can cause further excitation, dissociation or ionization. Thus, the excited state reactions originally expected may not be observed because they are outmatched by processes induced by the alignment field [173]. In this section, we show how the alignment pulse can be turned off at its peak and how molecules in He droplets keep a very high degree of alignment for 5–20 ps without the presence of the alignment field. Comparison is made to molecules in the gas phase where, in contrast, the degree of alignment disappears rapidly after the pulse is turned off.

The experimental setup is similar to that used for the adiabatic alignment experiments except that the alignment laser beam is now sent through a longpass optical filter just before it is overlapped with the probe laser beam. This filter spectrally truncates the alignment pulses, which leads to a corresponding temporal truncation because the pulses are highly chirped [175]. The intensity profile of the alignment pulse, displayed by the grey shaded area in Fig. 9.26, shows a slow turn-on in ~100 ps followed by a rapid turn-off at the peak, where the intensity drops by more than two orders of magnitude over ~10 ps.

Figure 9.26 (a) shows the alignment dynamics of I_2 molecules, both isolated (black curve) and in He droplets (purple curve) exposed to the truncated pulse with linear polarization. All parameters of the alignment and the probe pulses are identical in the measurements on isolated and He-solvated molecules. During the rise of the pulse, the two curves follow the intensity profile, as already shown on Fig. 9.7. After the truncation, both curves drop, but the drop is much slower for the He-solvated molecules. The right panel of Fig. 9.26 (a) shows that $\langle\cos^2\theta_{2D}\rangle(t)$ retains a value between 0.86 and 0.80 from $t = 5$ ps to $t = 11$ ps, a period in which the alignment pulse intensity is reduced to less than 1 % of the value at the peak. When $\langle\cos^2\theta_{2D}\rangle(t)$ is corrected for the nonaxial recoil of the I^+ ions, the $\langle\cos^2\theta_{2D}\rangle(t)$ values are between 0.90 and 0.84. By contrast, in the same interval, $\langle\cos^2\theta_{2D}\rangle(t)$ for the isolated molecules drops from 0.69 to 0.52. These observations show that by rapidly truncating the alignment pulse,

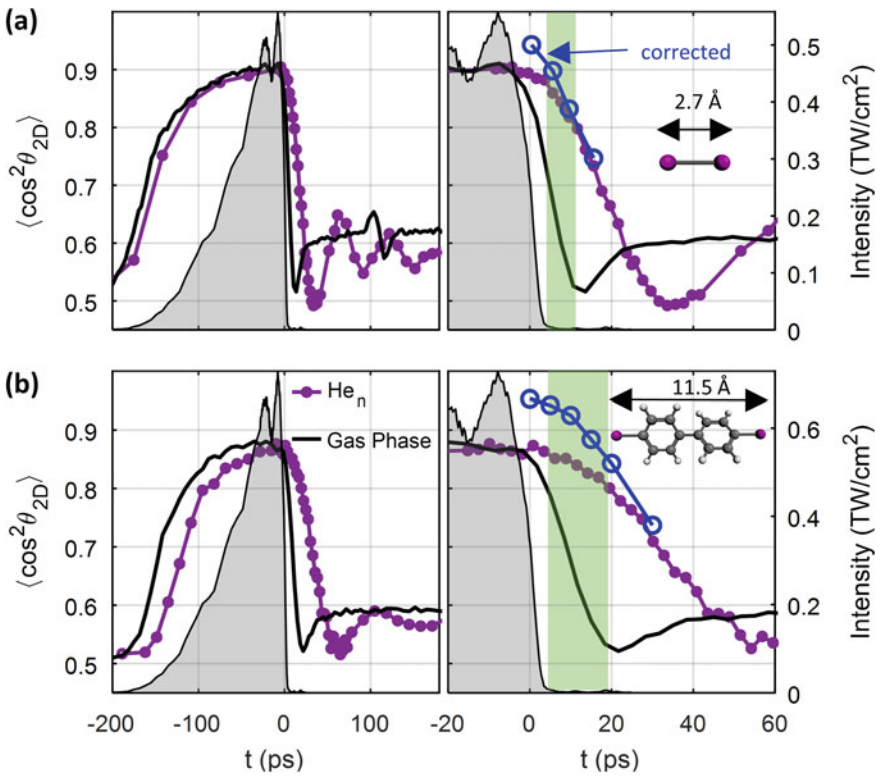

Fig. 9.26 $\langle \cos^2 \theta_{2D} \rangle (t)$ measured for I_2 (panels **a**) and 4,4'-diiodobiphenyl (panels **b**) molecules. Black curves: isolated molecules, purple curves: molecules in He droplets. The intensity profile of the truncated alignment pulse is shown by the grey shaded area and refers to the right vertical axis. The panels on the right show a zoom of the post-truncation region. The green shaded area in each panel marks the interval where the alignment field intensity is < 1 % of its peak and $\langle \cos^2 \theta_{2D} \rangle \geq 0.80$ for molecules solvated in He droplets. The structure of each molecule (shown as an inset), along with a scalebar representing the I–I distance. In droplets, the values for $\langle \cos^2 \theta_{2D} \rangle$ after correction for non-axial recoil at selected times are also shown as blue open circles. Reproduced from [174]

it is possible to create a 6 ps windows in which the I_2 molecules remain strongly aligned and where the alignment pulse intensity is reduced by more than a factor of 100, weak enough to be considered field-free for many applications.

We note that $\langle \cos^2 \theta_{2D} \rangle (t)$ does not return to 0.5 after truncation for either the isolated or the He-solvated molecules. In fact, the truncation creates a rotational wave packet in both cases. For gas phase molecules, this has been studied before [29, 36, 41, 176, 177]. In that case, distinct rotational revivals appear, qualitatively similar to the situation when a fs or ps pulse is used to create the rotational wave packet. Here we show the long-time dynamics for the He-solvated molecules to demonstrate that

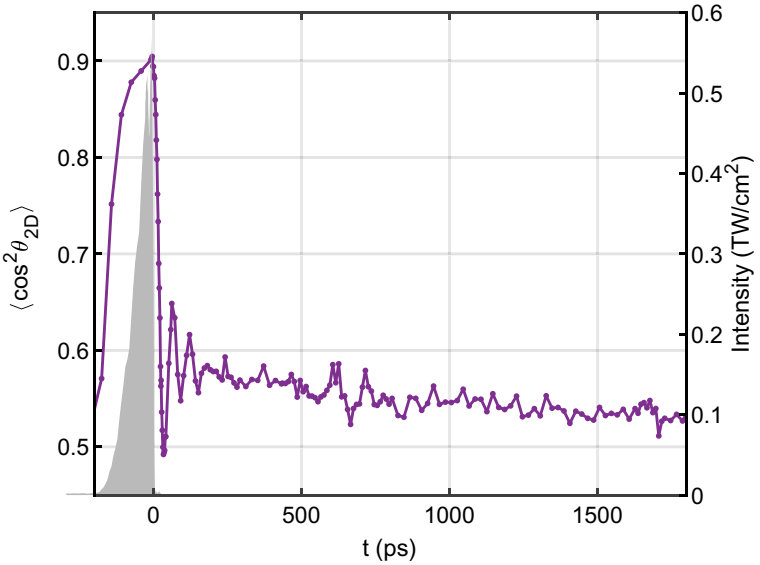

Fig. 9.27 $\langle \cos^2 \theta_{2D} \rangle(t)$ measured for I_2 molecules in He droplets. The alignment dynamics is induced by the truncated pulse with an intensity profile similar to that shown in Fig. 9.26

the truncated pulses can also create revivals for molecules in He droplets. Figure 9.27 shows $\langle \cos^2 \theta_{2D} \rangle(t)$ in the time interval −250 ps to 1800 ps. A distinct revival structure is observed at ∼ 650 ps after the truncation, a time position fully consistent with that of the half-revival observed for the 450 fs or 5 ps alignment pulses, see Fig. 9.16 and Fig. 9.18. The polarity of the revival is opposite to that of the revivals shown in those figures. This is because there is a different phase relationship between the eigenstates in the wave packet when it is created by truncation, i.e. from molecules that are already adiabatically aligned, compared to when it is created by a short laser pulse, acting on molecules that are initially randomly aligned. Finally, we point out that the average value of $\langle \cos^2 \theta_{2D} \rangle(t)$ (the permanent alignment level) decreases over the time measured, which indicates a decay of some of the rotational states in the wave packet.

Measurements were also conducted on a significantly larger molecule, namely 4,4'diiodobiphenyl (DIBP). Its most polarizable axis is along the I-I axis, so experimentally I^+ ions are ideal observables for characterizing 1D alignment, just as in the case of the I_2 molecules. The time-dependence of $\langle \cos^2 \theta_{2D} \rangle(t)$, obtained from I^+ (IHe^+) images for the isolated (He-solvated) molecules are shown in Fig. 9.26 (b). Despite the much larger moment of inertia for DIBP compared to I_2, $\langle \cos^2 \theta_{2D} \rangle(t)$ still rises concurrently with the intensity profile of the pulse. After the truncation, the $\langle \cos^2 \theta_{2D} \rangle(t)$ curves behave in a similar way to that observed for I_2 - a rapid decrease for the isolated molecules and lingering behavior for the He-solvated molecules. After correction for nonaxial recoil, we find that in the interval 5–20 ps, where the

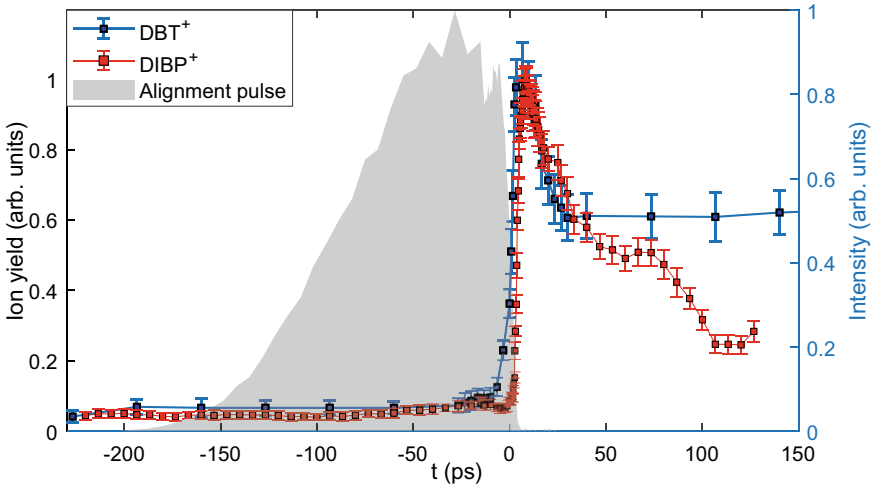

Fig. 9.28 Time-dependence of the parent ion yields when 1D aligned DBT or DIBP molecules are ionized with the probe pulse at time t. $I_{\text{probe}} = 2.4 \times 10^{14}$ W/cm^2

laser intensity is reduced to < 1 % of its maximum value, $\langle \cos^2 \theta_{2D} \rangle(t)$ remains between 0.94 and 0.84 for the He-solvated molecules while it drops from 0.78 to 0.53 for the isolated molecules. Thus, for DIBP in He droplets, there is a 15 ps long field-free alignment window.

To assess the field-free nature of the alignment created we measured the yield of intact parent cations following ionization of either 5,5"-dibromo-2,2':5',2"-terthiophene (DBT) or DIBP molecules with the probe pulse. DBT is an oligomer composed of three thiophene units. If the parent ions are created while the alignment pulse is on, we expect them to be fragmented by the remainder of the pulse, an effect generally occurring for most molecules, see e.g. [173, 178]. This destruction of parent ions precludes their use as experimental observables. Figure 9.28 shows the yield of DBT^+ and $DIBP^+$ ions created by ionization of 1D aligned molecules with the probe pulse sent at time t. When the probe pulse arrives during the alignment pulse the parent ion signal is almost zero but when it arrives after the pulse both the DBT^+ and $DIBP^+$ signal increases sharply and reaches a maximum at $t \sim 7 - 10$ ps, i.e. while the molecules are still strongly aligned, see Figs. 9.26 and 9.29. The sudden increase of the parent signal by almost a factor of 20 shows that the truncation reduces the alignment pulse intensity sufficiently to prevent destruction of the parent ions. Figure 9.28 demonstrates that our method enables ionization experiments on sharply aligned molecules, without the destruction of the fragile parent ions by the alignment field. Without this new ability, structural determination of dimers of large molecules by Coulomb explosion imaging, discussed in Sect. 9.3.7, would not be possible.

Finally, we discuss 3D alignment and how the truncated pulses also enable creation of a time window with 3D aligned molecules under field-free conditions. We

focus on the example of DBT. The molecular structure is sketched on the inset in Fig. 9.29 (c). Also, the most polarizable axis (MPA) and the second most polarizable axis (SMPA) are shown. To induce 3D alignment we use again the truncated laser pulse but now elliptically rather than linearly polarized. The idea, developed for gas phase molecules, is that the MPA of the molecule aligns along the major polarization axis of the laser pulse and the SMPA along the minor polarization axis [22, 80]. The last principal polarizability axis of the molecule is then automatically aligned perpendicular to the polarization plane. To characterize the 3D alignment two fragment ion species from the probe-pulse-induced Coulomb explosion are detected: 1) Br^+ ions as they are expected to recoil (approximately) along the direction of the MPA. 2) S^+ ions as they are expected to recoil (approximately) along the SMPA.

Figure 9.30 (a) shows a Br^+ ion image recorded for an alignment pulse linearly polarized along the Y-axis and with the probe pulse sent at $t = 0$, i.e. just before the truncation begins. The ions are sharply confined along the Y-axis showing pronounced 1D alignment of the DBT molecules as expected for the polarization state of the alignment pulse. This is a side view of the molecule. Figure 9.30 (c) shows a S^+ image. The alignment pulse is still linearly polarized but now the polarization is rotated to be parallel to the Z-axis. The circularly symmetric image shows that the rotation of the SMPA around the Z-axis is uniform. This is an end view of the molecule. Combining the information from the Br^+ and S^+ images, we conclude that the alignment pulse confine the MPA but leaves the rotation of the SMPA unrestricted.

When the polarization state of the alignment pulse is changed to elliptical with the major (minor) polarization axis parallel to the Z-axis (Y-axis), intensity ratio I_Z:I_Y = 3:1, the S^+ image Fig. 9.30 (d) acquires a pronounced angular confinement along the Y-axis. This shows that the SMPA is now aligned along the Y-axis. For the same elliptical polarization but now with the major axis parallel to the Y-axis, the Br^+ image remains sharply angularly confined along the Y-axis, Fig. 9.30 (b), i.e. the MPA is still strongly aligned. The simultaneous angular confinement of the Br^+ and the S^+ ions is the experimental evidence of 3D alignment similar to what has been used for a range of other asymmetric top molecules in the gas phase [22, 43, 80, 83, 172, 179].

To quantify the degree of alignment, we determine $\langle\cos^2\theta_{2D}\rangle$ from the Br^+ images and $\langle\cos^2\alpha\rangle$ from the S^+ images, α is defined in Fig. 9.29 (a). The time-dependence of $\langle\cos^2\theta_{2D}\rangle$ and $\langle\cos^2\alpha\rangle$ are shown in Fig. 9.29 (c). They both rise concurrently with the alignment pulse and reaches maximum values at its peak. These values, $\langle\cos^2\theta_{2D}\rangle \sim 0.80$ and $\langle\cos^2\alpha\rangle \sim 0.60$ are lower than those found for e.g. 3,5-dichloroiodobenzene molecules in He droplets [172]. We explain the lower values by the fact that the Br^+ and S^+ fragment ions do not recoil directly along the aligned axes as illustrated in Fig. 9.29 (a), (b). Therefore, $\langle\cos^2\theta_{2D}\rangle$ and $\langle\cos^2\alpha\rangle$ can only provide qualitative rather than quantitative measures for the degree of alignment [180]. The important finding is, however, the lingering of the alignment after pulse truncation. From $t = 5$ to 24 ps, where the laser intensity is $< 1\%$ of the peak value, $\langle\cos^2\theta_{2D}\rangle$ for the Br^+ ions drops only from 0.80 to 0.72, and $\langle\cos^2\alpha\rangle$ remains > 0.58 for the S^+ ions. This demonstrates a 19 ps-long interval, marked by the green area, where the molecules are 3D aligned under field-free conditions.

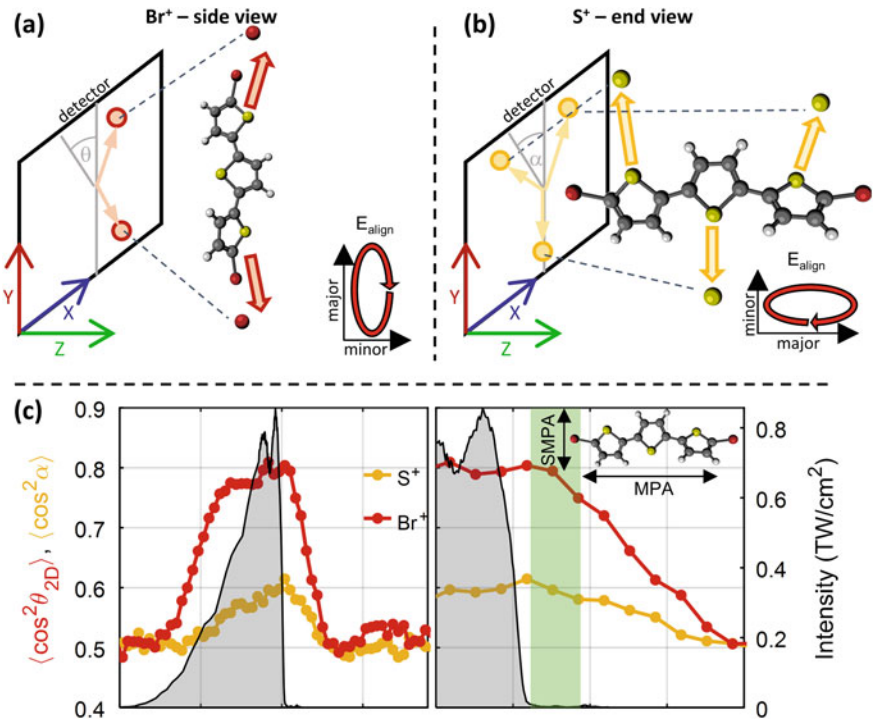

Fig. 9.29 **a**-**b**: Illustration of how 3D alignment of DBT is characterized. **a**: Side view where the MPA of DBT is confined to the major polarization axis of the alignment pulse, directed along the Y-axis. **b**: End view of DBT, with the MPA confined to the major polarization axis directed on the Z-axis. In the side view, alignment is characterized by $\langle \cos^2 \theta_{2D} \rangle$ where θ_{2D} is the angle between the emission direction of a Br^+ ion and the Y-axis, while in the end view it is characterized by $\langle \cos^2 \alpha \rangle$ where α is the angle between the emission direction of a S^+ ion and the Y-axis. **c**: The time dependence of $\langle \cos^2 \theta_{2D} \rangle$ and $\langle \cos^2 \alpha \rangle$ for DBT molecules induced by an elliptically polarized alignment pulse with an intensity ratio of 3:1. The panels on the right show a zoom of the post-truncation region and the green shaded areas mark the interval where the alignment field intensity is <1% of its peak value and $\langle \cos^2 \theta_{2D} \rangle$ has dropped by less than 10%. The MPA and SMPA are overlaid on the molecular structure. Adapted from [174]

9.3.7 Structure Determination of Dimers in He Nanodroplets

In this section, we discuss how the combination of laser-induced alignment and Coulomb explosion imaging makes it possible to determine structure of molecular complexes formed inside He nanodroplets. So far, we have introduced Coulomb explosion of molecules and of molecular dimers, triggered by multiple ionization with an intense fs probe pulse, as a technique to determine the spatial orientation of such systems. Coulomb explosion can also serve another useful purpose in determination of molecular structure. This approach is termed Coulomb explosion imaging (CEI)

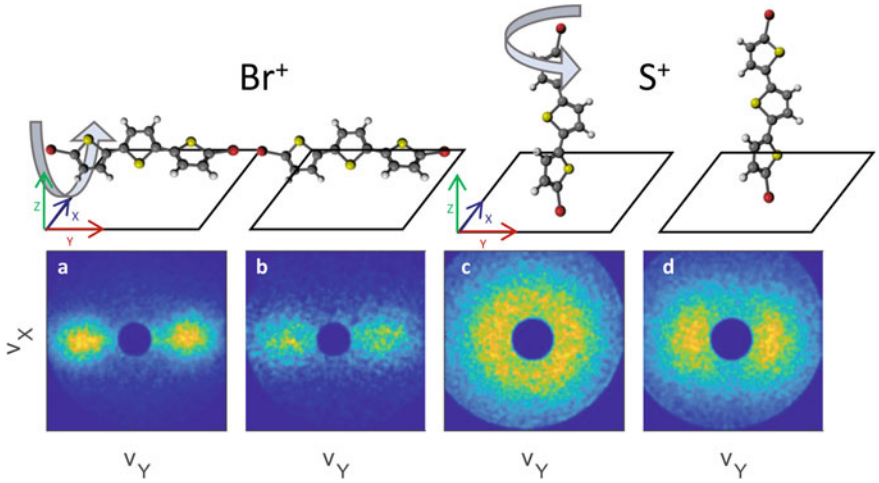

Fig. 9.30 Two-dimensional velocity images of Br^+ ions (**a**-**b**) and S^+ ions (**c**-**d**) produced from Coulomb explosion of DBT molecules in He droplets at the peak of either a linearly polarized (**a**,**c**) or an elliptically polarized (**b**,**d**) alignment pulse with a peak intensity of 9×10^{11} W/cm^2. The molecular alignment and rotational freedom are depicted above each ion image. Reproduced from the supplementary material of [174]

and relies on the fact that the molecular structure is encoded in the kinetic energy and emission direction of the recoiling fragment ions.

The CEI technique was originally introduced in experiments where a MeV beam of small molecular ions was sent through a few-hundred Å thin metal foil [181]. However most later studies, including many current activities, employ intense fs laser pulses to trigger the Coulomb explosion event [57]. Typically, the pulses are in the near IR region, as in the work described here, but VUV [182] and x-ray pulses [183, 184] are also used. Coulomb explosion imaging has been applied in a variety of different studies, for example determination of the absolute configuration of chiral molecules [121, 185–187], time-resolved imaging of intramolecular processes such as torsion [42, 44], dissociation [188, 189], roaming [190] and proton migration [191], identification of structural isomers [192, 193], and imaging of interatomic or intermolecular wavefunctions of diatomic molecules [194–196] or of weakly bonded dimers [170, 197, 198]. Key to obtaining structural information is the identification of correlations in the angular distributions of the fragment ions, in practice implemented by coincidence or covariance analysis. More recently, it was shown that aligning the molecules in well-defined spatial orientations with respect to the ion imaging detector prior to the Coulomb explosion event increases the structural information available from the recorded fragment ion momenta [43]. Such molecular frame measurement is an example of one of the main advantages offered by aligned molecules as mentioned in Sect. 9.1.

Here we give two examples of structure determination of molecular dimers inside He droplets. The first concerns the CS_2 dimer. In Sect. 9.3.5 we already discussed

how this dimer can be aligned by a laser pulse and how velocity images of CS_2^+ ions, resulting from double ionization of aligned dimers and subsequent Coulomb explosion into two CS_2^+ fragment ions, make it possible to infer that the dimer structure is cross-shaped. The dihedral angle, i.e. the angle between the interatomic axes of the CS_2 monomers could, however, not be determined. We now discuss how this angle can be determined from images of S^+ ions. The pump and the probe laser pulses were the same as those used for the measurement described in Sect. 9.3.5.

Figure 9.31 (a1) shows a velocity map image of S^+ ions under doping cell conditions where each droplet picks up at most one molecule. The angular distribution of the S^+ ions is localized along the vertical axis, which is parallel to the polarization direction of the alignment pulse. In analogy with the adiabatic alignment experiments on I_2, Sect. 9.3.5, we conclude that the CS_2 molecules are 1D aligned. The identification of the S^+ ions as arising from Coulomb explosion of the CS_2 molecules is obtained from the angular covariance map of the S^+ ions, Fig. 9.31 (a2), determined from ions outside the yellow circle. Strong correlations of ions with a relative emission of 180° are observed similar to the observations for I_2. Such a correlation can originate from double ionization of CS_2 and fragmentation into (S^+, C and S^+) or triple ionization of CS_2 and fragmentation into (S^+, C^+ and S^+).

The more interesting observations appear when the doping pressure is increased such that a significant number of the droplets become doped with CS_2 dimers. The S^+ image, shown in Fig. 9.31 (b1) is still confined along the vertical axis. It is wider than the distribution in Fig. 9.31 (a1) but it is not easy to identify a clear signature of the contribution from the dimers in this image alone. However, the contribution from the dimers clearly stands out in the angular covariance map of the image displayed in Fig. 9.31 (b2). In addition to the prominent monomer signals at (0°, 180°) and (180°, 0°) strong correlations are present centered approximately at (−45°, 45°), (−45°, 135°), (−45°, 225°), (45°, 135°), (45°, 225°), (135°, 225°) and, since the covariance map is an autovariance map, at six equivalent positions obtained by mirroring in the central diagonal. Analysis of these extra islands in the covariance map makes it possible to conclude that the dihedral angle is 90°. The details are given in [171]. The method described here for CS_2 was also applied to determine the structure of the OCS dimer [199]. The structure was found to be a slipped-parallel shape similar to the structure found for gas phase dimers [200].

The second example concerns a more complex system namely the dimer of tetracene (Tc), a polycyclic aromatic hydrocarbon composed of four benzene rings fused together in a linear geometry. As a starting point velocity map images of parent ions, Tc^+, were recorded. The angular covariance map of the Tc^+ ions created with the alignment pulse polarized along the X-axis (perpendicular to the detector, see Fig. 9.5), is depicted in Fig. 9.32(a_e). The prominent diagonal stripes show correlation between ions departing with a relative angle of 180°. As in the previous case of $(CS_2)_2$, we conclude that Tc dimers are formed and that they can be identified by double ionization and subsequent Coulomb explosion into a pair of Tc^+ ions. Next, we recorded Tc^+ images and, in particular, determined the corresponding angular covariance maps for different alignment geometries. In the case of the CS_2 dimer this was done by synchronizing the probe pulse to the peak of the 160 ps long alignment

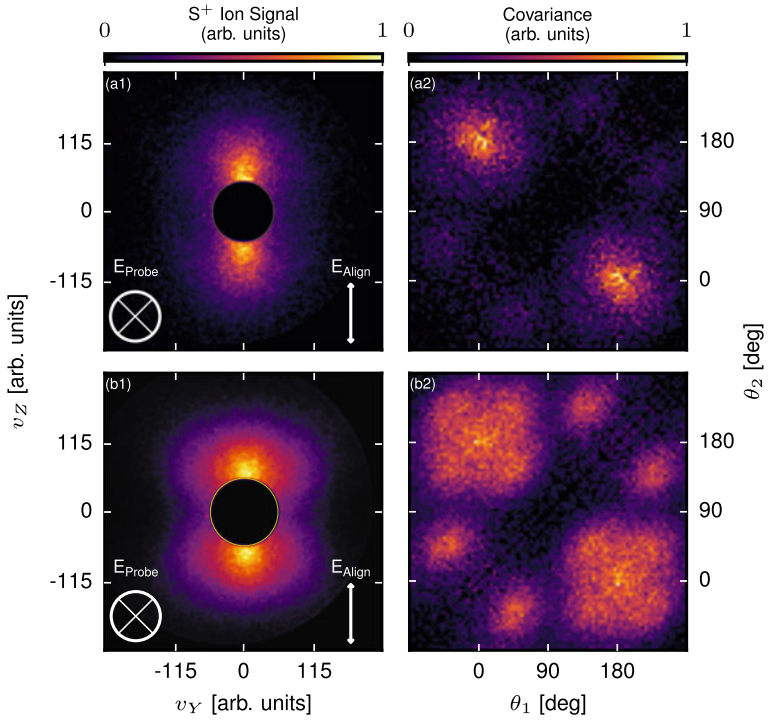

Fig. 9.31 (a1)-(b1) S^+ ion images and (a2)-(b2) corresponding angular covariance maps created from ions outside the yellow circles. The polarization state of the probe (alignment) pulse is given in the lower left (right) corner of each ion image. Image (a1) [(b1)] was recorded under the monomer-[dimer]-doping-condition. Here the central region is removed due to background contaminants occurring at m/z = 32 Da. Reproduced from [171] with permission from American Physical Society (APS). Copyright (2018) by APS

pulse to benefit from the highest degree of alignment. This approach does not work for the Tc case because the Tc^+ ion is destroyed by the alignment pulse similar to what happened to the DIBP molecules illustrated in Fig. 9.28. Now we can, however, make use of the ability to create field-free alignment by rapidly turning off the alignment field. Therefore, the measurements on aligned Tc dimers are recorded using the truncated alignment pulse and the probe pulse sent 10 ps after the truncation. In contrast, the CS_2^+ ions were not significantly fragmented by the alignment pulse, and so in that case, no truncation was needed.

Column two from the left in Fig. 9.32 shows the angular covariance maps for Tc^+ recorded for different alignment geometries. The covariance maps change when the polarization of the alignment pulse is changed from linear to elliptical. The approach to deducing the dimer structure is to compare the experimental covariance maps to covariance maps simulated for the most plausible structures. This was done employing seven different dimer conformations. The angular covariance maps, sub-

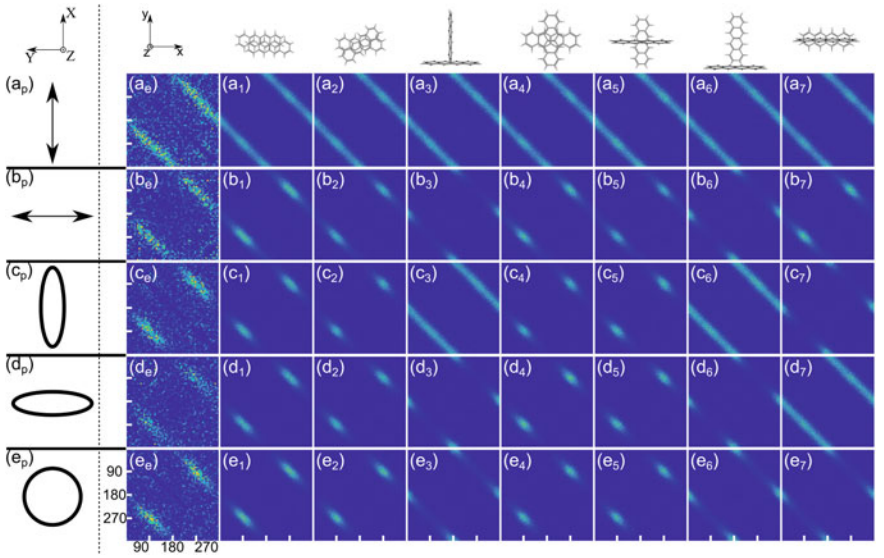

Fig. 9.32 Angular covariance maps obtained for the Tc dimer. The left column shows the polarization state of the alignment pulse for each row. (the laboratory axes are illustrated at the top). Index e (second column from the left) refers to the experimental results, while indices 1–7 refer to simulated results for different plausible conformations of the tetracene dimer depicted on top of the corresponding column. Each panel axis ranges linearly from 0 to 360°. Reproduced from [201] licensed under a Creative Commons Attribution (CC BY) license

indexed 1–7, are displayed in Fig. 9.32. Details of the numerical simulations are given in [201]. The comparison shows that conformations 1, 2, 4, and 5, produce covariance maps consistent with the experimental data.

To narrow down the possible structures for the dimers we would ideally like to analyze covariance maps for another fragment ion species, just as the S^+ ions were analyzed in addition to the CS_2^+ ions for the carbon disulfide dimer case. For tetracene, fragmentation will produce H^+ or hydrocarbon ions and neither of these will be particularly structure-informative because they can originate from different parts of the Tc molecule. Instead, we performed an alternative type of measurement by recording the alignment-dependent ionization yield of the Tc dimer. In practice, the Tc^+ ion yield was measured for the 1D aligned dimers with the probe pulse polarized either parallel or perpendicular to the alignment polarization. For $I_{\text{probe}} = 3 \times 10^{12}$ W/cm^2, the Tc^+ yield in the parallel geometry was 5.5 times higher than in the perpendicular geometry. Such a large difference in the ionization yield implies that the dimer structure must be highly anisotropic. In particular, the dimer must possesses a 'long' axis leading to the highest ionization rate when the probe pulse is polarized along it. Such an anisotropic structure is compatible with conformations 1 and 2 but not with conformations 4 and 5. Thus, we conclude that the possible conformations of the Tc dimer is a slipped-parallel or parallel-slightly rotated structure.

Recently, we have applied the CEI method to the bromobenzene homodimer, $(BrPh)_2$, and the bromobenzene-iodine, $BrPh–I_2$, heterodimer [202]. As for the CS_2 dimer, both $(BrPh)_2$ and $BrPh–I_2$ produce 'tracer-ions', here Br^+ and I^+, in addition to the parent ions. Analysis of the angular covariance maps for both the parent ions and the atomic fragment ions, lead us to conclude that for $BrPh–I_2$, the I_2 molecular axis is approximately perpendicular to the C–Br axis of bromobenzene, whereas $(BrPh)_2$, has a stacked planar structure, with the two bromine atoms pointing in opposite directions.

9.4 Conclusion

The work presented in this article has shown that laser-induced alignment techniques, originally developed for isolated molecules in the gas phase, can be transferred to molecules embedded in He nanodroplets. In the (quasi) adiabatic limit, here realized with 160 ps long alignment pulses, the alignment dynamics observed for different molecular species was essentially the same as that of isolated molecules, i.e. the degree of alignment followed the intensity profile of the alignment laser pulse. Furthermore, the intensity dependence of the strongest alignment, reached at the peak of the pulse, agreed well with a gas phase model calculation for a rotational temperature of 0.4 K. These observations indicate that the mechanism of adiabatic laser-induced alignment of molecules in He droplets is the same as that of isolated molecules with a 0.4 K temperature. This temperature, which is lower than the 1–2 K temperature typically reached in cold supersonic beams of isolated molecules, is advantageous for creating very high degrees of alignment, with $\langle \cos^2 \theta_{2D} \rangle$ values in excess of 0.95. By truncating the alignment pulse in time just after its peak, we demonstrated that a 5–20 ps long time window can be created, where the alignment pulse intensity is reduced by several orders of magnitude and yet where the degree of alignment remains high. The reduction of the intensity was sufficient to eliminate the fragmentation of parent ions of large molecules that the remainder of the alignment pulse usually causes. This opens new opportunities for exploring e.g. how the ionization rate of large molecules induced by strong laser pulses or by VUV laser pulses, depends on the molecular alignment with respect to the polarization state of the ionizing laser pulse. In the field-free period, the intensity of the alignment pulse is also expected to be low enough that molecules in electronically excited states will remain intact. This opens unexplored possibilities for femtosecond time-resolved imaging of molecules undergoing fundamental photo-induced intramolecular processes in electronically excited states using Coulomb explosion, or diffraction by ultrashort x-ray [203, 204] or electron pulses [205–208].

One application, discussed here, of adiabatically aligned molecules is structure determination of molecular dimers through Coulomb explosion imaging. We showed that by aligning molecular dimers, either 1-dimensionally or 3-dimensionally, prior to their Coulomb explosion by an intense laser fs laser pulse, made it possible to determine the dimer configuration from the angular covariance maps of the fragment

ions. For dimers of small molecules like CS_2 or OCS, the structural resolution of the CEI method cannot compete with that available from IR spectroscopy. For larger systems like the tetracene dimer, the IR spectra may, however, be too congested to extract any structural information. The biggest promise of the CEI technique lies, however, in its ability to capture the structure of dimers as they change on the natural atomic time scale. Experimentally, this can be realized by using a fs pump laser pulse to initiate some event of interest like exciplex formation [209, 210] from a weakly-bonded dimer and then following the structural evolution by Coulomb explosion with an intense fs probe pulse sent at a sequence of different times. More generally, it should be possible to trigger bimolecular reactions [211, 212], by initiating the dynamics from prereactive complexes with the fs pump pulse.

It was also shown that molecules in He droplets can be aligned by laser pulses that are much shorter than the intrinsic rotational period of the molecules. In this nonadiabatic limit, two regimes were identified. When the laser pulses are weak, meaning that the rotational energy acquired by the molecules remain below a few cm^{-1}, the alignment dynamics can be accurately described by a gas phase model where the molecule is characterized by the effective rotational and centrifugal distortion constants, and the inhomogenoeus broadening of these two parameters is taken into account. Thus, the molecules essentially rotate (quasi)-freely although the time-dependent degree of alignment in practice appear different from that of gas phase molecules because the centrifugal distortion constant, 3–4 orders of magnitude larger than for isolated molecules, causes a strong dispersion of $\langle \cos^2 \theta_{2D} \rangle$, and the inhomogeneous broadening a gradual decay of the amplitude of the oscillations of $\langle \cos^2 \theta_{2D} \rangle$. We believe the quasi-free rotation is a result of the superfluidity of the He droplets.

When the duration of the alignment pulse was kept short (hundreds of fs or a few ps) but its intensity increased significantly, we observed that the rotational dynamics during the first few ps were essentially as fast as for isolated molecules under the same laser conditions. This phenomenon was interpreted as the molecule and its He solvation shell being set into so fast rotation by the strong alignment pulse that the weakly bonded He atoms in the shell were shed off due to the centrifugal force. The interpretation was backed by classical calculations.

Looking forward, there are exciting opportunities to be explored with nonadiabatic alignment of molecules in He droplets. First, the quasi-free rotation observed for low intensities of the alignment pulse is, we believe, a result of superfluidity of the He droplets: the induced rotational energy remains so low that coupling between rotation and the He excitations (rotons, phonons) is very weak. When the intensity of the alignment pulse is increased higher-lying rotational states will be excited and the coupling to the He excitations will increase strongly. It will be interesting to investigate both the structure and dynamics (lifetime) of rotational states in this unexplored regime which is inaccessible to MW and IR spectroscopy. Another opportunity is to use the short, very intense alignment pulse to transiently decouple a molecule from its solvation shell. This will create a situation where the molecule-He system is extremely far away from equilibrium. For instance, we estimate that a CS_2 molecule can acquire more than $500\,cm^{-1}$ of rotational energy by the interaction

with an alignment pulse. In comparison the rotational energy at 0.4 K is $\sim 0.3\,\mathrm{cm}^{-1}$. We propose to measure how long it takes for the equilibrium to be restored. In practise this could be done by measuring the rotational dynamics induced by a weak alignment pulse sent after the intense distortion pulse and observing how much the weak pulse must be delayed with respect to the distortion pulse that the alignment trace recorded becomes identical to a reference trace obtained without any distortion pulse. Finally, the studies discussed in this article concerned molecules embedded inside He droplets. Dimers of alkali atoms are, however, residing on the surface of He droplets [213–215]. It will be interesting to apply the nonadiabatic alignment schemes to investigate the rotation of alkali dimers, a topic that is so far unexplored. Such studies, which are now ongoing in our group, may also provide information about their binding to the surface.

Acknowledgements The work described here was supported by The Independent Research Fund Denmark (grant no. 10-083041 and no. 8021-00232B), The Lundbeck Foundation (grant no. R45-A4280), The Carlsberg Foundation (grant no. 2009-01-0378), The European Research Council-AdG (Project No. 320459, DropletControl), The European Union Horizon 2020 research and innovation program under the Marie Sklodowska-Curie Grant Agreement No. 641789 MEDEA and No. 674960 ASPIRE, and The Villum Foundation: Villum Experiment (grant no. 23177) and Villum Investigator (grant no. 25886.)

References

1. P.R. Brooks, Science **193**, 11–16 (1976)
2. M. Lein, J. Phys. B: At. Mol. Opt. Phys. **40**, R135–R173 (2007)
3. L. Holmegaard, J.L. Hansen, L. Kalhoj, S. Louise Kragh, H. Stapelfeldt, F. Filsinger, J. Küpper, G. Meijer, D. Dimitrovski, M. Abu-samha, C.P.J. Martiny, L. Bojer Madsen, Nat. Phys. **6**, 428–432 (2010)
4. J. Arlt, D.P. Singh, J.O.F. Thompson, A.S. Chatterley, P. Hockett, H. Stapelfeldt, K.L. Reid, Mol. Phys. **119**, e1836411 (2021)
5. D.H. Parker, R.B. Bernstein, Annu. Rev. Phys. Chem. **40**, 561 (1989)
6. H.J. Loesch, A. Remscheid, J. Chem. Phys. **93**, 4779–4790 (1990)
7. B. Friedrich, D.R. Herschbach, Nature **353**, 412–414 (1991)
8. J.M. Rost, J.C. Griffin, B. Friedrich, D.R. Herschbach, Phys. Rev. Lett. **68**, 1299–1302 (1992)
9. P.A. Block, E.J. Bohac, R.E. Miller, Phys. Rev. Lett. **68**, 1303–1306 (1992)
10. B. Friedrich, D.P. Pullman, D.R. Herschbach, J. Phys. Chem. **95**, 8118–8129 (1991)
11. V. Aquilanti, D. Ascenzi, D. Cappelletti, F. Pirani, Nature **371**, 399–402 (1994)
12. V. Aquilanti, M. Bartolomei, F. Pirani, D. Cappelletti, F. Vecchiocattivi, Y. Shimizu, T. Kasai, Phys. Chem. Chem. Phys. **7**, 291 (2005)
13. R.E. Drullinger, R.N. Zare, J. Chem. Phys. **51**, 5532–5542 (1969)
14. M.J. Weida, C.S. Parmenter, J. Chem. Phys. **107**, 7138–7147 (1997)
15. B. Friedrich, D. Herschbach, Phys. Rev. Lett. **74**, 4623–4626 (1995)
16. T. Seideman, J. Chem. Phys. **103**, 7887–7896 (1995)
17. W. Kim, P.M. Felker, J. Chem. Phys. **104**, 1147–1150 (1996)
18. T. Seideman, Phys. Rev. Lett. **83**, 4971 (1999)
19. H. Sakai, C.P. Safvan, J.J. Larsen, K.M. Hilligsøe, K. Hald, H. Stapelfeldt, J. Chem. Phys. **110**, 10235–10238 (1999)
20. N.E. Henriksen, Chem. Phys. Lett. **312**, 196–202 (1999)

21. J. Ortigoso, M. Rodríguez, M. Gupta, B. Friedrich, J. Chem. Phys. **110**, 3870–3875 (1999)
22. J.J. Larsen, K. Hald, N. Bjerre, H. Stapelfeldt, T. Seideman, Phys. Rev. Lett. **85**, 2470 (2000)
23. F. Rosca-Pruna, M.J.J. Vrakking, Phys. Rev. Lett. **87**, 153902 (2001)
24. I.S. Averbukh, R. Arvieu, Phys. Rev. Lett. **87**, 163601 (2001)
25. M. Machholm, N.E. Henriksen, Phys. Rev. Lett. **87**, 193001 (2001)
26. V. Renard, M. Renard, S. Guérin, Y.T. Pashayan, B. Lavorel, O. Faucher, H.R. Jauslin, Phys. Rev. Lett. **90**, 153601 (2003)
27. E. Péronne, M.D. Poulsen, C.Z. Bisgaard, H. Stapelfeldt, T. Seideman, Phys. Rev. Lett. **91**, 043003 (2003)
28. M. Leibscher, I.S. Averbukh, H. Rabitz, Phys. Rev. Lett. **90**, 213001 (2003)
29. J.G. Underwood, M. Spanner, M.Y. Ivanov, J. Mottershead, B.J. Sussman, A. Stolow, Phys. Rev. Lett. **90**, 223001 (2003)
30. P.W. Dooley, I.V. Litvinyuk, K.F. Lee, D.M. Rayner, M. Spanner, D.M. Villeneuve, P.B. Corkum, Phys. Rev. A **68**, 023406 (2003)
31. H. Stapelfeldt, T. Seideman, Rev. Mod. Phys. **75**, 543 (2003)
32. T. Seideman, E. Hamilton, Adv. At. Mol. Opt. Phys **52**, 289–329 (2005)
33. Y. Ohshima, H. Hasegawa, Int. Rev. Phys. Chem. **29**, 619–663 (2010)
34. S. Fleischer, Y. Khodorkovsky, E. Gershnabel, Y. Prior, I.S. Averbukh, Isr. J. Chem. **52**, 414–437 (2012)
35. C.P. Koch, M. Lemeshko, D. Sugny, Rev. Mod. Phys. **91**, 035005 (2019)
36. T. Seideman, J. Chem. Phys. **115**, 5965–5973 (2001)
37. B. Friedrich, D. Herschbach, J. Phys. Chem. **99**, 15686–15693 (1995)
38. J.H. Nielsen, P. Simesen, C.Z. Bisgaard, H. Stapelfeldt, F. Filsinger, B. Friedrich, G. Meijer, J. Küpper, Phys. Chem. Chem. Phys. **13**, 18971–18975 (2011)
39. V. Renard, M. Renard, A. Rouzée, S. Guérin, H.R. Jauslin, B. Lavorel, O. Faucher, Phys. Rev. A **70**, 033420 (2004)
40. M. Leibscher, I.S. Averbukh, H. Rabitz, Phys. Rev. A **69**, 013402 (2004)
41. B.J. Sussman, J.G. Underwood, R. Lausten, M.Y. Ivanov, A. Stolow, Phys. Rev. A **73**, 053403 (2006)
42. C.B. Madsen, L.B. Madsen, S.S. Viftrup, M.P. Johansson, T.B. Poulsen, L. Holmegaard, V. Kumarappan, K.A. Jørgensen, H. Stapelfeldt, Phys. Rev. Lett. **102**, 073007–4 (2009)
43. J.L. Hansen, J.H. Nielsen, C.B. Madsen, A.T. Lindhardt, M.P. Johansson, T. Skrydstrup, L.B. Madsen, H. Stapelfeldt, J. Chem. Phys. **136**, 204310–204310–10 (2012)
44. L. Christensen, J.H. Nielsen, C.B. Brandt, C.B. Madsen, L.B. Madsen, C.S. Slater, A. Lauer, M. Brouard, M.P. Johansson, B. Shepperson, H. Stapelfeldt, Phys. Rev. Lett. **113**, 073005 (2014)
45. C.Z. Bisgaard, O.J. Clarkin, G. Wu, A.M.D. Lee, O. Gessner, C.C. Hayden, A. Stolow, Science **323**, 1464–1468 (2009)
46. J. Itatani, J. Levesque, D. Zeidler, H. Niikura, H. Pépin, J.C. Kieffer, P.B. Corkum, D.M. Villeneuve, Nature **432**, 867–871 (2004)
47. T. Kanai, S. Minemoto, H. Sakai, Nature **435**, 470–474 (2005)
48. J.P. Marangos, S. Baker, N. Kajumba, J.S. Robinson, J.W.G. Tisch, R. Torres, Phys. Chem. Chem. Phys. **10**, 35–48 (2008)
49. B.K. McFarland, J.P. Farrell, P.H. Bucksbaum, M. Gühr, Science **322**, 1232–1235 (2008)
50. P.M. Kraus, B. Mignolet, D. Baykusheva, A. Rupenyan, L. Horný, E.F. Penka, G. Grassi, O.I. Tolstikhin, J. Schneider, F. Jensen, L.B. Madsen, A.D. Bandrauk, F. Remacle, H.J. Wörner, Science **350**, 790–795 (2015)
51. B. Shepperson, A.S. Chatterley, L. Christiansen, A.A. Søndergaard, H. Stapelfeldt, Phys. Rev. A **97**, 013427 (2018)
52. J.P. Toennies, A.F. Vilesov, Angew. Chem. Int. Ed. **43**, 2622–2648 (2004)
53. M.Y. Choi, G.E. Douberly, T.M. Falconer, W.K. Lewis, C.M. Lindsay, J.M. Merritt, P.L. Stiles, R.E. Miller, Int. Rev. Phys. Chem. **25**, 15 (2006)
54. S. Yang, A.M. Ellis, Chem. Soc. Rev. **42**, 472–484 (2012)

55. J.L. Hansen, Imaging molecular frame dynamics using spatially oriented molecules. Ph.D. thesis, Aarhus University, Aarhus (2012)
56. S. Trippel, T.G. Mullins, N.L. Müller, J.S. Kienitz, K. Dlugolecki, J. Küpper, Mol. Phys. **111**, 1738–1743 (2013)
57. T. Yatsuhashi, N. Nakashima, J. Photochem. Photobiol. C: Photochem. Rev. **34**, 52–84 (2018)
58. X. Ren, V. Makhija, V. Kumarappan, Phys. Rev. A **85**, 033405 (2012)
59. J. Mikosch, C.Z. Bisgaard, A.E. Boguslavskiy, I. Wilkinson, A. Stolow, The J. Chem. Phys. **139**, 024304 (2013)
60. D.W. Chandler, P.L. Houston, The J. Chem. Phys. **87**, 1445–1447 (1987)
61. A.T.J.B. Eppink, D.H. Parker, Rev. Sci. Instrum. **68**, 3477–3484 (1997)
62. U. Even, J. Jortner, D. Noy, N. Lavie, C. Cossart-Magos, J. Chem. Phys. **112**, 8068–8071 (2000)
63. B. Shepperson, A.S. Chatterley, A.A. Søndergaard, L. Christiansen, M. Lemeshko, H. Stapelfeldt, The J. Chem. Phys. **147**, 013946 (2017)
64. J.H. Posthumus, A.J. Giles, M.R. Thompson, K. Codling, J. Phys. B: At. Mol. Opt. Phys. **29**, 5811–5829 (1996)
65. A.A. Søndergaard, B. Shepperson, H. Stapelfeldt, J. Chem. Phys. **147**, 013905 (2017)
66. C.S. Slater, S. Blake, M. Brouard, A. Lauer, C. Vallance, J.J. John, R. Turchetta, A. Nomerotski, L. Christensen, J.H. Nielsen, M.P. Johansson, H. Stapelfeldt, Phys. Rev. A **89**, 011401 (2014)
67. L.J. Frasinski, J. Phys. B: At. Mol. Opt. Phys. **49**, 152004 (2016)
68. C. Vallance, D. Heathcote, J.W.L. Lee, J. Phys. Chem. A **125**, 1117–1133 (2021)
69. L. Christensen, L. Christiansen, B. Shepperson, H. Stapelfeldt, Phys. Rev. A **94**, 023410 (2016)
70. R. Torres, R. de Nalda, J.P. Marangos, Phys. Rev. A **72**, 023420 (2005)
71. S. Trippel, T. Mullins, N.L.M. Müller, J.S. Kienitz, J.J. Omiste, H. Stapelfeldt, R. González-Férez, J. Küpper, Phys. Rev. A **89**, 051401 (2014)
72. S. Guérin, J. Mod. Opt. **55**, 3193–3201 (2008)
73. S. Guérin, A. Rouzée, E. Hertz, Phys. Rev. A **77**, 041404 (2008)
74. E.T. Karamatskos, S. Raabe, T. Mullins, A. Trabattoni, P. Stammer, G. Goldsztejn, R.R. Johansen, K. Długołecki, H. Stapelfeldt, M.J.J. Vrakking, S. Trippel, A. Rouzée, J. Küpper, Nat. Commun. **10**, 3364 (2019)
75. A.A. Søndergaard, *Understanding Laser-Induced Alignment and Rotation of Molecules Embedded in Helium Nanodroplets* (Aarhus University, Thesis, 2016)
76. E.F. Thomas, A.A. Søndergaard, B. Shepperson, N.E. Henriksen, H. Stapelfeldt, Phys. Rev. Lett. **120**, 163202 (2018)
77. P.M. Felker, J. Phys. Chem. **96**, 7844–7857 (1992)
78. C. Riehn, Chem. Phys. **283**, 297–329 (2002)
79. C.B. Madsen, L.B. Madsen, S.S. Viftrup, M.P. Johansson, T.B. Poulsen, L. Holmegaard, V. Kumarappan, K.A. Jørgensen, H. Stapelfeldt, J. Chem. Phys. **130**, 234310–9 (2009)
80. I. Nevo, L. Holmegaard, J.H. Nielsen, J.L. Hansen, H. Stapelfeldt, F. Filsinger, G. Meijer, J. Küpper, Phys. Chem. Chem. Phys. **11**, 9912–9918 (2009)
81. J.G. Underwood, B.J. Sussman, A. Stolow, Phys. Rev. Lett. **94**, 143002 (2005)
82. K.F. Lee, D.M. Villeneuve, P.B. Corkum, A. Stolow, J.G. Underwood, Phys. Rev. Lett. **97**, 173001 (2006)
83. X. Ren, V. Makhija, V. Kumarappan, Phys. Rev. Lett. **112**, 173602 (2014)
84. S.S. Viftrup, V. Kumarappan, S. Trippel, H. Stapelfeldt, E. Hamilton, T. Seideman, Phys. Rev. Lett. **99**, 143602–4 (2007)
85. J.L. Hansen, H. Stapelfeldt, D. Dimitrovski, M. Abu-samha, C.P.J. Martiny, L.B. Madsen, Phys. Rev. Lett. **106**, 073001 (2011)
86. B. Friedrich, D. Herschbach, J. Phys. Chem. A **103**, 10280–10288 (1999)
87. B. Friedrich, D. Herschbach, J. Chem. Phys. **111**, 6157–6160 (1999)
88. L. Holmegaard, J.H. Nielsen, I. Nevo, H. Stapelfeldt, F. Filsinger, J. Küpper, G. Meijer, Phys. Rev. Lett. **102**, 023001 (2009)

89. O. Ghafur, A. Rouzee, A. Gijsbertsen, W.K. Siu, S. Stolte, M.J.J. Vrakking, Nat Phys **5**, 289–293 (2009)
90. J.H. Nielsen, H. Stapelfeldt, J. Küpper, B. Friedrich, J.J. Omiste, R. González-Férez, Phys. Rev. Lett. **108**, 193001 (2012)
91. J.J. Omiste, R. González-Férez, Phys. Rev. A **94**, 063408 (2016)
92. S. Trippel, T. Mullins, N.L. Müller, J.S. Kienitz, R. González-Férez, J. Küpper, Phys. Rev. Lett. **114**, 103003 (2015)
93. F. Filsinger, J. Küpper, G. Meijer, L. Holmegaard, J.H. Nielsen, I. Nevo, J.L. Hansen, H. Stapelfeldt, J. Chem. Phys. **131**, 064309–13 (2009)
94. S.Haessler, J. Caillat, W. Boutu, C. Giovanetti-Teixeira, T. Ruchon, T. Auguste, Z. Diveki, P. Breger, A. Maquet, B. Carré, R. Taïeb, P. Saliéres, Nat. Phys. **6**, 200–206 (2010)
95. C. Vozzi, M. Negro, F. Calegari, G. Sansone, M. Nisoli, S. De Silvestri, S. Stagira, Nat. Phys. **7**, 822–826 (2011)
96. J.L. Hansen, L. Holmegaard, L. Kalhøj, S.L. Kragh, H. Stapelfeldt, F. Filsinger, G. Meijer, J. Küpper, D. Dimitrovski, M. Abu-samha, C.P.J. Martiny, L.B. Madsen, Phys. Rev. A **83**, 023406 (2011)
97. D. Dimitrovski, M. Abu-samha, L.B. Madsen, F. Filsinger, G. Meijer, J. Küpper, L. Holmegaard, L. Kalhøj, J.H. Nielsen, H. Stapelfeldt, Phys. Rev. A **83**, 023405 (2011)
98. I.V. Litvinyuk, K.F. Lee, P.W. Dooley, D.M. Rayner, D.M. Villeneuve, P.B. Corkum, Phys. Rev. Lett. **90**, 233003 (2003)
99. D. Pavicic, K.F. Lee, D.M. Rayner, P.B. Corkum, D.M. Villeneuve, Phys. Rev. Lett. **98**, 243001 (2007)
100. J.L. Hansen, L. Holmegaard, J.H. Nielsen, H. Stapelfeldt, D. Dimitrovski, L.B. Madsen, J. Phys. B: At. Mol. Opt. Phys. **45**, 015101 (2012)
101. J. Maurer, D. Dimitrovski, L. Christensen, L.B. Madsen, H. Stapelfeldt, Phys. Rev. Lett. **109**, 123001 (2012)
102. D. Dimitrovski, J. Maurer, H. Stapelfeldt, L. Madsen, Phys. Rev. Lett. **113**, 103005 (2014)
103. R. Johansen, K.G. Bay, L. Christensen, J. Thøgersen, D. Dimitrovski, L.B. Madsen, H. Stapelfeldt, J. Phys. B: At. Mol. Opt. Phys. **49**, 205601 (2016)
104. P. Sándor, A. Sissay, F. Mauger, M.W. Gordon, T.T. Gorman, T.D. Scarborough, M.B. Gaarde, K. Lopata, K.J. Schafer, R.R. Jones, J. Chem. Phys. **151**, 194308 (2019)
105. C.J. Hensley, J. Yang, M. Centurion, Phys. Rev. Lett. **109**, 133202 (2012)
106. R. Boll, D. Anielski, C. Bostedt, J.D. Bozek, L. Christensen, R. Coffee, S. De, P. Decleva, S.W. Epp, B. Erk, L. Foucar, F. Krasniqi, J. Küpper, A. Rouzée, B. Rudek, A. Rudenko, S. Schorb, H. Stapelfeldt, M. Stener, S. Stern, S. Techert, S. Trippel, M.J.J. Vrakking, J. Ullrich, D. Rolles, Phys. Rev. A **88**, 061402 (2013)
107. M.G. Pullen, B. Wolter, A.T. Le, M. Baudisch, M. Hemmer, A. Senftleben, C.D. Schröter, J. Ullrich, R. Moshammer, C.D. Lin, J. Biegert, Nat. Commun. **6** (2015)
108. J. Yang, M. Guehr, T. Vecchione, M.S. Robinson, R. Li, N. Hartmann, X. Shen, R. Coffee, J. Corbett, A. Fry, K. Gaffney, T. Gorkhover, C. Hast, K. Jobe, I. Makasyuk, A. Reid, J. Robinson, S. Vetter, F. Wang, S. Weathersby, C. Yoneda, M. Centurion, X. Wang, Nat. Commun. **7**, 1–9 (2016)
109. Wolter, B., Pullen, M.G., Le, A.T., Baudisch, M., Doblhoff-Dier, K., Senftleben, A., Hemmer, M., Schröter, C.D., Ullrich, J., Pfeifer, T., Moshammer, R., Gräfe, S., Vendrell, O., Lin, C.D., Biegert, J., Science **354**, 308–312 (2016)
110. J. Küpper, S. Stern, L. Holmegaard, F. Filsinger, A. Rouzée, A. Rudenko, P. Johnsson, A.V. Martin, M. Adolph, A. Aquila, S. Bajt, A. Barty, C. Bostedt, J. Bozek, C. Caleman, R. Coffee, N. Coppola, T. Delmas, S. Epp, B. Erk, L. Foucar, T. Gorkhover, L. Gumprecht, A. Hartmann, R. Hartmann, G. Hauser, P. Holl, A. Hömke, N. Kimmel, F. Krasniqi, K.U. Kühnel, J. Maurer, M. Messerschmidt, R. Moshammer, C. Reich, B. Rudek, R. Santra, I. Schlichting, C. Schmidt, S. Schorb, J. Schulz, H. Soltau, J.C.H. Spence, D. Starodub, L. Strüder, J. Thøgersen, M.J.J. Vrakking, G. Weidenspointner, T.A. White, C. Wunderer, G. Meijer, J. Ullrich, H. Stapelfeldt, D. Rolles, H.N. Chapman, Phys. Rev. Lett. **112**, 083002 (2014)

111. T. Kierspel, A. Morgan, J. Wiese, T. Mullins, A. Aquila, A. Barty, R. Bean, R. Boll, S. Boutet, P. Bucksbaum, H.N. Chapman, L. Christensen, A. Fry, M. Hunter, J.E. Koglin, M. Liang, V. Mariani, A. Natan, J. Robinson, D. Rolles, A. Rudenko, K. Schnorr, H. Stapelfeldt, S. Stern, J. Thøgersen, C.H. Yoon, F. Wang, J. Küpper, J. Chem. Phys. **152**, 084307 (2020)
112. P. Hockett, C.Z. Bisgaard, O.J. Clarkin, A. Stolow, Nat. Phys. **7**, 612–615 (2011)
113. C. Schröter, K. Kosma, T. Schultz, Science **333**, 1011–1015 (2011)
114. C. Schröter, J.C. Lee, T. Schultz, PNAS **115**, 5072–5076 (2018)
115. A.S. Chatterley, M.O. Baatrup, C.A. Schouder, H. Stapelfeldt, Phys. Chem. Chem. Phys. **22**, 3245–3253 (2020)
116. D.M. Villeneuve, S.A. Aseyev, P. Dietrich, M. Spanner, M.Y. Ivanov, P.B. Corkum, Phys. Rev. Lett. **85**, 542–545 (2000)
117. A. Korobenko, A.A. Milner, V. Milner, Phys. Rev. Lett. **112**, 113004 (2014)
118. A.A. Milner, A. Korobenko, V. Milner, Phys. Rev. A **93**, 053408 (2016)
119. A. Korobenko, V. Milner, Phys. Rev. Lett. **116**, 183001 (2016)
120. A.A. Milner, J.A. Fordyce, I. MacPhail-Bartley, W. Wasserman, V. Milner, I. Tutunnikov, I.S. Averbukh, Phys. Rev. Lett. **122**, 223201 (2019)
121. L. Christensen, J.H. Nielsen, C.S. Slater, A. Lauer, M. Brouard, H. Stapelfeldt, Phys. Rev. A **92**, 033411 (2015)
122. S. Ramakrishna, T. Seideman, Phys. Rev. Lett. **95**, 113001 (2005)
123. S. Ramakrishna, T. Seideman, J. Chem. Phys. **124**, 034101–034111 (2006)
124. T. Vieillard, F. Chaussard, D. Sugny, B. Lavorel, O. Faucher, J. Raman Spectrosc. **39**, 694–699 (2008)
125. N. Owschimikow, F. Königsmann, J. Maurer, P. Giese, A. Ott, B. Schmidt, N. Schwentner, J. Chem. Phys. **133**, 044311–044311–13 (2010)
126. J.M. Hartmann, C. Boulet, J. Chem. Phys. **136**, 184302–184302–17 (2012)
127. F. Chaussard, T. Vieillard, F. Billard, O. Faucher, J.M. Hartmann, C. Boulet, B. Lavorel, J. Raman Spectrosc. **46**, 691–694 (2015)
128. J. Ma, H. Zhang, B. Lavorel, F. Billard, E. Hertz, J. Wu, C. Boulet, J.M. Hartmann, O. Faucher, Nat. Commun. **10**, 1–7 (2019)
129. J. Ma, H. Zhang, B. Lavorel, F. Billard, J. Wu, C. Boulet, J.M. Hartmann, O. Faucher, Phys. Rev. A **101**, 043417 (2020)
130. J. Jang, R.M. Stratt, J. Chem. Phys. **113**, 5901–5916 (2000)
131. F. Stienkemeier, K.K. Lehmann, J. Phys. B: At. Mol. Opt. Phys. **39**, R127 (2006)
132. M. Hartmann, R.E. Miller, J.P. Toennies, A. Vilesov, Phys. Rev. Lett. **75**, 1566 (1995)
133. C. Callegari, A. Conjusteau, I. Reinhard, K.K. Lehmann, G. Scoles, J. Chem. Phys. **113**, 10535–10550 (2000)
134. G.E. Douberly, Molecules in helium nanodroplets, in *Topics in Applied Physics*, ed. by A. Slenczka, J.P. Toennies (2021)
135. V. Kumarappan, C.Z. Bisgaard, S.S. Viftrup, L. Holmegaard, H. Stapelfeldt, J. Chem. Phys. **125**, 194309–7 (2006)
136. A. Braun, M. Drabbels, Phys. Rev. Lett. **93**, 253401 (2004)
137. A. Braun, M. Drabbels, J. Chem. Phys. **127**, 114304 (2007)
138. M. Mudrich, F. Stienkemeier, Int. Rev. Phys. Chem. **33**, 301–339 (2014)
139. F. Bierau, P. Kupser, G. Meijer, G. von Helden, Phys. Rev. Lett. **105**, 133402 (2010)
140. A.I.G. Florez, D.S. Ahn, S. Gewinner, W. Schoellkopf, G. von Helden, Phys. Chem. Chem. Phys. **17**, 21902–21911 (2015)
141. A. Mauracher, O. Echt, A.M. Ellis, S. Yang, D.K. Bohme, J. Postler, A. Kaiser, S. Denifl, P. Scheier, Phys. Rep. **751**, 1–90 (2018)
142. G. von Helden, Molecules in helium nanodroplets, in *Topics in Applied Physics*, ed. by A. Slenczka, J.P. Toennies (2021)
143. A. Slenczka, Molecules in helium nanodroplets, in *Topics in Applied Physics*, ed. by A. Slenczka, J.P. Toennies (2021)
144. D. Pentlehner, R. Riechers, B. Dick, A. Slenczka, U. Even, N. Lavie, R. Brown, K. Luria, Rev. Sci. Instrum. **80**, 043302 (2009)

145. J.J. Larsen, H. Sakai, C.P. Safvan, I. Wendt-Larsen, H. Stapelfeldt, J. Chem. Phys. **111**, 7774–7781 (1999)
146. E. Hamilton, T. Seideman, T. Ejdrup, M.D. Poulsen, C.Z. Bisgaard, S.S. Viftrup, H. Stapelfeldt, Phys. Rev. A **72**, 043402–12 (2005)
147. J.H. Posthumus, Rep. Prog. Phys. **67**, 623 (2004)
148. D. Pentlehner, J.H. Nielsen, L. Christiansen, A. Slenczka, H. Stapelfeldt, Phys. Rev. A **87**, 063401 (2013)
149. A. Scheidemann, B. Schilling, J.P. Toennies, J. Phys. Chem. **97**, 2128–2138 (1993)
150. M. Lewerenz, B. Schilling, J.P. Toennies, Chem. Phys. Lett. **206**, 381–387 (1993)
151. D. Pentlehner, J.H. Nielsen, A. Slenczka, K. Mølmer, H. Stapelfeldt, Phys. Rev. Lett. **110**, 093002 (2013)
152. S. Grebenev, M. Hartmann, M. Havenith, B. Sartakov, J.P. Toennies, A.F. Vilesov, J. Chem. Phys. **112**, 4485 (2000)
153. A.S. Chatterley, L. Christiansen, C.A. Schouder, A.V. Jørgensen, B. Shepperson, I.N. Cherepanov, G. Bighin, R.E. Zillich, M. Lemeshko, H. Stapelfeldt, Phys. Rev. Lett. **125**, 013001 (2020)
154. K.K. Lehmann, Mol. Phys. **97**, 645–666 (1999)
155. R. Lehnig, P.L. Raston, W. Jäger, Faraday Discuss. **142**, 297–309 (2009)
156. K.K. Lehmann, J. Chem. Phys. **114**, 4643–4648 (2001)
157. D. Rosenberg, R. Damari, S. Kallush, S. Fleischer, J. Phys. Chem. Lett. **8**, 5128–5135 (2017)
158. A.A. Milner, A. Korobenko, J.W. Hepburn, V. Milner, The J. Chem. Phys. **147**, 124202 (2017)
159. K. Nauta, R.E. Miller, J. Chem. Phys. **115**, 10254–10260 (2001)
160. R. Zillich, Y. Kwon, K. Whaley, Phys. Rev. Lett. **93**, 250401 (2004)
161. B. Shepperson, A.A. Søndergaard, L. Christiansen, J. Kaczmarczyk, R.E. Zillich, M. Lemeshko, H. Stapelfeldt, Phys. Rev. Lett. **118**, 203203 (2017)
162. L. García-Gutierrez, L. Delgado-Tellez, l. Valdés, R. Prosmiti, P. Villarreal, G. Delgado-Barrio, J. Phys. Chem. A **113**, 5754–5762 (2009)
163. S.E. Ray, A.B. McCoy, J.J. Glennon, J.P. Darr, E.J. Fesser, J.R. Lancaster, R.A. Loomis, The J. Chem. Phys. **125**, 164314 (2006)
164. F. Paesani, K.B. Whaley, J. Chem. Phys. **121**, 4180–4192 (2004)
165. A.A. Søndergaard, R.E. Zillich, H. Stapelfeldt, J. Chem. Phys. **147**, 074304 (2017)
166. P. Vindel-Zandbergen, J. Jiang, M. Lewerenz, C. Meier, M. Barranco, M. Pi, N. Halberstadt, J. Chem. Phys. **149**, 124301 (2018)
167. R. Schmidt, M. Lemeshko, Phys. Rev. Lett. **114**, 203001 (2015)
168. M. Lemeshko, Phys. Rev. Lett. **118**, 095301 (2017)
169. J.D. Pickering, B. Shepperson, L. Christiansen, H. Stapelfeldt, Phys. Rev. A **99**, 043403 (2019)
170. C.A. Schouder, A.S. Chatterley, L.B. Madsen, F. Jensen, H. Stapelfeldt, Phys. Rev. A **102**, 063125 (2020)
171. J.D. Pickering, B. Shepperson, B.A. Hübschmann, F. Thorning, H. Stapelfeldt, Phys. Rev. Lett. **120**, 113202 (2018)
172. A.S. Chatterley, B. Shepperson, H. Stapelfeldt, Phys. Rev. Lett. **119**, 073202 (2017)
173. R. Boll, A. Rouzée, M. Adolph, D. Anielski, A. Aquila, S. Bari, C. Bomme, C. Bostedt, J.D. Bozek, H.N. Chapman, L. Christensen, R. Coffee, N. Coppola, S. De, P. Decleva, S.W. Epp, B. Erk, F. Filsinger, L. Foucar, T. Gorkhover, L. Gumprecht, A. Hömke, L. Holmegaard, P. Johnsson, J.S. Kienitz, T. Kierspel, F. Krasniqi, K.U. Kühnel, J. Maurer, M. Messerschmidt, R. Moshammer, N.L.M. Müller, B. Rudek, E. Savelyev, I. Schlichting, C. Schmidt, F. Scholz, S. Schorb, J. Schulz, J. Seltmann, M. Stener, S. Stern, S. Techert, J. Thøgersen, S. Trippel, J. Viefhaus, M. Vrakking, H. Stapelfeldt, J. Küpper, J. Ullrich, A. Rudenko, D. Rolles, Faraday Discuss. (2014)
174. A.S. Chatterley, C. Schouder, L. Christiansen, B. Shepperson, M.H. Rasmussen, H. Stapelfeldt, Nat. Commun. **10**, 133 (2019)
175. A.S. Chatterley, E.T. Karamatskos, C. Schouder, L. Christiansen, A.V. Jørgensen, T. Mullins, J. Küpper, H. Stapelfeldt, J. Chem. Phys. **148**, 221105 (2018)
176. Z.C. Yan, T. Seideman, The J. Chem. Phys. **111**, 4113–4120 (1999)

177. A. Goban, S. Minemoto, H. Sakai, Phys. Rev. Lett. **101**, 013001 (2008)
178. C.S. Slater, S. Blake, M. Brouard, A. Lauer, C. Vallance, C.S. Bohun, L. Christensen, J.H. Nielsen, M.P. Johansson, H. Stapelfeldt, Phys. Rev. A **91**, 053424 (2015)
179. H. Tanji, S. Minemoto, H. Sakai, Phys. Rev. A **72**, 063401 (2005)
180. V. Makhija, X. Ren, V. Kumarappan, Phys. Rev. A **85**, 033425 (2012)
181. Z. Vager, R. Naaman, E.P. Kanter, Science **244**, 426–431 (1989)
182. I. Luzon, K. Jagtap, E. Livshits, O. Lioubashevski, R. Baer, D. Strasser, Phys. Chem. Chem. Phys. **19**, 13488–13495 (2017)
183. T. Takanashi, K. Nakamura, E. Kukk, K. Motomura, H. Fukuzawa, K. Nagaya, S.I. Wada, Y. Kumagai, D. Iablonskyi, Y. Ito, Y. Sakakibara, D. You, T. Nishiyama, K. Asa, Y. Sato, T. Umemoto, K. Kariyazono, K. Ochiai, M. Kanno, K. Yamazaki, K. Kooser, C. Nicolas, C. Miron, T. Asavei, L. Neagu, M. Schöffler, G. Kastirke, X.J. Liu, A. Rudenko, S. Owada, T. Katayama, T. Togashi, K. Tono, M. Yabashi, H. Kono, K. Ueda, Phys. Chem. Chem. Phys. **19**, 19707–19721 (2017)
184. A. Rudenko, L. Inhester, K. Hanasaki, X. Li, S.J. Robatjazi, B. Erk, R. Boll, K. Toyota, Y. Hao, O. Vendrell, C. Bomme, E. Savelyev, B. Rudek, L. Foucar, S.H. Southworth, C.S. Lehmann, B. Kraessig, T. Marchenko, M. Simon, K. Ueda, K.R. Ferguson, M. Bucher, T. Gorkhover, S. Carron, R. Alonso-Mori, J.E. Koglin, J. Correa, G.J. Williams, S. Boutet, L. Young, C. Bostedt, S.K. Son, R. Santra, D. Rolles, Nature **546**, 129–132 (2017)
185. M. Pitzer, M. Kunitski, A.S. Johnson, T. Jahnke, H. Sann, F. Sturm, L.P.H. Schmidt, H. Schmidt-Böcking, R. Dörner, J. Stohner, J. Kiedrowski, M. Reggelin, S. Marquardt, A. Schießer, R. Berger, M.S. Schöffler, Science **341**, 1096–1100 (2013)
186. P. Herwig, K. Zawatzky, M. Grieser, O. Heber, B. Jordon-Thaden, C. Krantz, O. Novotný, R. Repnow, V. Schurig, D. Schwalm, Z. Vager, A. Wolf, O. Trapp, H. Kreckel, Science **342**, 1084–1086 (2013)
187. E.F. Thomas, N.E. Henriksen, J. Chem. Phys. **150**, 024301 (2019)
188. H. Stapelfeldt, E. Constant, P.B. Corkum, Phys. Rev. Lett. **74**, 3780–3783 (1995)
189. M. Burt, R. Boll, J.W.L. Lee, K. Amini, H. Köckert, C. Vallance, A.S. Gentleman, S.R. Mackenzie, S. Bari, C. Bomme, S. Düsterer, B. Erk, B. Manschwetus, E. Müller, D. Rompotis, E. Savelyev, N. Schirmel, S. Techert, R. Treusch, J. Küpper, S. Trippel, J. Wiese, H. Stapelfeldt, B.C. de Miranda, R. Guillemin, I. Ismail, L. Journel, T. Marchenko, J. Palaudoux, F. Penent, M.N. Piancastelli, M. Simon, O. Travnikova, F. Brausse, G. Goldsztejn, A. Rouzée, M. Géléoc, R. Geneaux, T. Ruchon, J. Underwood, D.M.P. Holland, A.S. Mereshchenko, P.K. Olshin, P. Johnsson, S. Maclot, J. Lahl, A. Rudenko, F. Ziaee, M. Brouard, D. Rolles, Phys. Rev. A **96**, 043415 (2017)
190. T. Endo, S.P. Neville, V. Wanie, S. Beaulieu, C. Qu, J. Deschamps, P. Lassonde, B.E. Schmidt, H. Fujise, M. Fushitani, A. Hishikawa, P.L. Houston, J.M. Bowman, M.S. Schuurman, F. Légaré, H. Ibrahim, Science **370**, 1072–1077 (2020)
191. H. Ibrahim, B. Wales, S. Beaulieu, B.E. Schmidt, N. Thiré, E.P. Fowe, R. Bisson, C.T. Hebeisen, V. Wanie, M. Giguére, J.C. Kieffer, M. Spanner, A.D. Bandrauk, J. Sanderson, M.S. Schuurman, F. Légaré, Nat. Commun. **5**, 4422 (2014)
192. U. Ablikim, C. Bomme, H. Xiong, E. Savelyev, R. Obaid, B. Kaderiya, S. Augustin, K. Schnorr, I. Dumitriu, T. Osipov, R. Bilodeau, D. Kilcoyne, V. Kumarappan, A. Rudenko, N. Berrah, D. Rolles, Sci. Rep. **6**, srep38202 (2016)
193. M. Burt, K. Amini, J.W.L. Lee, L. Christiansen, R.R. Johansen, Y. Kobayashi, J.D. Pickering, C. Vallance, M. Brouard, H. Stapelfeldt, The J. Chem. Physi. **148**, 091102 (2018)
194. E. Skovsen, M. Machholm, T. Ejdrup, J. Thøgersen, H. Stapelfeldt, Phys. Rev. Lett. **89**, 133004 (2002)
195. C. Petersen, E. Péronne, J. Thøgersen, H. Stapelfeldt, M. Machholm, Phys. Rev. A **70**, 033404 (2004)
196. T. Ergler, A. Rudenko, B. Feuerstein, K. Zrost, C.D. Schröter, R. Moshammer, J. Ullrich, Phys. Rev. Lett. **97**, 193001 (2006)
197. S. Zeller, M. Kunitski, J. Voigtsberger, A. Kalinin, A. Schottelius, C. Schober, M. Waitz, H. Sann, A. Hartung, T. Bauer, M. Pitzer, F. Trinter, C. Goihl, C. Janke, M. Richter, G. Kastirke,

M. Weller, A. Czasch, M. Kitzler, M. Braune, R.E. Grisenti, W. Schöllkopf, L.P.H. Schmidt, M.S. Schöffler, J.B. Williams, T. Jahnke, R. Dörner, PNAS **113**, 14651–14655 (2016)
198. M. Kunitski, Molecules in helium nanodroplets, in *Topics in Applied Physics*, ed. by A. Slenczka, J.P. Toennies (2021)
199. J.D. Pickering, B. Shepperson, L. Christiansen, H. Stapelfeldt, J. Chem. Phys. **149**, 154306 (2018)
200. N. Moazzen-Ahmadi, A.R.W. McKellar, Int. Rev. Phys. Chem. **32**, 611–650 (2013)
201. C. Schouder, A.S. Chatterley, F. Calvo, L. Christiansen, H. Stapelfeldt, Struct. Dyn. **6**, 044301 (2019)
202. Schouder, C., Chatterley, A.S., Johny, M., Hübschmann, F., Al-Refaie, A.F., Calvo, F., Küpper, J., Stapelfeldt, H., To be submitted (2021)
203. L.F. Gomez, K.R. Ferguson, J.P. Cryan, C. Bacellar, R.M.P. Tanyag, C. Jones, S. Schorb, D. Anielski, A. Belkacem, C. Bernando, R. Boll, J. Bozek, S. Carron, G. Chen, T. Delmas, L. Englert, S.W. Epp, B. Erk, L. Foucar, R. Hartmann, A. Hexemer, M. Huth, J. Kwok, S.R. Leone, J.H.S. Ma, F.R.N.C. Maia, E. Malmerberg, S. Marchesini, D.M. Neumark, B. Poon, J. Prell, D. Rolles, B. Rudek, A. Rudenko, M. Seifrid, K.R. Siefermann, F.P. Sturm, M. Swiggers, J. Ullrich, F. Weise, P. Zwart, C. Bostedt, O. Gessner, A.F. Vilesov, Science **345**, 906–909 (2014)
204. R.M.P. Tanyag, B. Langbehn, D. Rupp, T. Möller, Molecules in helium nanodroplets, in *Topics in Applied Physics*, ed. by A. Slenczka, J.P. Toennies (2021)
205. Y. He, J. Zhang, W. Kong, J. Chem. Phys. **145**, 034307 (2016)
206. L. Lei, Y. Yao, J. Zhang, D. Tronrud, W. Kong, C. Zhang, L. Xue, L. Dontot, M. Rapacioli, J. Phys. Chem. Lett. **11**, 724–729 (2020)
207. J. Zhang, S.D. Bradford, W. Kong, C. Zhang, L. Xue, J. Chem. Phys. **152**, 224306 (2020)
208. J. Zhang, Y. He, L. Lei, Y. Yao, S. Bradford, W. Kong, Molecules in helium nanodroplets, in *Topics in Applied Physics*, ed. by A. Slenczka, J.P. Toennies (2021)
209. H. Saigusa, E.C. Lim, Chem. Phys. Lett. **336**, 65–70 (2001)
210. M. Miyazaki, M. Fujii, Phys. Chem. Chem. Phys. **17**, 25989–25997 (2015)
211. D. Zhong, P.Y. Cheng, A.H. Zewail, The J. Chem. Phys. **105**, 7864–7867 (1996)
212. M.D. Wheeler, D.T. Anderson, M.I. Lester, Int. Rev. Phys. Chem. **19**, 501–529 (2000)
213. F. Stienkemeier, J. Higgins, W.E. Ernst, G. Scoles, Phys. Rev. Lett. **74**, 3592–3595 (1995)
214. F. Ancilotto, G. DeToffol, F. Toigo, Phys. Rev. B **52**, 16125–16129 (1995)
215. L. Bruder, M. Koch, M. Mudrich, F. Stienkemeier, Molecules in helium nanodroplets, in *Topics in Applied Physics*, ed. by A. Slenczka, J.P. Toennies (2021)